Dynamique électronique dans les molécules organiques par la spectroscopie Core-Hole Clock

Jessica Barbosa Martins

Sorbonne Université
École Doctorale 388
Discipline : Chimie Physique

Thèse de doctorat

Soutenue le 31 mai 2021 par

Jessica Barbosa Martins

Dynamique Électronique dans les Molécules Organiques par la Spectroscopie Core-Hole Clock

Mme. Tatiana Marchenko	(Directeur de thèse)
M. Arnaldo Naves de Brito	(Rapporteur)
M. Lorenzo Avaldi	(Rapporteur)
M. Emmanuel Maisonhaute	(Examinateur)
Mme. Valérie Brenner	(Examinateur)
M. Evangelos Papalazarou	(Examinateur)

I dedicate this thesis to all people involved in the battle against one of the most challenging crises of our times. Science matters.

"A nation that does not know
its history and past
will not have a chance
to build a better future."

Luiz Inácio Lula da Silva

Abstract

The use of synchrotron radiation in the so-called tender X-ray domain, which ranges from around 2 keV to 12 keV, enables the core-shell excitation/ionization of chemical systems. Since these core-excited/ionized states are quite unstable, the system decays. Thus, such states own ultrashort lifetime on the time scales of femtoseconds. The relaxation pathways for the decay to a more stable state can occur via the ejection of an electron or emission of a photon. In this thesis, we studied processes resulting from the interaction between the X-ray radiation and matter through the employment of electron spectroscopy techniques. We experimentally observed the theoretical prediction of the relativistic nature of the photoionization of the spin-orbit doublets in Argon and Xenon. Following, we continued our studies on chemical systems in gas-phase. However, we moved to larger chemical systems: sulfur-based aromatic molecules. We explored the sensitivity of resonant Auger spectroscopy to observe conjugation effects following the relaxation of the core-excited states. Theoretical calculations provided an interpretation of the behavior observed in the resonant Auger spectra. In the last part of this work, we applied the core-hole clock spectroscopy (CHCS) to investigation of electron dynamics in two thiophene-based polymer thin films: polythiophene (PT) and poly[3-hexylthiophene-2,5-diyl] (P3HT) deposited on ITO substrate. Using resonant Auger electron spectroscopy, we provided an indication of from which molecular orbital the spectator electron delocalizes.

Résumé

L'utilisation du rayonnement synchrotron dans le domaine dit de rayons X tendres, qui va d'environ 2 keV à 12 keV, permet l'excitation/ionisation des systèmes chimiques en couche profonde. Étant donné que ces états sont assez instables, vont alors se relaxer par émission dun photon ou dun électron. Ainsi, de tels états possèdent une durée de vie ultracourte dans les échelles de temps de la femtoseconde. Les voies de relaxation pour la relaxation vers un système plus stable peuvent se produire via l'éjection d'un électron ou l'émission d'un photon. Dans cette thèse, nous avons étudié les processus résultant de l'interaction entre le rayonnement X et la matière grâce à l'utilisation de techniques de spectroscopie électronique. Nous avons observé expérimentalement la prédiction théorique de la nature relativiste de la photoionisation des doublets spin-orbite pour l'argon et le xénon. Ensuite, nous avons conservé nos études sur les systèmes chimiques en phase gazeuse. Cependant, nous avons opté pour des systèmes chimiques plus larges: des molécules aromatiques à base de soufre. Nous avons exploré la sensibilité de la spectroscopie Auger résonnante par mesurer les spectres Auger résonnants du soufre $KL_{2,3}L_{2,3}$ sous forme de cartes bidimensionnelles pour étudier les effets de conjugaison suite à la relaxation des états excités par le couche profonde. Les calculs théoriques ont fourni une compréhension complémentaire du comportement observé dans les spectres Auger résonants. Dans la dernière partie de ce travail, nous avons exploré la méthode de core-hole clock spectroscopy (CHCS) pour étudier la dynamique électronique dans deux films minces de polymère à base de thiophène: le polythiophène (PT) et le poly [3-hexylthiophène-2,5-diyl] (P3HT) déposé sur un substrat ITO. En utilisant la spectroscopie électronique Auger résonante, nous avons fourni une indication de l'orbitale moléculaire à partir de laquelle l'électron spectateur se délocalise.

Contents

Chapter

1 Introduction

In this thesis, we investigated different processes in atoms, molecules and polymers through the response of these chemical systems to the interaction with the X-ray radiation in tender regime ($2 - 12$ keV). When a core electron is excited/ionized, the system becomes quite unstable and then, excess energy is released in the form of either photon (via radiative decay) or of ejected electron (via the nonradiative Auger decay path). These two channels compete and the probability of these decay pathways to occur depends on the atomic number of the studied chemical element. In this work, we employed high-resolution electron spectroscopy with an outstanding instrumental resolution, which measures the emitted electron's kinetic energy resulting from the ionization induced by a high-energy photon.

We start the first chapter by the concepts of the X-ray absorption (XAS) and photoelectron spectroscopy (PES). The resonant Auger spectroscopy (RAS) is discussed in the framework of the X-ray Raman scattering (XRS) theory. The concepts of Raman effect, effective duration time and the possibility to study nuclear dynamics are introduced. We also present the Core-hole clock spectroscopy (CHCS) as a suitable tool for investigating nuclear and electron dynamics. Finally, we present several studies on ultrafast electron dynamics in different media using the core-hole clock techniques.

The second chapter starts by presenting a brief history of the development of the synchrotron radiation facilities. Next, the characteristics of SOLEIL synchrotron facility are presented as well as an overview of GALAXIES, the beamline in which the measurements of this work were performed. We also presented a brief review of the potential of HAXPES by pinpointing the main topics of investigation using this tool and showing the rapid increase of HAXPES facilities worldwide. The following section focuses on the details of the HAXPES setup installed at the GALAXIES beamline. We finish this chapter by detailing the data treatment concerning the electron kinetic energy and the photon energy calibration required in our experiments, as well

as a method to obtain the spectrometer resolution and the photon bandwidth values.

In the third chapter, we presented our findings on core-level photoionization for Argon and Xenon showcases to investigate considerably small intensity processes. The overcome of recent instrumental limitations enables measuring the ratio of the photoionization cross sections of the spin-orbit components at energies far above their thresholds. We could experimentally confirm the theoretical predictions for the non-statistic (relativistic) behavior of the photoionization of the spin-orbit doublets.

In the fourth chapter, our studies concerning molecular systems in gas-phase are presented. We performed resonant Auger spectroscopy in sulfur-based aromatic molecules. We employed the sensitivity of this technique as a powerful tool to probe stabilization effects on the electronic structure of these chemical systems. In the two aromatics, thiophene and thiazole, a change in the energy order of the two lowest core-excited states of Sulfur is observed, in contrast to the saturated analog of thiophene, thiolane. Theoretical methods were applied to describe the electronic structure changes, providing the interpretation of the experimentally observed behavior.

In the fifth chapter, we explored the potential of CHCS as a tool to understand electron delocalization in two thiophene-based thin-film polymers: polythiophene (PT) and poly[3-hexylthiophene-2,5-diyl] (P3HT) deposited on ITO substrate. The CHCS method uses the core-hole lifetime as an internal clock for investigations of dynamical processes. Since the lifetime of core-excited states is on the (sub)femtosecond timescale, the CHCS was quite convenient for observing ultrafast electronic motion. We performed RAS, one of the CHCS techniques, to monitor the electron delocalization in a core-excited state. Moreover, the electron delocalization times were obtained by quantifying the integrated intensity ratio between spectator Auger and normal Auger contributions from the resonant Auger spectra. We measured the spectra at two different angles of the photon beam incidence with respect to the sample surface. A strong angle dependence was observed for the P3HT samples, indicating an organized film-structure. The electron delocalization in both films was demonstrated to be related to the resonant excitation of the σ^* orbital.

A group of complementary spectroscopic techniques can be applied to investigate the electronic structure and dynamics of chemical systems. The study of filled electronic levels can be done by performing photoelectron spectroscopy technique. Absorption spectroscopies can be performed to obtain information at empty states and the processes following photoelectron emission. During the relaxation from a core-excited state, an electron from a higher occupied molecular orbital can occupy the inner-shell vacancy. In the decay process, either photon (radiative decay) or electrons (non-radiative decay) can be released. The techniques related to these processes are, respectively, X-ray emission and Auger spectroscopy. Then, the combination of absorption spectroscopies, where the transition between the initial ground state and the intermediate excited state is observed, and the emission spectroscopies, where the decay products are detected, gives a complete picture of the electronic structure and dynamics of the chemical systems. [1] In the following, we present a review of the essential concepts of the X-ray absorption process, photoelectron spectroscopy, and resonant Auger spectroscopy.

1.1 The X-ray Absorption Process

The probability of a chemical system to be photoionized/photoexcited by an incident X-ray photon of energy $\hbar\Omega$ is given by the X-ray absorption cross section of this target chemical system. The transition probability, P_{if} (Equation 1.1), per unit of time, between two states i and f (whether it is an ionization or an excitation) is obtained by Fermi's golden rule (Equation 1.1) formulated from the time-dependent perturbation theory.

$$P_{if} = \frac{2\pi}{\hbar} \left| \left\langle \Psi_f \left| \hat{H}_{int} \right| \Psi_i \right\rangle \right|^2 \delta(E_f - E_i - \hbar\Omega) \tag{1.1}$$

where $|\Psi_i\rangle$ and $|\Psi_f\rangle$ correspond to the initial state and the final state wave functions, respectively, and both are composed of an electronic part and a nuclear part. The Dirac function δ stands for the energy conservation so that the transition occurs if the final state energy, E_f, equals the energy of the initial state, E_i, plus the photon energy, $\hbar\Omega$. The squared matrix elements give the transition rate, and $\hat{H}_{int}$ is the Hamiltonian that describes the electromagnetic field. $\hat{H}_{int}$ can be written by using the Coulomb gauge condition to describe the interaction between the chemical system and the electric field of the incident radiation as presented in Equation 1.2.

$$\hat{H}_{int} = -\frac{q}{m_e}\vec{p}\cdot\vec{A} \propto \vec{\epsilon}\cdot\frac{\vec{p}}{m_e} exp(-i\vec{k}\cdot\vec{r}) \tag{1.2}$$

where $\vec{p}$ is the electron momentum, $\vec{A}$ is the vector potential of the incident photon, $\vec{\epsilon}$ is the unit vector of incident photon polarization, which is perpendicular to the propagation direction of the radiation beam, $\vec{k}$ is the wave vector specifying the propagation direction of the incident photon and $\vec{r}$ correspond to the electrons' radial coordinate. The equation's exponential term can be rewritten using a Taylor expansion as presented in Equation 1.3.

$$exp(-i\vec{k}\cdot\vec{r}) \approx 1 - i\vec{k}\cdot\vec{r} - \frac{1}{2}(i\vec{k}\cdot\vec{r})^2 + \cdots \tag{1.3}$$

One can simplify the Equation 1.2 by truncating the Taylor expansion (Equation 1.3) in the first term, by assuming that $|\vec{r}| << \lambda/2\pi$, where λ is the X-ray wavelength. This approximation, called the *dipole approximation*, describes the interaction of the radiation and a chemical system when λ is considerably larger than the system's dimensions.

The cross section of the transition between a state i and a state f can then be written as in the Equation 1.4.

$$\sigma_{if}(\Omega) = \frac{4\pi^2\Omega\alpha_0^2}{3}\left|\left\langle \Psi_f \left| \sum_k r_k \right| \Psi_i \right\rangle\right|^2 \delta(E_f - E_i - \hbar\Omega) \tag{1.4}$$

where the term α_0 is the fine structure constant and $\langle\Psi_f|\sum_k r_k|\Psi_i\rangle$ is the dipole matrix elements, which includes all the electrons in the system. The dipole approximation gives rise to the selection rules that constrain the allowed transitions between two quantum states in a system.

1.2 Photoelectron Spectroscopy

The basis of the electron spectroscopy is the photoelectron effect, i.e., the emission of electrons by absorption of light, first observed by Heinrich Hertz in 1887 [2]. In 1905, Albert Einstein provided a mathematical description for this effect that led to his Nobel prize in physics in 1921 [3]. This is one of the cornerstones of our comprehension of the nature of electromagnetic radiation and also of the modern spectroscopy. He described the ionization process as the absorption of light quanta, which are nowadays called photons. Einstein postulated that the photons have energy equal to the Planck constant multiplied by its frequency. Moreover, every photon with energy higher than certain energy has the possibility to eject one electron. The Equation 1.5 shows Einstein's formulation for the photoelectric effect.

$$\varepsilon_{kin} = \hbar\omega - E_B \tag{1.5}$$

where ε_{kin} is the kinetic energy of the ejected electron, $\hbar$ is the reduced form of Planck's constant, ω stands for the frequency of the light, and E_B is the binding energy of the electron, i.e., the energy required to eject the electron from the studied system. By the 1920s, several unsuccessful attempts to measure the kinetic energy of the photoelectrons by using X-rays were made. In the 1950s, Kai Siegbahn implemented the electron spectroscopy for chemical analysis (ESCA) [4] thanks to the instrumentation progress made in nuclear sciences. This technique applies X-rays (commonly an Aluminium anode source) and single-photon absorption, leading to the emission of one electron from a deep shell. The first key point of ESCA was the possibility to derive the chemical composition of samples (solid or gaseous) by identifying the atomic species present in the sample. This was possible due to the atom-specificity of the core electrons' binding energy. The second key point was the observation of the "chemical shift," i.e., the slight displacement of the binding energy of a core electron of an element due to a change in its chemical bonding (chemical environment).

Few decades after the implementation of ESCA, the development of the synchrotron radiation facilities in the 1970s opened new possibilities due to the great advantages of tunability, intensity, and stability compared to the conventional sources, enhancing the research on core photoelectron spectroscopy of atoms, molecules, and solids in VUV and X-ray regions. Specifically for gas-phase systems, photoelectron spectroscopy experiments focused in the VUV and soft X-ray domains rather than the harder X-ray regime. The mentioned developments on synchrotron radiation enable measuring processes of a considerably small cross-section over the UV and X-ray energy ranges. In particular, in the past five years, improvements in synchrotron radiation and electron detectors in the tender X-ray regime allowed us to conduct measurements using photoelectron spectroscopy that could not be performed a few years ago. For example, now it is possible to study the ratios of spin-orbit doublet photoionization cross-sections (i.e., their branching ratios) experimentally, at energies far above their thresholds, as presented in Chapter 3.

1.2.1 Partial Cross Section and Angular Distribution

The partial cross section for creating a specific ionized state of a chemical system can be determined using photoelectron spectroscopy. The description of this cross section given by Equation 1.4 allows separation of ionization processes, which give rise to energetically non-degenerate pho-

toelectron lines as independent partial cross sections with individual cross-sectional behavior. This behavior reflects the orbital structure of the particular subshell and the several interactions between different subshells.

Multi-electron chemical systems have a spatial distribution of electrons. Therefore, the experimentally measurable intensities of electrons in photoelectron spectroscopy experiments may show an angular dependence. We can describe this angular dependence also in terms of the electric dipole approximation. When this approximation is applied to the electron emission upon the interaction with a photon, an expression for the measurable intensity, $I(\theta)$, can be written from the differential of the partial cross section (Equation 1.4) as presented in Equation 1.6. This differential equation describes the angular distribution of the emitted electrons from a gas-phase sample in a random orientation, excited by 100% linearly polarized light.

$$I(\theta) = \frac{d\sigma}{d\Omega} = \frac{\sigma}{4\pi}\left(1 + \frac{\beta}{2}\left(3\cos^2\theta - 1\right)\right) \tag{1.6}$$

where θ is the angle between the electric field vector and the vector that describes the direction of the ejected electron, σ is the angle integrated cross-section of a given state, and β is the asymmetry parameter. The $\beta-$parameter is independent of θ, but can depend on the excitation energy or the electrons' kinetic energy. This parameter assumes values ranging from -1 to 2. The photoelectron differential cross-section is illustrated in Figure 1.1. For example, consider the photoionization of an atomic 1s orbital. The electron in this orbital has angular momentum, $l = 0$. Upon the photon impact, the angular momentum of this electron becomes $l = 1$, according to the dipole selection rules ($\Delta l = \pm 1$). Therefore, the ejected electron leaves the system as a p-wave, corresponding to the case of $\beta = 2$. In this case, the intensity in the polarization vector plane is maximum and close to zero in the plane perpendicular to the polarization vector. We can extend the same arguments for orbitals with different characters and relate them to the corresponding $\beta-$value.

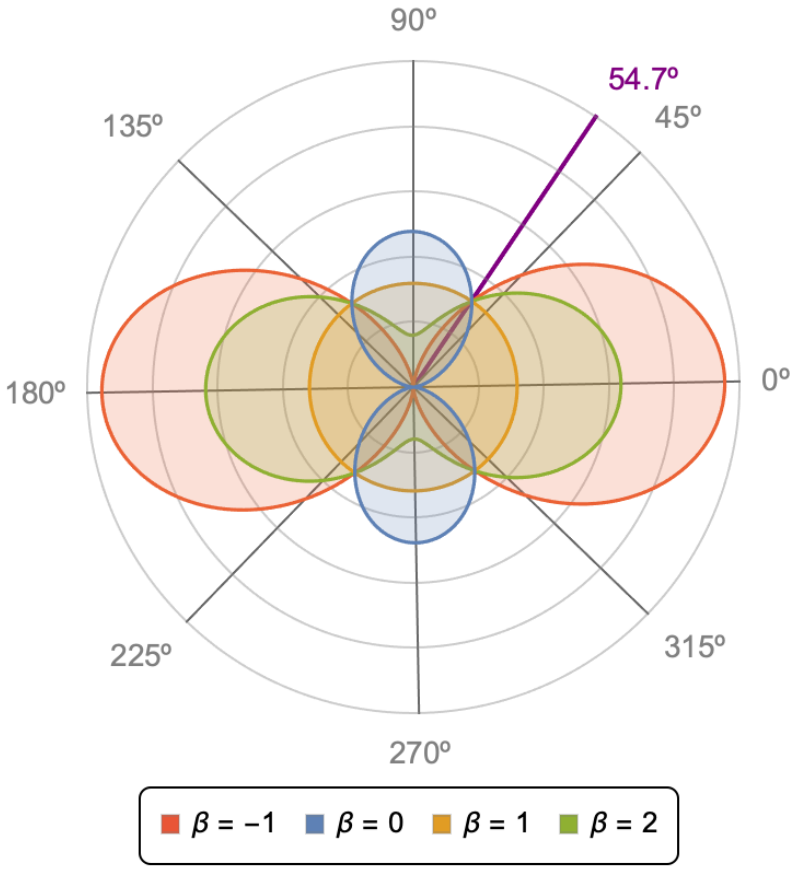

Figure 1.1: *Polar plot for the electron angular distribution at different angles with respect to the polarization plane of the radiation.*

An important observation in Figure 1.1 is the connection of all angular distributions in four symmetrical points. In these points, the angular distributions are independent of the $\beta-$parameter. One of these points is referred to as *magic angle* and is at a value of 54.7° with respect to the polarization vector of the electromagnetic radiation. The name "magic angle" is due to the intensity distribution being independent of the wave-character of the emitted electron. If an electron energy analyzer is mounted at the magic angle (assuming 100% linear polarization), the angular distribution vanishes and, therefore, the differential partial cross section in the Equation 1.6 becomes proportional to the integral partial cross section. Otherwise, if the analyzer is mounted at a different angle, then the correction factors are necessary due to angular distribution effects [5, 6]. In chapter 3, we present our results on the photoionization branching ratios of spin-orbit doublets of Ar and Xe. However, our measurements were not performed at the magic angle, where the photoelectron intensity is proportional to the partial cross section, but the lenses of our analyzer are at 0°, so that angular distribution effects come into play as the angular distributions of the two components of a spin-orbit doublet differ.

1.2.2 Line Shapes

A core-ionized state has a finite life-time, τ, which is of the order of 10^{-15} s or 1 fs. The observed energy of the electron is recorded according to the Heisenberg's uncertainty principle (Equation 1.7), where the indeterminacy on the energy of the particle (ΔE) increases the shorter the lifetime (Δt) is. One can, then, write the Equation 1.8.

$$\Delta E \Delta t \geq \frac{\hbar}{2} \tag{1.7}$$

$$\Gamma \tau = \hbar \tag{1.8}$$

where Γ is the full width at half maximum (FWHM) of the core-excited state. This statement shows that for a given atomic photoelectron spectrum, the narrower peaks correspond to core-ionized states with longer lifetimes. The Lorentz lineshape (Equation 1.9) describes very well the line shapes corresponding to the lifetime broadening of exponentially decaying states.

$$P(E_k) = \frac{\Gamma}{2\pi \left(\frac{\Gamma^2}{4} + E_k^2 \right)} \tag{1.9}$$

where the Lorentz distribution is a function of the photoelectron kinetic energy, E_k. The lifetime broadening is the limit of spectral resolution in photoelectron spectroscopy. Nonetheless, other factors also affect the total resolution of the core level photolines. The experimental contributions as, for example, the spectrometer resolution, the thermal Doppler effect, and the photon bandwidth also play a role in the total resolution of a photoline. The sum of these contributions is well described by a Gaussian distribution. Therefore, the total resolution of a photoline is usually described by Voigt function, which is a convolution of a Lorentzian and a Gaussian function. In the subsection 2.2.4, we present a methodology to obtain the total resolution as well as the photon bandwidth and the spectrometer resolution through the analysis of the Argon 2p photoline together with the Argon LMM Auger lines.

1.3 Photoionization, Photoexcitation and Relaxation Processes

One can describe the electronic structure of a chemical system by partitioning it into valence levels and core levels. The valence level corresponds to the outer electronic shells, where the orbitals are more delocalized, and the energy required to extract an electron is in the order of a

few eV. In molecules, the outer electrons interact and are involved in the chemical bond. The core level is related to the inner electronic shells of quite localized orbitals with the atomic character since the core electrons do not usually participate in chemical bonding. The high binding energy of the core electrons range from 100 eV to 1000 eV. Starting from the fundamental aspects of core-level spectroscopy, the first step is to understand the creation of a core-hole. Essentially, a chemical system can be core-excited by the absorption of an X-ray photon to an unoccupied state below the ionization threshold (photoexcitation) or above the ionization threshold (photoionization). An atom with a core-hole is quite unstable so that the system will decay to minimize its energy either through radiative (fluorescence) and non-radiative (Auger decay) channels. These two decay channels compete with each other, and the decay probability of either decay path depends on the atomic number, Z, as presented in Figure 1.2. [7] We observe that at low Z, the Auger decay channel dominates over fluorescence. The two curves intersect around $Z = 30$, the Zinc atom, for the K-shell.

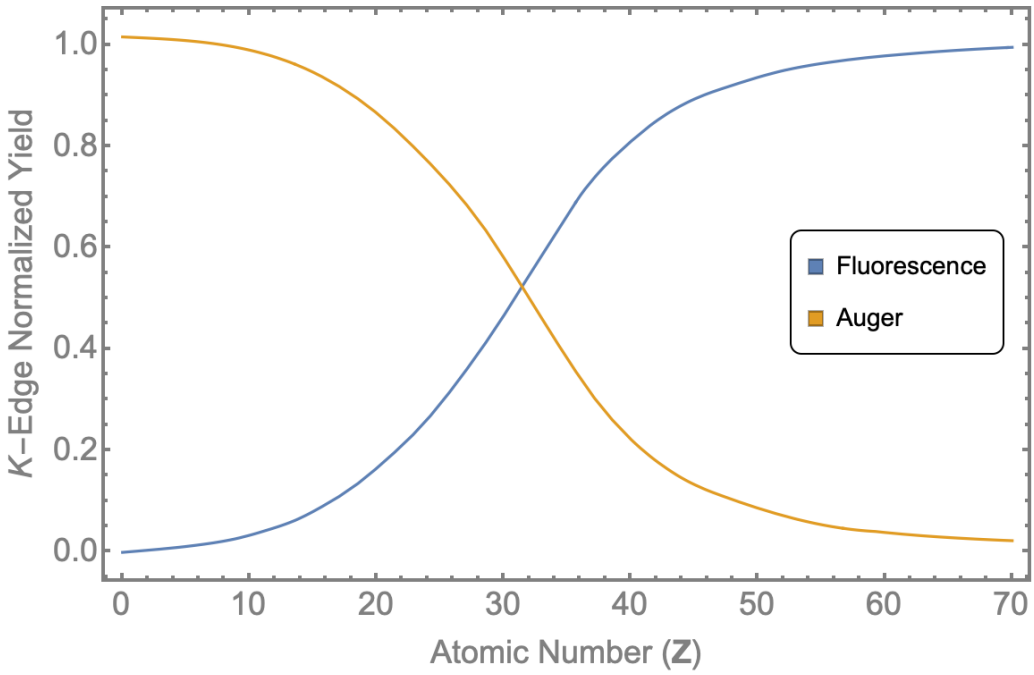

Figure 1.2: *The Fluorescence and Auger yields for $K-$shell vacancies as a function of the atomic number, Z.*

If the core-hole is created by the core-ionization process, the subsequent non-radiative decay is named normal Auger decay. A schematic representation of the core ionization process is presented in Figure 1.3a. First, the X-ray photon excites the core electron to an unbound state (i.e., emitted to the continuum). This emitted electron is the photoelectron. A core-ionized state

with a core-hole is created, and then the electronic system becomes quite unstable. Subsequent to the ionization, the system relaxes by filling the core vacancy with an electron from an upper shell. The remaining energy is transferred to a third electron, ejected to the continuum as the so-called Auger electron. In this case, the final state configuration has two-holes (2-h state), and the atom is, therefore, doubly-ionized. One can easily distinguish the photoelectron, and the normal Auger electron lines since the kinetic energy of the normal Auger electron is independent of the photon energy, which is not the case for the photoelectron.

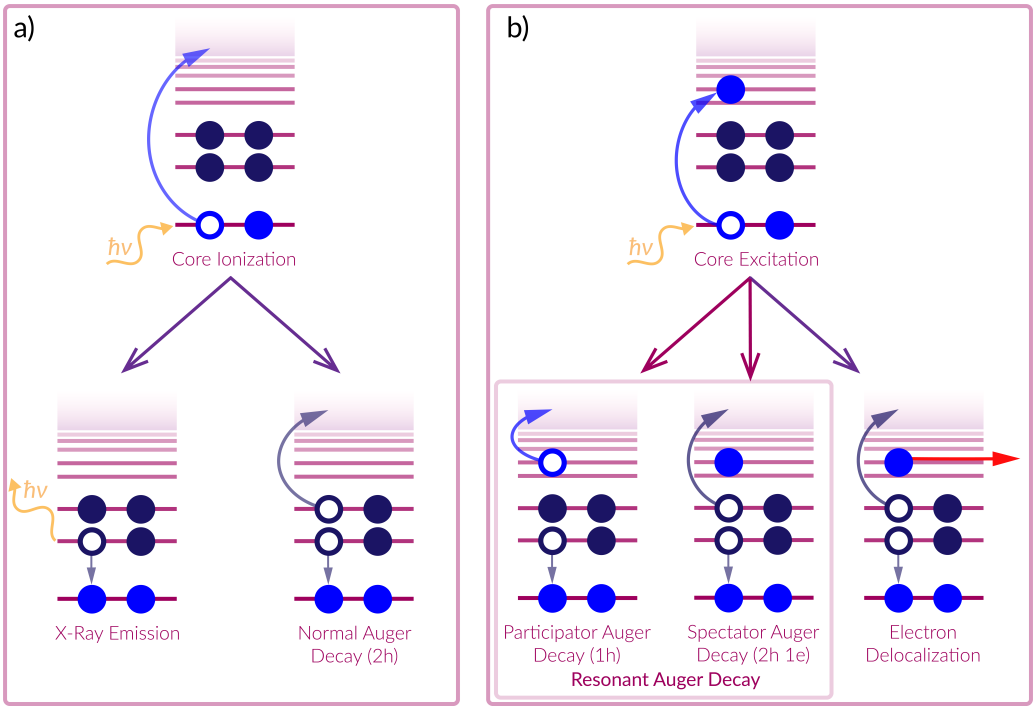

Figure 1.3: *Pictorial representation of relaxation dynamics following core-ionized (a) and core-excited (b) states. Note that in panel a) we also represent a photon's emission with energy hν, the radiative decay process following the core-ionization. The radiative decay pathway competes with the nonradiative decay channel, where an Auger electron is ejected. We focus our discussion on the description of nonradiative decay processes.*

For the core-excitation, one can refer to the subsequent non-radiative decay process as the "resonant Auger effect". In this case, two mechanisms are possible: the so-called participator or spectator Auger decays. These two processes can be distinguished depending on the behavior of the core-excited electron during the relaxation. The X-ray photon excites the chemical system and the core-electron is promoted to an unoccupied valence orbital. In the relaxation process, an electron from a higher shell fills the core-hole. The remaining energy can be transferred to the resonantly excited electron in the valence orbital, and it is emitted as the participator Auger

electron. The configuration of the final state is singly-ionized (1-h state). For spectator Auger decay, the electron which was initially promoted to a valence orbital remains there and does not participate in the decay process. The spectator Auger decay leads to two-holes one-particle (2-h 1e) final state configurations (singly-ionized atom). Alternatively, the resonantly excited core-electron can delocalize over the molecular orbital. In this case, the system remains singly charged, as the delocalized electron does not leave to the continuum. All processes are presented by the pictorial representation in Figure 1.3b.

1.4 Resonant Auger Spectroscopy

The majority of the investigations presented in this thesis deals with resonant Auger spectroscopy as the spectroscopic tool. As shown in the previous section, in the Auger decay, a core electron is promoted to an unoccupied molecular orbital and, in the relaxation process, an Auger electron is emitted. We performed resonant Auger spectroscopy employing the synchrotron light available in the third-generation SOLEIL synchrotron facility. The bandwidth of the monochromatized hard X-ray radiation at the GALAXIES beamline is smaller than the natural lifetime width of the core-hole created in our experiments, allowing us to reach the so-called Raman conditions, which will be detailed in the following. Considering the importance of resonant Auger spectroscopy for our work, it is essential to introduce the basic aspects of the theory related to this technique.

1.4.1 X-ray Scattering Theory

The development of X-ray scattering experiments is based on the diffraction scattering [8], and spectroscopy [9], first in emission and then in absorption, in the 1910s, which followed the earlier discovery of X-rays by Röntgen [10]. At that time, it was revealed that the X-ray energies were element-specific and sensitive to the chemical environment [11]. Following, non-resonant fluorescence spectroscopy technique was developed in the hard X-ray region. Most of the investigations using hard X-rays at this time addressed the chemical shift of core-to-core X-ray emission. Therefore, these investigations made it possible to have a large database of such chemical shifts, and the underlying mechanism was well-understood [12–15]. Next, in the 1920's the Auger [16, 17] effect and Raman [18] effect were discovered. While the Auger effect was not explored due to the lack of electron analyzer technology, the Raman effect was rapidly established.

The Indian physicist Sir Chandrasekhara Venkata Raman found that monochromatic light in the visible (optical) wavelength region could change its wavelength when scattered from a material. The Raman scattering concept was first used in the optical wavelength region. In contrast to elastic X-ray scattering, which is an intense coherent process, radiative inelastic X-ray scattering is very weak. This is the main reason that X-ray inelastic scattering experiments were scarce in the aera of conventional X-ray tubes experiments. To penetrate the resonant region, extremely bright, well-collimated sources are necessary. These requirements only were fulfilled with the development of the synchrotron facilities.

The modern theory of X-ray Raman scattering (XRS) was developed in the 1970s ([19, 20] and references therein) and is based on the classical investigations by Kramers and Heisenberg [21] and Weisskopf and Wigner [22, 23]. The development of synchrotron radiation as an exciting/ionizing source after the 1950s, in particular, the rise of the third-generation synchrotron sources in the 1970s (detailed in Section 2.1), offered great advantages compared to laboratory sources. The tunability of the synchrotron sources enables the selective photo-excitation of the target systems. A core or valence electron is promoted to an empty level, and it is possible to follow the dynamics of the created intermediate neutral excited-state, i.e., resonant photoemission. The high intensity implies that the monochromatization can be driven far, not only to excite single electronic states exclusively but to produce widths of the exciting photon beam that are narrower than the lifetime width of the resonant level. Concomitant to the development of the synchrotron facilities, the advances in dispersive and detection elements were essential to achieve balanced spectroscopic setups to perform X-ray Raman scattering experiments. In the 1980s, Brown *et. al.* [24], observed the so-called resonant Raman effect, which can be considered a breakthrough and has been cited in many publications since then. This effect will be detailed later in this subsection. In the 1990s, many new physical phenomena in the field of XRS were unraveled and studied for both the gas and condensed phases ([20] and references therein). In the next paragraphs, we explained the XRS theory and detailed the first as well as the more recent studies using the techniques related to this theory.

The X-ray Raman scattering theory deals with the interaction of X-ray photons with a target chemical system (atoms, molecules, or solids), creating a core-excited state and the following relaxation from this state. The basis of the theory is to consider the Auger electrons in the nonradiative decay (or photons in the radiative decay) emitted in the relaxation process as

being scattered off upon photoabsorption. When the frequency of the incident X-ray photons is tuned below or closely above the core-ionization threshold, resonant core-excitation occurs. This case is commonly referred to as resonant X-ray scattering or X-ray Raman scattering. The shapes of resonant X-ray emission spectra depend on the creation of the core-excited state, being strongly frequency-dependent when the excitation frequency approached the X-ray photoabsorption threshold. This means that the excitation and deexcitation processes cannot be disentangled so that it is treated as a one, non-separable, scattering event. For this thesis, we rely on the description of nonradiative X-ray Raman scattering.

The interaction between a target chemical system and the radiation field is described by the dipole operator, $\hat{D}$. Thus, the photoabsorption cross-section is given by the Equation 1.10.

$$\sigma_{abs} \propto |\langle \Psi_c | \hat{D} \cdot \mathbf{e} | \Psi_o \rangle|^2 \tag{1.10}$$

where $\mathbf{e}$ is the polarization vector of the incoming X-ray photon, and $|\Psi_c\rangle$ and $|\Psi_o\rangle$ correspond to the core-excited state and the ground state, respectively. The Perturbation theory [19] can be applied to obtain the Kramers-Heisenberg formula (Equation 1.11) [21], which describes the differential cross-section ($\sigma(\omega, \omega')_{Res}$) of the resonant X-ray Raman scattering.

$$\begin{aligned} \frac{d\sigma(\omega,\omega')_{Res}}{d\omega'} &\propto \sum_f |F_f|^2 L(\omega - \omega' - \omega_{fo}, \Gamma_f/2) \propto \\ \propto \sum_f \left| \tilde{\beta}_f \sum_c \frac{\langle \Psi_f | \hat{Q} | \Psi_c \rangle \langle \Psi_c | \hat{D} | \Psi_o \rangle}{\omega - \omega_{co} + \imath \Gamma_c/2} \right|^2 & L(\omega - \omega' - \omega_{fo}, \Gamma_f/2) \end{aligned} \tag{1.11}$$

where F_f is the Kramers-Heisenberg scattering amplitude, $\sum_f$ and $\sum_c$ represent the sum over all the final and intermediate states, respectively. The ejected Auger electron's kinetic energy is given by the term ω'. The resonant energy of the transition from the ground to the intermediate state is given by the term ω_{co} whereas ω_{fo} stands for the energy difference between the initial and final states. $L(\omega - \omega' - \omega_{fo}, \Gamma_f)$ is the Lorentzian function with FWHM Γ_f, which takes into account the conservation of energy during absorption of the photon and the emission of the Auger electron. The lifetime broadening of the intermediate and the final states are represented by the terms Γ_c and Γ_f, respectively. $|\Psi_o\rangle$, $|\Psi_c\rangle$, and $|\Psi_f\rangle$ represent an initial, intermediate, and final state wavefunctions of the chemical system, respectively. $\hat{D}$ and $\hat{Q}$ are the dipole and Coulomb operators, respectively. For the case of radiative decay, the Coulomb operator is replaced by the dipole operator. Finally, all the unessential constants are included in $\tilde{\beta}_f$. In the scope of the Born-Oppenheimer approximation, the total wavefunctions can be factorized into

an electronic and a nuclear part, as shown by the Equation 1.12.

$$\begin{aligned} |\Psi_o\rangle &= |\phi_o\rangle|\psi_o\rangle \\ |\Psi_c\rangle &= |\phi_c\rangle|\psi_c\rangle \\ |\Psi_f\rangle &= |\phi_f\rangle|\psi_f\rangle \end{aligned} \tag{1.12}$$

where $|\phi_o\rangle$, $|\phi_c\rangle$, and $|\phi_f\rangle$ corresponds to the nuclear part and $|\psi_o\rangle$, $|\psi_c\rangle$, and $|\psi_f\rangle$ stands for the electronic part of the wavefunctions $|\Psi_o\rangle$, $|\Psi_c\rangle$, and $|\Psi_f\rangle$, respectively. The transition operators can be factored out, together with the electronic parts of the total wavefunctions, if they do not strongly depend on the molecular geometry, following the Franck-Condon approximation. Then, one can write the Equation 1.11 considering only the nuclear wavefunctions, as shown by the Equation 1.13.

$$\frac{d\sigma(\omega,\omega')_{Res}}{d\omega'} \propto \sum_f \left| \beta_f \sum_c \frac{\langle\phi_f|\phi_c\rangle\langle\phi_c|\phi_o\rangle}{\omega - \omega_{co} + \imath\Gamma_c/2} \right|^2 L(\omega - \omega' - \omega_{fo}, \Gamma_f/2) \tag{1.13}$$

where $\langle\psi_f|\hat{Q}|\psi_c\rangle$ and $\langle\psi_f|\hat{D}|\psi_c\rangle$ are included as constant in β_f. The Equation 1.13 is the simplified form of the Kramers-Heisenberg formula (Equation 1.11) referred to as the "standard Kramers-Heisenberg equation". This equation describes the resonant part of the Auger process. However, to have a full description of the scattering process it is necessary to include the other pathway involved in the process: the direct decay channel from the ground electronic state to the final electronic state. A third term required for the full description of the cross-section appears from the interference between the resonant and direct decay pathways. For this thesis, we rely on the resonant part of the process. In any case, in the vicinity of a photoabsorption resonance, the resonant process is much stronger than the direct process, and then, these terms can be neglected.

Furthermore, an important observation from Equation 1.13 is that it depends essentially on the square of the overlap between the initial and intermediate states during the photon absorption and the square of the overlap between the intermediate and final states during the Auger electron ejection. Essentially, these are square overlap matrix elements, i.e., the Franck-Condon factors. Therefore, the Franck-Condon factors can be described following the standard Kramers-Heisenberg formula.

We are going to focus our discussion on atoms. In this case, the core-excitation is from the ground state to a well-separated resonant intermediate state, which decays into a single final state. According to the X-ray Raman scattering theory, the Auger decay is considered

as a scattering event from an initial state, consisting of an incoming photon and the system in its ground state, to a final state, where an Auger electron is ejected, leading to a singly-ionized system. The core-excited state, i.e., the intermediate state, can be thought of as a bandpass filter so that it selects the photons with suitable energy, $\hbar\omega$, for the scattering process. This photon energy is selected around the nominal resonance energy ω_{co} (we normalized $\hbar = 1$ for convenience) by our "bandpass filter" in a range limited by the lifetime broadening of the intermediate state (Γ), which has a Lorentzian distribution ($L_c(\omega - \omega_{co},\Gamma)$) with width Γ. According to the energy conservation principle, the absorption of a photon with energy ω results in an Auger electron with kinetic energy E_{Auger} (Equation 1.14).

$$E_{Auger} = \omega - (E_f - E_o) \tag{1.14}$$

where E_o and E_f represent the energy of the ground electronic and final electronic states, respectively. For molecular cases, instead of electronic states, we treat them as vibronic states. Note that the difference between E_f and E_o is the binding energy of the singly-ionized final state.

Then, the probability of absorption of a photon with energy ω leading to the emission of an Auger electron with kinetic energy E_{Auger} is related to the Lorentzian distribution of the intermediate state, $L_c(\omega - \omega_{co}, \Gamma)$. If the exciting radiation bandwidth is very large, it can be taken as a constant over the range of interest, and this distribution will be Lorentzian. However, practically the exciting radiation has a limited bandwidth. The photons form a band distribution given by the spectral function $\Phi(\omega - \omega_m, \gamma_m)$, which is a Gaussian function that represents the shape and width of the photon band, centered at ω_m and with width γ_m. We can, then, write an equation for the Auger electron energy distribution presented by the Equation 1.15.

$$P(E_{Auger}) \propto L_c(\omega - \omega_{co}, \Gamma)\Phi(\omega - \omega_m, \gamma_m) \tag{1.15}$$

where it is assumed that the considered final state is stable against further decay during the core-hole lifetime. The Equation 1.15 has important consequences. As a simple product of two functions, if the widths of these functions are quite different, then the distribution $P(E_{Auger})$ will be dominated by the narrower one. If a large photon bandwidth is used, then the natural lifetime width Γ will govern the linewidth in the final Auger spectrum, which we call natural $P(E_{Auger})$. In opposite, for a very narrow photon bandwidth, γ_m governs the Equation 1.15, leading to the so-called "subnatural" linewidths in the final Auger spectrum, which gives rise to

the resonant Raman effect. In other words, the total experimental resolution, in this case, is better than the natural lifetime broadening of the core-excited intermediate state. The resonant Raman effect was first observed for Xe resonant photoemission spectrum around the 2p edge by Brown *et. al* [24]. The corresponding experimental conditions are referred to as Auger resonant-Raman conditions. In such conditions, the excitation and deexcitation processes can not be disentangled in a two-step framework. Therefore, the whole phenomenon is considered as scattering and treated in a one-step picture. [25]

An important consequence of the distribution function $P(E_{Auger})$ connected to the excited state resonance phenomena can be observed not only when the maximum of the distribution function of the photon band is tuned to the nominal resonance maximum but also at values detuned from it, although with reduced intensity. $P(E_{Auger})$ is centered around the Auger electron energy $E_{Auger,0}$ if $\omega_m = \omega_{co}$, meaning that the excitation energy is tuned exactly on resonance. One can detune the excitation energy from the resonance and, in this case, the maximum of the electron energy is displaced from $E_{Auger,0}$. [24, 26, 27] This displacement is written as shown in Equation 1.16, as a function of the photon energy detuning.

$$\Omega = \omega_m - \omega_{co} \tag{1.16}$$

Here, if we consider an excitation of the target system by a large photon bandwidth, then $P(E_{Auger})$ shows no dispersive behavior as a function of the detuning Ω. Meanwhile, the excitation by a narrow photon bandwidth (Auger resonant Raman conditions) results in a linear dispersion of the Auger electron kinetic energy, $E_{Auger,disp}$ against Ω, which is a direct consequence of the Equation 1.14 and is called Raman dispersion law (Equation 1.17).

$$E_{Auger,disp} = E_{Auger,0} + \Omega \tag{1.17}$$

The linear dispersion is observed in the atomic case, but it is more complicated for molecules due to the necessity to take into account nuclear dynamics. In this case, the dispersion law can manifest strong deviations from the linear behavior observed for dissociative intermediate states. In chapter 4 we deal with dissociative states, and therefore we observe such deviations from the linear behavior manifested in the dispersion curves.

Another important consequence of the resonant Raman conditions is the possibility to investigate the composition of resonant Auger spectra as a function of frequency detuning. It has been shown that in a time-dependent approach one can derive an effective duration of scattering,

τ_{eff}, from this process (see Equation 1.18) [20].

$$\tau_{eff} = \frac{1}{\sqrt{\Omega^2 + \Gamma^2}} \tag{1.18}$$

The concept of a duration time, firstly introduced in the soft X-ray range, is one of the most important characteristics of the dynamics of the resonant X-ray scattering process from an experimental viewpoint since it provides a manner to control the scattering time. While the core-hole lifetime Γ is a molecular property and cannot be changed, the frequency of the incoming photons can be chosen. The exponential lifetime of the core-excited states is comparable to the exposure time in an ultrafast camera. [28] In this way, the duration time can be thought of as the spectral formation time.

In detail, the Equation 1.18 allow us to directly relate the duration of the nuclear wavepacket propagation in the excited intermediate state and the detuning between the incident photon and the resonance of the intermediate state, Ω. For the case where Ω is zero (the photon energy is the same as the resonance energy), the wavepacket propagation time is maximum, i.e., the upper limit of the effective duration time is reached ($\tau_{\text{eff}} = \Gamma^{-1}$). In opposite, when the photon energy is detuned from the resonance energy, the duration time is drastically shortened and the nuclear wavepacket does not have enough time to evolve on the core-excited state potential curve before the electronic decay takes place. Therefore, the ultrafast nuclear dynamics can be investigated by knowing the incident photon energy and the lifetime of the intermediate state, which is in the order of a femtosecond in the tender X-rays domain.

The investigation on ultrafast nuclear dynamics was introduced in 1986 by Morin and Nenner for core-excitation of isolated HBr molecules using soft X-rays ($\approx$ 1 keV). [29] The competition between atomic and molecular deexcitation following the Br 3d $\rightarrow \sigma^*$ (LUMO) resonant excitation was studied. The authors observed broad peaks in the Auger electron spectrum corresponding to the molecular deexcitations and narrow peaks, corresponding to the atomic deexcitation signature. This work marked the first observation of the ultrafast dissociation phenomenon. In detail, for cases when the electron is promoted to an orbital with antibonding character, the molecule is in a dissociative state, and the chemical bond is elongated. In other words, the system evolves on a dissociation pathway. In the soft X-ray regime, the lifetime of the intermediate state is a few femtoseconds, comparable to the dissociation time of molecules. The major relaxation path, in this case, is relaxation via resonant spectator Auger, although the participator

Auger decay pathway is also possible, even if less likely (see Section 1.3). If the scattering duration time, τ_{eff}, is long enough, the Auger decay will happen already in a dissociated molecule so that one can observe atomic or fragment lines in the resonant Auger spectrum.

Later, Aksela *et al.* [30, 31] performed similar measurements by resonantly exciting the chlorine atom at 2p threshold in the HCl molecule towards the valence orbitals (LUMO and Rydberg) and showed that the dissociation of the molecule is more favorable when the 2p electron is promoted to the 6σ orbital (LUMO), which has an antibonding character. Then, the molecule is in a dissociative state. When the resonant excitation is towards Rydberg orbitals, the molecule is in a bound state. Following these first observations, in several other studies, ultrafast dissociation phenomenon has been observed for isolated molecules like O_2 [32], HF [33], H_2O [34], NH_3 [35], H_2S [36], among others. In all these studies the competition between molecular deexcitation or deexcitation after fragmentation was observed, because the dissociation time of the molecule is comparable to the lifetime of the core-excited state, which is of a few femtoseconds. To probe nuclear dynamics at such timescales, one can apply a method that represents a milestone in the study of nuclear and electron dynamics, the so-called core-hole clock spectroscopy, detailed in the next section.

1.5 Core-Hole Clock Spectroscopy

The core-hole clock method has been first established theoretically and then applied experimentally in the soft X-ray range. The central idea is to use the lifetime of the excited-state with a core-hole as a time reference for study of dynamical processes occurring in a given chemical system. The decay from a core-excited state yields a spectral signature that is characteristic of the target system. Thus, if any other process occurs during the core-hole decay, its fingerprint will be observed in the spectrum. Then, the core-hole lifetime can be used as an "internal clock" to study dynamical phenomena, like ultrafast nuclear dynamics. Recently, the studies using core-hole clock spectroscopy (CHCS) have been extended to the tender X-ray domain, which gives access to the K thresholds of the third-row elements of the periodic table. The $K-$edge core-hole lifetime ranges between few femtoseconds (10^{-15} fs) for light third-row elements and even the attosecond (10^{-18} fs) timescale for deep holes in heavy elements.

The corresponding core-hole clock techniques which enable us to investigate the dynamics

of the systems are referred to as resonant inelastic X-ray scattering (RIXS) and resonant Auger spectroscopy, which are relevant, respectively, to the measurements of X-ray photons or Auger electrons emitted in the course of relaxation of core-excited molecular states. The electronic final states reached upon relaxation are the main difference between these two techniques. In RIXS, the molecule is neutral with an electron in the excited orbital and a single hole. In resonant spectator Auger decay, the molecule is singly charged with an electron in the excited orbital and two holes. The first experiments demonstrating nuclear dynamics in the sub-femtosecond timescale in tender X-ray regime were RIXS measurements on HCl [37], CH_3I [38], and CH_3Cl [39] isolated molecules. More recently, a work investigated the ultrafast dissociation of HCl following deep Cl 1s photoexcitation, and relaxation [40] using RIXS and RAS. The authors observed ultrafast nuclear dynamics leading to bond break as a result of the strong repulsive character of the potential surface. This repulsive character was related to the intermediate states with one or two holes in the 2p inner shells.

1.5.1 Ultrafast Electron Dynamics

Electron dynamical processes are usually investigated through laser pump-probe measurements. In these experiments, an electron is optically excited (i.e., the electron is "pumped" to a higher state), and the excited state is probed as a function of time after the excitation. The first observations of the electron dynamics in molecules using laser pump-probe were in two small diatomic molecules, H_2 and D_2 [41, 42]. The study of electron delocalization processes in complex systems requires to address both the temporal evolution of the electron wave packet and the question at which atomic center the electron was localized before its delocalization. This latter information cannot be provided in probe-pump experiments in the spectral regime of optical transitions. [43] Alternatively to the time-resolved measurements, such processes can be successfully studied in the energy domain using the core-hole clock method. As mentioned in the previous section, for deep core shells, the lifetime of core-hole states is on the sub-femtosecond time scale. This makes CHCS perfectly suitable also for the observation of ultrafast electronic motion [43–48]. Furthermore, the use of tunable monochromatic synchrotron radiation allows controlling the effective core-hole lifetime, thus providing a precise tool for probing the electron transfer process. [20] Finally, due to the excitation of the core shells, the CHCS method allows selective interaction with a specific atom in a molecule. The site-specificity is essential for a localized initiation of

the electron delocalization process.

The feasibility of the application of CHCS to the study of sub-femtosecond electron dynamics was demonstrated in the gas-phase. A study demonstrated that RIXS spectroscopy in isolated carbon disulfide CS_2 molecules could provide access to X-ray-induced electron dynamics in a molecule occurring on attosecond timescale [49]. At large photon-energy detuning below the first absorption resonance, the RIXS profile is dominated by the onset of the electron dynamics triggered by a coherent excitation of multiple electronic states. Electron dynamics occur on the characteristic time scale in the attosecond range, determined by the spacing of the coherently excited intermediate states. The RIXS profile is determined by the interplay of the effective scattering duration and the characteristic time of the electron wave packet evolution. Marchenko *et. al.* [50] combined RIXS and resonant Auger spectroscopy to provide complementary information on the dynamic response of resonantly excited molecules. The authors proposed an experimental method to obtain information on the lifetime and potential energy surface of dissociative single-core-hole (SCH) and double-core-hole (DCH) states in molecules, core excited with hard X-ray radiation using dissociative I $3d^{-2}$ double-core-hole state of CH_3I molecule as the showcase. These potential energy surfaces are otherwise difficult to obtain by *ab initio* calculations for molecules containing heavy atoms and are predictive of the dynamical behavior of the photoexcited systems.

In condensed-phase, non-local electronic decay processes in solutions were demonstrated in [51, 52]. Furthermore, electron transfer between the solute and the solvent was observed in aqueous solutions of potassium chloride [53] and several aqueous iron-containing species [54]. In this thesis, we focused on exploring the potential of CHCS using resonant Auger spectroscopy technique to investigate solid chemical systems. Earlier observations of electron dynamics using resonant Auger spectroscopy were reported in solid-state studies. Previous works demonstrated that the electron transfer from the adsorbed atoms and molecules to the substrate occurs on the timescale of few femtoseconds to hundreds of attoseconds. [43, 55] Noteworthy results were demonstrated on electron dynamics investigations in a genomic DNA molecule in 5'-Guanosine monophosphate (GMP) nucleotide. [56, 57] Powdered samples pressed to a solid substrate were measured by resonant Auger spectroscopy revealing intramolecular electron delocalization on the timescale of attoseconds along the phosphate groups in the DNA backbone and in the aggregated GMP structures. Furthermore, the importance of the structural periodicity for the formation of

the conduction band was demonstrated.

The phenomenon of electron delocalization in periodic structures is also of great relevance in optoelectronics. In this topic, organic optoelectronic devices have been potential candidates for the emerging technologies of solid-state lighting and green-energy applications. [58] The key issue for the efficiency of organic polymers used in photovoltaic devices is the charge transport. In conjugated polymers characterized by a sequence of alternating single- and double-bonds, the electric conduction is formed by the $\pi-$electrons delocalized over several carbon atoms along the polymer backbone. Apart from delocalization of $\pi-$electrons, the important factors for charge transport are inter-chain interactions, $\pi - \pi$ stacking interactions through the aromatic rings and side groups [56]. Recently, studies in thiophene-based polymers suggest the importance of inter-chain interactions for electron delocalization observed in highly oriented polymer films [59, 60]. In our work, we investigated similar systems using resonant Auger spectroscopy to study ultrafast electron dynamics by means of the CHCS. Moreover, we obtained the so-called charge (or electron) transfer rate for an electron in an initially localized orbital in the vicinity of the core-hole transferring to an unoccupied state of a neighbor molecule. Our results are detailed in Chapter 5.

Chapter

2 Experimental Techniques and Instrumentation

Chapter content

2.1 Brief History of Synchrotron Radiation and the Development of Synchrotron Facilities

Synchrotron radiation is the electromagnetic radiation emitted by accelerated charged relativistic particles. Nowadays, it is produced in Synchrotron facilities, which are machines consisting of an evacuated storage ring with high-energy electrons (or positrons) circulating at highly relativistic velocities. Synchrotron radiation was first observed in 1947, in a man-made circular particle accelerator at General Electric Research Laboratory in the United States. On that occasion, it was considered as a "parasitic radiation" since it caused energy loss in the accelerated particles. However, in the mid-50's, Diran Tomboulian and Paul Hartman experimentally demonstrated the spectral characteristics of this radiation. The experiment showed the suitability of synchrotron radiation for absorption measurements and for detector calibration in the ultraviolet

region [61]. This work stimulated the interest in the application of synchrotron radiation, which led to the construction of the first facility in 1961, named Synchrotron Ultraviolet Radiation Facility (*SURF I*) in Washington, D.C. It defined the beginning of the first generation sources.

Thanks to the increasing interest in the research using synchrotron radiation in the upcoming years, and to the development of efficient storage rings for long-term operations, dedicated synchrotron facilities were constructed around the 1980s. The development of this specific installation establishes the beginning of the second generation of radiation sources. At this time, synchrotron radiation was mostly produced from "bending magnets", which are a set of dipole magnets located at the curved sections of the storage rings and induce the electrons to follow a circular path. Therefore, the electrons were accelerated by a centripetal force, producing the synchrotron radiation in a tangential direction. The radiation produced by a bending magnet is characterized by a broad energy range spectrum.

Despite the high intensity, the radiation produced by the bending magnets has limited brilliance and flux, which are important properties of the photon beam. These two properties determine the "quality" of the photon beam produced by a X-ray source. The so-called "radiation brilliance" is a function of the photon energy (Equation 2.1). The numerator indicates the number of photons which are emitted by the source per second. In the denominator, the collimation of the beam, given in $mrad^2$, describes how well this source is able to focus the beam in a spot of an area given in mm^2. Finally, the term "0.1% *bandwidth*" stands for the relative photon energy range covered by the source. The spectral flux is defined as the number of photons emitted per second per 0.1% bandwidth, which means that the brilliance describes how the flux is distributed in phase-space. In other words, a high brilliance is given by a high flux in a small spot size with low beam divergence.

$$Brilliance = \frac{photons/second}{(mrad)^2(mm^2\text{source area})(0.1\%bandwidth)} \tag{2.1}$$

The instrumental development in accelerator physics over the subsequent years allowed the inclusion of the insertion devices in the straight sections of the storage rings overcoming the bending magnets's limitations. The incorporation of these devices in the synchrotron facilities marked to the third-generation installations in the 1990s. The insertion devices are periodic structures consisting of an array of alternated polarity magnets that forces the electrons to

deflect in a harmonic oscillatory path horizontally with respect to the storage ring [62]. In this way, the intensity of the emitted radiation beam increases proportionally to the number of periods of the device.

The insertion devices can be divided into two types named wigglers and undulators. In the wigglers, strong magnetic fields deflect the electrons laterally and it makes them "wiggle" by a large amplitude, which increases the angular divergence of the emitted radiation beam. Therefore, the wigglers produce a broad radiation spectrum similar to the bending magnet spectrum but much more intense due to the contribution of their multiple magnetic dipoles and their radiation energy range is shifted to harder X-ray. The undulators consist of moderate magnetic fields, which causes a small deflection of the electrons from their orbit. The radiation produced in each turning is emitted in a narrow cone, which results in an overlap among the emitted radiation, in both constructive and destructive wave fronts. The spectrum of the radiation produced by an undulator is characterized by regularly separated narrow bands of radiation due to the constructive interference of radiation emitted from each pole. Therefore, one can distinguish the wigglers and the undulators by three factors: the amplitude of the electron deflection from its straight path, the angular divergence of the emitted radiation, and the resulting spectrum.

The light provided by the synchrotron installations is by several orders of magnitude more intense than the radiation produced by conventional sources such as the commercial X-ray facilities. It covers a broad spectral range, unachievable by tuneable lasers. The advantage of synchrotron radiation compared to the available conventional sources is its high brilliance, polarization, and broad spectral range. These features allow the experimental access to information on electronic structure, dynamics, surface and interface properties, and magnetic properties in numerous systems that are inaccessible with conventional sources.

2.2 SOLEIL Synchrotron Radiation Facility

The work developed in this thesis was carried out at the French third-generation synchrotron radiation facility SOLEIL, which stands for **S**ource **O**ptimisée de **L**umière d'**E**nergie **I**ntermédiaire du **L**ure. The spectral range covered by this 2.75 GeV synchrotron source goes from far infrared to hard X-ray. The schematic representation in Figure 2.1 shows the SOLEIL facility's main components.

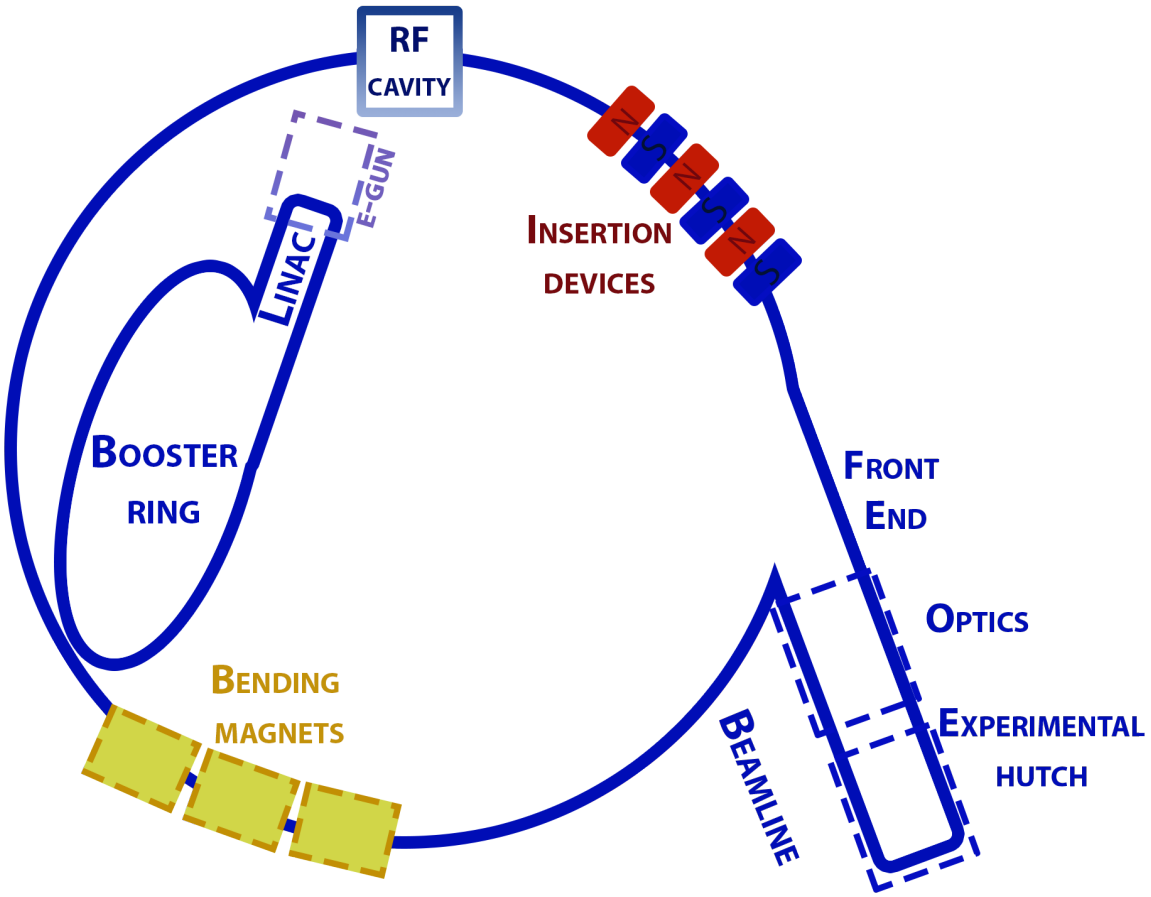

Figure 2.1: *Schematic representation of the third-generation SOLEIL synchrotron facility.*

In order to produce synchrotron radiation, first an electron beam emitted by an electron gun is accelerated to the linear accelerator (Linac). Inside the Linac, the electron beam reaches the high energy of about 100 MeV. In the next step, these electrons are oriented towards the booster ring thanks to a set of electromagnets where they will be further accelerated to match the energy of the electrons in the main storage ring, i.e., to 2.75 GeV in the case of SOLEIL.

Once reached the operating energy, the electron beam is injected into the $113m$ diameter storage ring, which holds the electrons on a closed path by using magnet lattices. The magnet lattice is constituted by an array of bending magnets, insertion devices, quadrupoles, and sextupoles. The bending magnets are located in the storage ring's curved sections, whereas the insertion devices are placed at its straight sections. These magnets and devices cause the loss of energy in the electrons due to the emission of synchrotron radiation (see subsection 2.1 for a detailed explanation). Then, the energy lost during this process is restored by a radiofrequency (RF) accelerating cavity. Furthermore, the quadrupole magnets focus the electron beam and balance the Coulombic electronic repulsion and the sextupole magnets correct the chromatic

aberrations resulting from the focusing by quadrupoles.

The beamlines are placed tangentially to the storage ring. The "front-end" isolates the beamline vacuum from the storage ring vacuum, monitors the beam's position, and defines the synchrotron radiation's angular acceptance through an aperture. Furthermore, the "front-end" also blocks the undesired radiation during the access to the experimental optical set-up and hutches.

2.2.1 GALAXIES beamline

GALAXIES is an undulator beamline optimized to operate in the energy range from $2.3keV$ to $12keV$ which covers the electromagnetic radiation from tender to hard X-ray regime [63]. The beamline holds two experimental end-stations: one dedicated to Resonant Inelastic X-ray Scattering (RIXS) and another one dedicated to Hard X-ray Photoelectron Spectroscopy (HAXPES), which are powerful techniques for characterizing the electronic properties of atomic and molecular systems. The literature detailing RIXS end-station can be found in reference [63]. All of the work of this thesis was performed using HAXPES end-station.

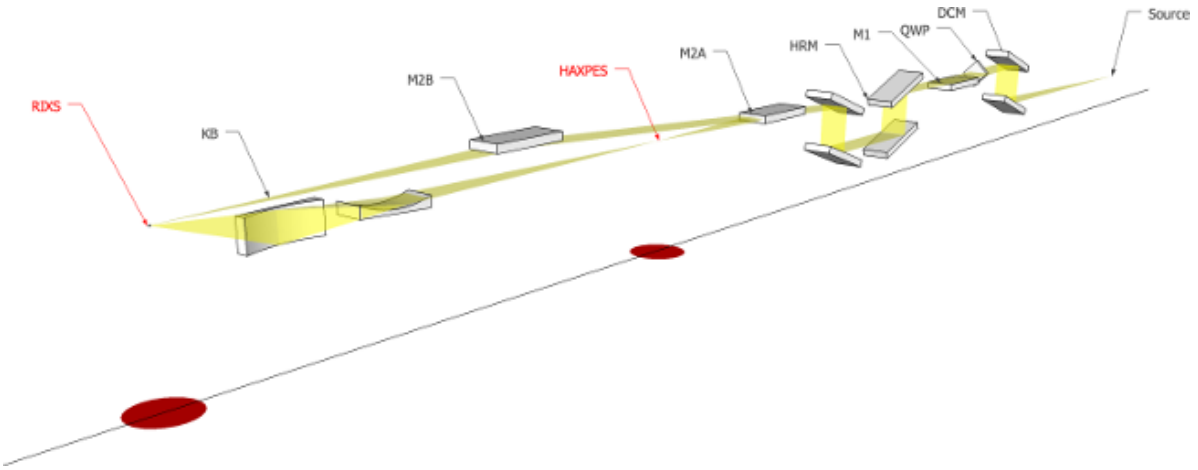

Figure 2.2: *Pictorial representation of the GALAXIES beamline layout [64].*

A schematic representation of the GALAXIES beamline is shown in Figure 2.2 [64]. The beamline is equipped with an in-vacuum 20 mm-period U20 undulator composed of 98 periods [63]. The undulator modulates the electrons' trajectory leading to their acceleration. The calculated U20 photon brilliance is presented in Figure 2.3 [64], showing that the maximum of brilliance is reached at 2.3 keV photon energy. The incident radiation beam reaches the beamline with a 100% horizontal linear polarization (H). It is possible to select the desired

photon energy thanks to a double Si(111) crystal monochromator (DCM). Following the DCM, the quarter wave-plate (QWP) allows switching between linear and circular polarization. The M1 collimating spherical mirror has two different coatings: Carbon coating for low photon energies (2.3 keV − 6 keV) and Palladium coating, for energies above 6 keV up to 12 keV. The recently commissioned four-bounce high-resolution monochromator (HRM) placed consecutively to the M1 mirror makes possible to further narrow the photon energy bandwidth to about ≈100 meV at 4 keV. The M2 mirror, which consists of Si toroidal mirrors coated with Pd, focuses the collimated beam onto the HAXPES (M2A) and RIXS (M2B) end-stations. The KB optics focus the beam at the RIXS sample location and are coated with both Rhodium and B_4C layers.

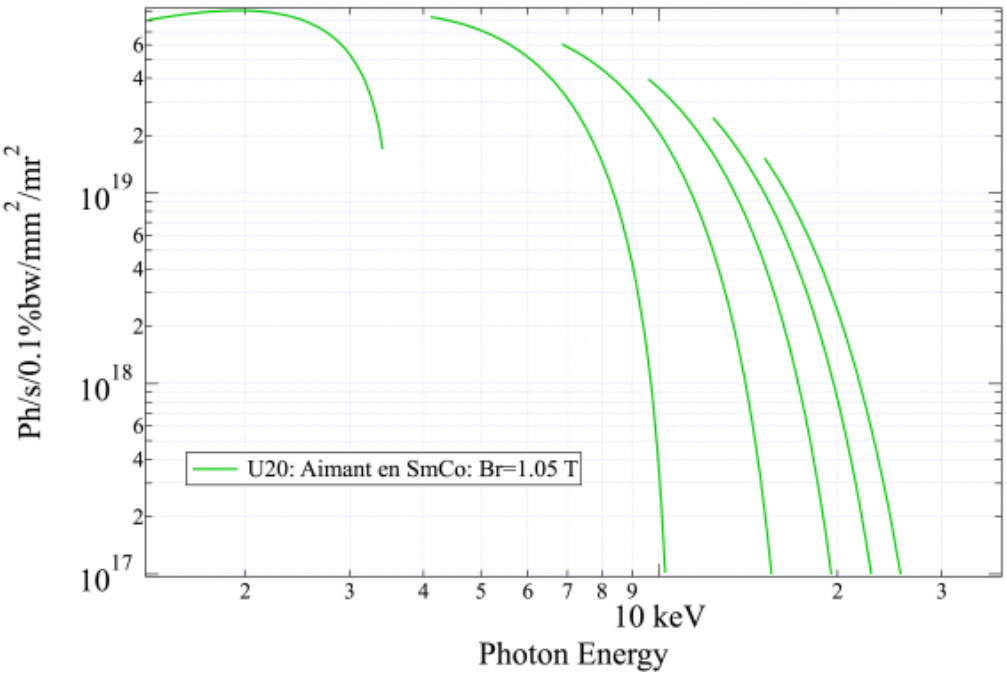

Figure 2.3: *Calculated brilliance as a function of the photon energy in the U20 undulator employed in the GALAXIES beamline (Extracted from [64]).*

2.2.2 Hard X-ray Photoelectron Spectroscopy

The experimental investigations presented in this thesis were performed by Hard X-ray Photoelectron Spectroscopy. We explored the potential of HAXPES at the GALAXIES beamline by performing studies on the electronic structure and ultrafast electron dynamics from noble-gases to larger organic chemical systems in both gas phase (see Chapters 3 and 4) and solid phase (Chapter 5), respectively. This section describes the most recent studies demonstrating

the HAXPES technique and presents the development of new HAXPES experimental stations in other synchrotron facilities. An extensive and detailed review on hard X-ray photoemission spectroscopy can be found in the reference [65].

HAXPES is photoelectron spectroscopy performed in a high-energy, i.e., tender to hard X-ray regime (from $\approx$ 2 to 12 keV). Hence, deeper electronic levels can be accessed giving rise to new studies on the inner-shell electronic structure of atoms and molecules, as well as the electron and nuclear dynamics of these systems. Taking advantage of the state-of-the-art photon energy and electron kinetic energy resolution achieved in the past decade, one can carry out experiments that before were only well established in the soft X-ray regime and could not be explored in harder X-ray region at that time. Today, the leading research on HAXPES in isolated atoms and molecules is performed using the experimental apparatus available in the GALAXIES beamline. The main topics investigated by our research group on atoms and small molecules in gas phase are briefly outlined below. A review of our group's publications on HAXPES can be found in reference [1].

Post-Collision Interaction and Electron Recapture

Briefly, the Post-Collision Interaction (PCI) effect occurs by kinetic energy exchange between the photoelectron and the Auger electron in the presence of an atom core-ionized close to the photoionization threshold. This interaction leads to an acceleration of the Auger electron, observed experimentally by the shift of the Auger peak to higher kinetic energies accompanied by the kinetic energy loss of the photoelectron. In the cases in which the photoionization is quite close the ionization threshold, the photoelectron can be recaptured into an unoccupied Rydberg orbital.

The PCI and electron recapture phenomena were studied with HAXPES by measuring the high-resolution Auger spectra following deep core ionization of Argon. [66]. This work, gives a complete picture of the interaction between the photoelectron, the Auger electron, and the Coulombic field of the ion created in this process. It is shown that the position and lineshape of the Auger peaks is strongly affected by the PCI effect. Moreover, a signature of electron recapture by the population of some discrete Rydberg states close to the ionization threshold was observed and confirmed by complementary calculations. We briefly describe in the outlooks of this thesis (Chapter 6) that the approach used in this work can be applied to the investigations

on PCI effects in large molecular systems, as polymers.

Recoil-Induced Effects

The recoil effect can be explained as follows: the photoionization process results in the ejection of a fast photoelectron that leads to recoil of the remaining ion due to momentum transfer. In a hard X-ray regime, this effect cannot be neglected. In atoms, the recoil energy can be dissipated only as translational motion, whereas in molecules, the vibrational and rotational channels are available. For example, the role of translational recoil on the Neon atom was demonstrated by measuring the Auger decay spectra after the Ne 1s ionization. The dramatic changes in the Auger line shapes were attributed to the Doppler effect caused by the translational recoil due to the photoelectron's momentum [67]. The recoil-induced effects were also investigated for the case of the photoionization of molecular systems, in which the excess recoil energy dissipated by vibrational and rotational motions. [68, 69]

Ultrafast Phenomena

The time scale of dynamical processes in atoms and molecules is about few femtoseconds ($10^{-15}s$) or even hundreds of attoseconds ($10^{-18}s$). Atomic interactions, nuclear motion, ultrafast fragmentation and electron dynamics are examples of processes of the sub-femtosecond time scales. The investigation of the dynamics on such ultrafast time scales can be performed using the short-lived core-hole lifetime as an "internal clock", the so-called core-hole clock spectroscopy (See Section 1.5). The access to higher photon energies at GALAXIES allows reaching deeper inner shells with shorter core-hole lifetimes, at the time scale of sub-femtoseconds, making it possible to investigate such processes. [70]

Core-hole clock spectroscopy was applied to HCl and CH_3Cl molecules to reveal the nuclear motion through resonant Auger spectroscopy upon excitation of Cl 1s shell. [71] To describe the Auger decay spectra the authors developed a fit approach that takes into account the electronic state-lifetime interference contributions and ultrafast nuclear dynamics in dissociative core-excited states. Travnikova *et.al.* [72] studied ultrafast fragmentation dynamics in HCl following Cl 1s photoexcitation. It was demonstrated that relaxation via Auger cascade is accompanied by ultrafast nuclear dynamics leading to bond breaking.

Double-Core-Hole Spectroscopy

Double-core-hole (DCH) states are electronic states formed either by two core-shell electrons being ejected into the continuum, or by core-ionization core-excitation, or by a double core-excitation. The mechanisms for the formation of DCH states are given by two different paths, direct and conjugate. The first path occurs in the case of a dipolar ionization and monopole excitation. In opposite, the second path occurs by dipolar excitation and monopole ionization. In other words, because of the $\Delta l = \pm 1$ selection rule one obtains (for an atom) for the direct path: $1s \rightarrow \varepsilon p$ and $1s \rightarrow ns$, with ε being the continuum and n the quantum number for an unoccupied Rydberg orbital. For the conjugate path, one obtains $1s \rightarrow \varepsilon s$ and $1s \rightarrow np$. So, in the direct channel one will have a $p-$wave ($\beta - value = 2$) emission along the axis of the analyzer lens, which is parallel to the polarization of the light at GALAXIES beamline. For the conjugate channel one will have an $s-$wave emission ($\beta - value = 0$). In the case of molecules, both channels can contribute to the same transition. For detailed explanation, see references [73, 74].

Despite electron impact [75] and heavy ion impact [76–78] experiments were performed on Neon many years ago, only few experimental works on DCH by photoelectron spectroscopy and related techniques have been performed until recently, due to the complexity of the required instrumentation. At HAXPES end-station, one can measure one ejected photoelectron at a time, therefore one can measure spectra of the so-called "super shake-up" (satellite) state, and namely 1s photoionization accompanied by shake-up of a core ns or np electron to an unoccupied orbital. The investigations in the DCH pre-edge states of CS_2 and SF_6 at different $K-$edges detailed the analogies and differences between the DCH photoelectron and the absorption spectra of single-core-hole (SCH) states. [79] In a previous work, the hyper-satellite Auger spectrum of Neon, resulting from DCH states was assigned in detail. [80] A high-resolution study in gas-phase water showed nuclear dynamics, particularly the stretching of the O−H bonds, during DCH formation and decay. The authors obtained evidence of ultrafast proton motion by rigorous analysis of the shape and width of the hyper-satellite Auger spectral lines resulting from the decay of the DCH states. [81] Directly related to this work in gas-phase water, we recently investigated single and multiple excitations in DCH states of isolated water molecules leading to dissociative nuclear dynamics. [82] We measured the DCH photoelectron spectrum by irradiating gas phase water molecules with hard X-rays above the Oxygen K^{-2} threshold. $K^{-2}V$ (were V

stands for an electron promoted to a vacant molecular orbital) states and multiply excited states are created by a single-photon absorption and following one-electron emission. Thanks to the high experimental resolution, our analysis revealed dissociative nuclear dynamics in the $K^{-2}V$ states. The strong broadening due to nuclear motion indicates a highly dissociative nature of the multiply excited states.

Other studies using HAXPES

In the last years, many research projects were carried out in GALAXIES by other groups employing HAXPES in solid systems with application in materials science [83]. As an example, a recent work investigated black phosphorus, a semiconductor with desirable optoelectronic properties, by time- and angle-resolved photoelectron spectroscopy [84]. Recently, GALAXIES also started to offer the possibility of employing the bulk sensitive photoelectron spectroscopy in liquid-phase systems, which presents an approach to overcome the surface sensitivity difficulties intrinsic to soft X-rays. A study of aqueous KCl performed using the HAXPES setup in GALAXIES aimed to investigate charge transfer dynamics from the solvent to the solvated ions, opening a prospect to ultrafast chemical dynamics investigation in liquids [85].

Meanwhile, it is essential to mention the fast development of this experimental tool also worldwide. Until present, there are about 25 HAXPES facilities at synchrotron installations around the world. This number is steadily growing as new HAXPES end-stations are being built at MAX IV in Sweden, Argonne National Laboratory in the USA, PETRA III in Germany and SPring-8 in Japan, among others. A brief update on the development of the mentioned new HAXPES set-ups is given below.

Spring-8 Synchrotron Facility, Japan

While at SOLEIL one can perform HAXPES experiments between 2 keV and 12 keV, at Spring-8, hard X-rays up to 35 keV are available. Experiments on isolated atoms and molecules were performed on two RIKEN beamlines (BL29XU and BL19LXU). [86] Moreover, investigations on Xe 1s photoionization and decay [87], and I 1s photoionization and decay in CH_3I and CF_3I [88] were recently performed. Besides the studies on small systems, also investigation on the chemical structure and ferromagnetic properties of oxides thin films were performed. [89–91]

PETRA III Synchrotron Facility, Germany

The HAXPES beamline P22 at PETRA III is in user operation since September 2018. The available energy range to perform HAXPES experiments is from 2.4 keV up to about 15 keV. The setup was designed for studies of functional solid-state nano-materials and catalytic interfaces, with a focus on measurements under operando and/or ambient conditions. [92] Recently, HAXPES was used as a high-sensitive voltmeter to study the evolution of charges. Combined with other spectroscopic techniques, the interface of a material used as a ferroelectric memory device was investigated. [93]

Argonne National Laboratory, United States

A HAXPES setup is under development at the Advanced Photon Source (APS) for experiments using a high-resolution, high-collection-efficiency electron Scienta analyzer, similar to the HAXPES end-station at GALAXIES beamline. Initially, two topics will be exploited. First, experiments to characterize inner-shell resonance and threshold effects by tuning the X-ray energy across K-edges of atoms and small molecules. Second, experiments to characterize DCH states in molecules in which hollow core shells are produced by single-photon absorption and generated by electron correlation. [94]

Max IV Synchrotron Facility, Sweden

The HAXPES setup at Max IV is under development. The apparatus will be dedicated to investigate materials, completing structural data with chemical information, and will be installed at DiffMax, a beamline still in design phase. This beamline will operate in the energy range of about 3 keV to 45 keV. [95]

Additionally, a well-established series of international HAXPES conferences and workshops have been organized since 2003 every two years [96]. Our group was actively involved in the organisation of the most recent edition held in 2019 in Paris. [97].

2.2.3 HAXPES setup at GALAXIES beamline

The components of the HAXPES station are shown in Figure 2.4a [64]. The yellow arrow represents the incoming photons. The setup carries a gas-cell mounted on a four axes-manipulator placed at the bottom of the main chamber, where the gas-phase experiments were performed. The experimental system includes a liquid nitrogen cooling system to reduce the thermal Doppler

broadening contribution (not used in this work) [98]. Furthermore, the station is equipped with a preparation chamber, which was involved in the solid-phase experiments performed in this thesis. The solid samples were mounted in a stainless steel sample plate (standard Omicron-type plate), which was hosted in a two-slot copper sample holder. The sample plates are electrically isolated from the copper block. A photo of the sample holder is shown in Figure 2.4b [64]. The holder is connected to the four axes-manipulator located on the top of the chamber. It is also connected to a He-cryostat for low-temperature measurements (below 15 K), which was not used in this thesis [98]. The mounted samples were transferred to the main chamber, where the measurements were performed. The trajectory of the electrons ejected from the solid sample or from the gas cell directed to the analyzer is represented with the red arrow in Figure 2.4a.

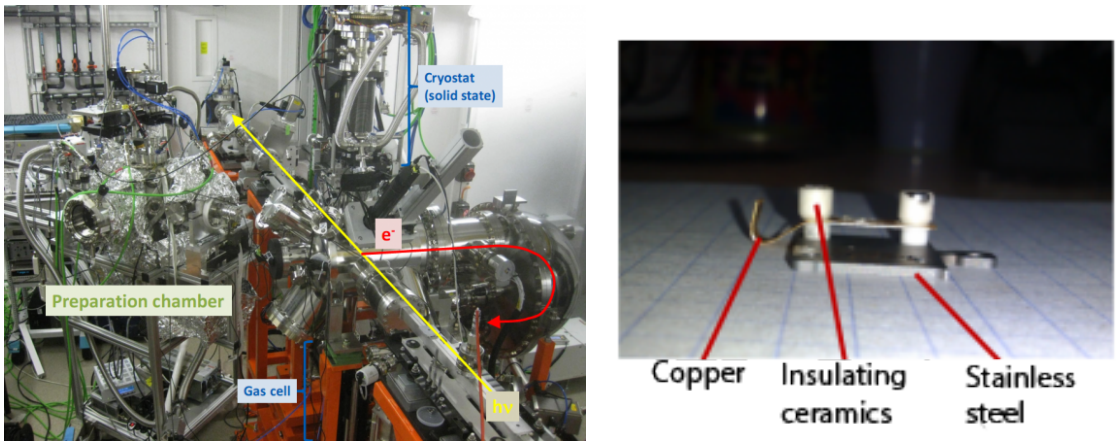

Figure 2.4: *(a): The components of HAXPES setup in the GALAXIES beamline. The yellow arrow represents the incoming photons and the red arrow, the photoelectrons ejected from the samples, and directed to the electron detector. (b): The stainless steel sample holder. Both pictures are adapted from [64].*

The electron kinetic energy in the HAXPES end-station is measured by the state-of-the-art hemispheric analyzer EW4000 VGScienta, mounted parallel to the polarization direction of the incoming radiation. The spectrometer lens can operate in three modes: wide-angle detection (60° acceptance), a high-angular resolution with 45° acceptance, and the transmission mode for high intensities. The analyzer is equipped with a micro-channel plate (MCP) detector coupled to a CCD (charge-coupled device) camera.

A schematic representation of this spectrometer is shown in Figure 2.5. After the photoemission, the ejected electrons go through the set of electrostatic lenses, which adapts the electron

kinetic energy to the set value of the pass energy, E_p, and simultaneously, focuses the electron trajectories onto the entrance slits of the analyser. After passing through the entrance slits, the electrons reach the analyzer's semi-spheric cavity, which consists of two concentric metallic hemispheres of radii R_1 and R_2 (where R_2 is smaller than R_1), floated to the negative potentials $-V_1$ and $-V_2$, respectively. The applied tension deflects the electrons' trajectories as a function of their kinetic energies towards the micro-channel plate (MCP) detector, located behind the exit slits.

The MCP is an electron signal amplifier, which amplifies it by several orders of magnitude compared with the initial signal [99]. The MCP is composed of a glass grid covered with metal. The schematic picture of this detector is represented in Figure 2.6. The sloped channels (micro-channels) enable increasing the contact between the electrons and the walls of the channels, multiplying the signal as following: the incident electron enters in a channel and tears off several secondary electrons accelerated by a high voltage applied between the input and the output electrodes, which creates a cascade process that generates several more electrons. The analyser is equipped with a CCD camera, which allows the tracking of the signal coming from the produced electrons and enabling us to obtain a spatially resolved image of the photoelectron pattern.

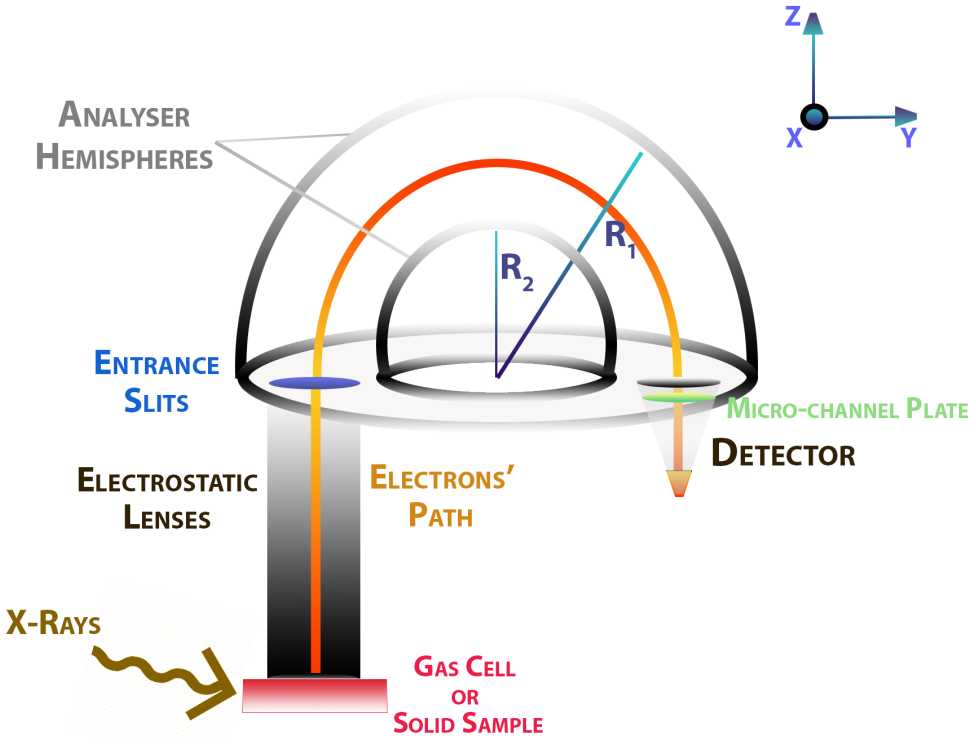

Figure 2.5: *Pictorial representation of a hemispherical analyzer. The electrons ejected from the studied system are collected, focused by the electrostatic lenses, and go into the hemispherical cavity. The electrons with kinetic energy close to the pass energy selected by the user will be detected and analyzed.*

The analyzer resolution is defined in the Equation 2.2, where E_p is the pass energy; ω is the slits width; R is the central radius between the two concentric hemispheres of radii R_1 and R_2; and $\delta\alpha$ is the trajectory deviation of the electron injected inside the hemispheres. An important consequence of Equation 2.2 is that the energy resolution can be improved by decreasing the pass energy and the widths of the slits. However, this improvement (decreasing $\Delta\varepsilon$) leads to signal reduction. Then, longer acquisition times are required to obtain reasonable statistics for the spectrum. A procedure to obtain the analyzer resolution can be found in section 2.2.4.

$$\Delta\varepsilon = E_p \cdot \left(\frac{\omega}{R} + \left(\frac{1}{2}\left(\delta\alpha\right)^2\right)\right) \tag{2.2}$$

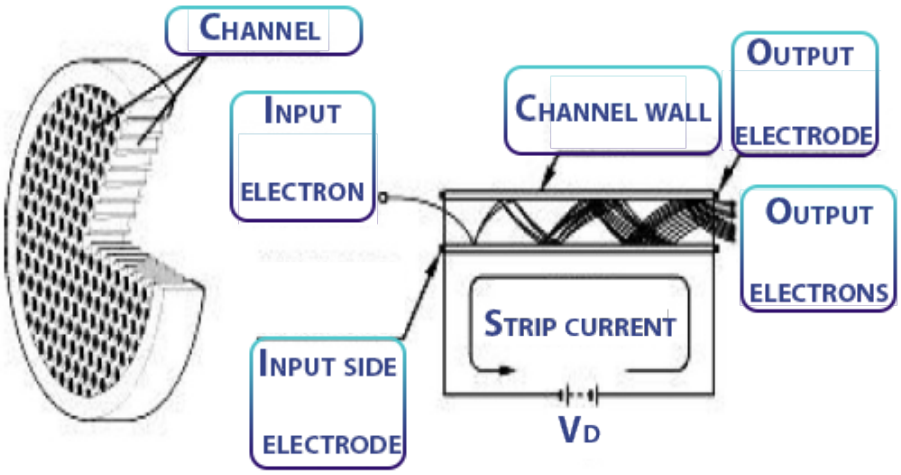

Figure 2.6: *The schematic representation of a micro-channel plate adapted from reference [99].*

2.2.4 Data Treatment

In order to calibrate the experimental data, two steps must be performed. First, the calibration of the kinetic energy scale of the electron spectrometer has to be performed. It can be achieved by measuring a well-known Auger spectrum, which in our case is Argon $L_{2,3}M_{2,3}M_{2,3}$ Auger spectrum. Second, the calibration of the photon energy scale can be established by measuring the kinetic energies of well-known photoelectron lines, which in our case is Argon $2p$ photoelectron spectrum. We also obtained the spectrometer resolution, the total resolution, and the photon bandwidth by using the Argon $L_{2,3}M_{2,3}M_{2,3}$ Auger spectrum and the Ar $2p$ photoelectron spectrum.

The Spectral Analysis by Curve Fitting (SPANCF) macro package developed by E. Kukk *et. al.*, designed for *IgorPro* software was employed to perform the curve fitting in all cases. More details on this package can be found in Reference [100].

Energy Calibration

The electron kinetic energy scale calibration was performed by measuring the Argon $L_{2,3}M_{2,3}M_{2,3}$ Auger spectrum. Figure 2.7 shows this spectrum measured at 2300 eV of photon energy as an example. The three spectroscopic terms ^1S, ^1D and, ^3P result from the two holes in the $3p$ orbitals in the final state. We fitted the peaks by using Voigt functions, the result of which is represented by a blue line. The red circles represent the experimental points.

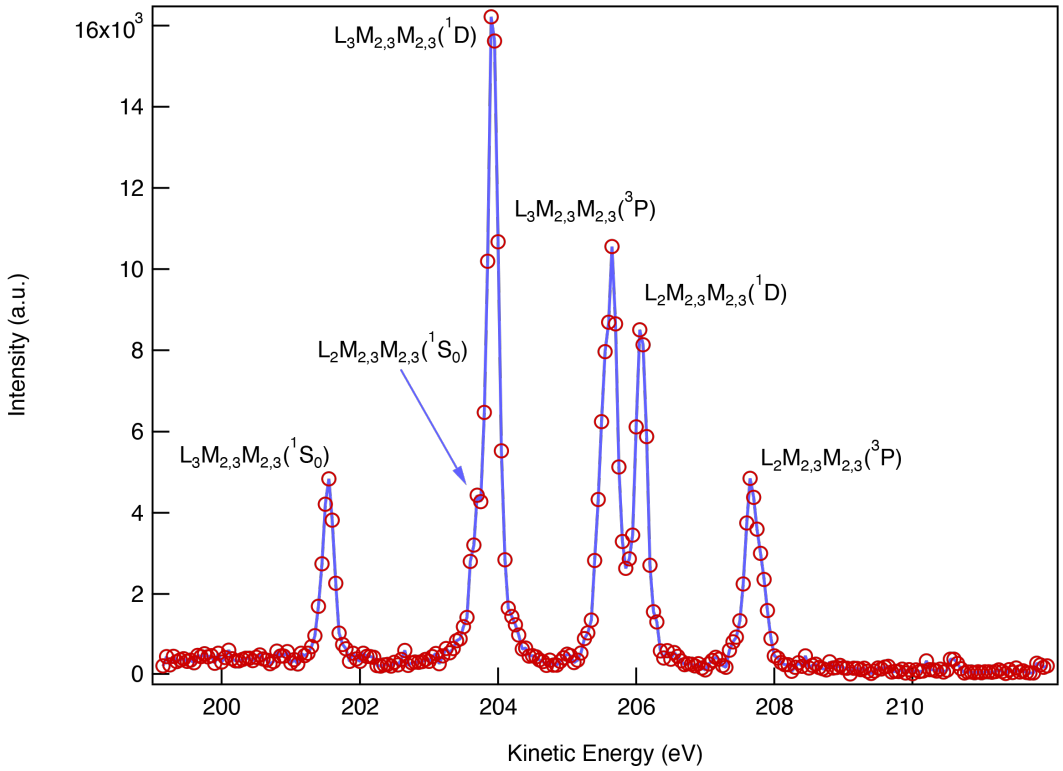

Figure 2.7: *The Argon $L_{2,3}M_{2,3}M_{2,3}$ Auger spectrum measured in the 2300 eV of photon energy. The red circles correspond to the experimental acquisition whereas the blue line is resulting of the curve fitting by a Voigt function. The peak corresponding to $L_3M_{2,3}M_{2,3}(^1S_0)$ was used to perform the kinetic energy calibration.*

The expected kinetic energy ($E_k^{expected}$) of the electron can be obtained by the sum of four parameters known in the literature: the electron binding energies (E_B) of L_2 or L_3; the ionization potential for Ar^+ and Ar^{2+}; the energy corresponding to the spectroscopic term (E($^{2S+1}L_J$)). Therefore, $E_k^{expected}$ is obtained by the Equation 2.3:

$$E_k^{expected} = E_{B(L_{2or3})} - IP_{Ar^+} - IP_{Ar^{+2}} - E(^{2S+1}L_J) \tag{2.3}$$

We used 248.63 (1) eV as the E_B to L_3 [101] and the IP values of 15.76 eV for Ar^+ and 27.63 eV for Ar^{2+} [102]. The energy related the ^1S term is 4.12 eV [102]. Then, applying these values to the Equation 2.3, we obtained the expected kinetic energy of the electron for the $L_3M_{2,3}M_{2,3}(^1S_0)$ state as $E_k^{expected} = 201.116(10)$ eV. From the measured spectrum (Figure 2.7), we chose the peak assigned to Ar $L_3M_{2,3}M_{2,3}(^1S_0)$ state due to its reasonable intensity and the simple curve fitting. The result of the fitting for the chosen peak gives 201.361 eV corresponding to the measured position in kinetic energy for the $L_3M_{2,3}M_{2,3}(^1S_0)$ state, which

we call $E_k^{measured}$. We can obtain the kinetic energy offset (ΔE) as the difference between the $E_k^{measured}$ and $E_k^{expected}$ kinetic energies, as shown in Equation 2.4. For example, for the spectrum presented in Figure 2.7 the calibration offset, ΔE, is 201.116 eV - 201.361 eV = −0.245 eV, meaning that the measured spectrum is +0.245 eV shifted in kinetic energy comparing to the expected lines.

$$\Delta E = E_k^{expected} - E_k^{measured} \tag{2.4}$$

The photon energy scale calibration is obtained by measuring Argon $2p$ photoelectron spectrum at the same photon energy as the data to be calibrated. By fitting Ar $2p_{3/2}$ and Ar $2p_{1/2}$ photoelectron lines with Voigt functions, we obtain the measured photoelectron kinetic energy ($E_{k,pe}^{measured}$). Then, one can obtain the experimental binding energy ($E_{B(L_{2,3})}^{measured}$) from Equation 2.5.

$$E_{B(L_{2,3})}^{measured} = h\nu^{measured} - (E_{k,pe}^{measured} + \Delta E) \tag{2.5}$$

The $E_{B(L_{2,3})}^{measured}$ binding energy is compared with the known reference value ($E_{B(L_{2,3})}^{reference}$)[101] of 248.63 (1) eV to Ar $2p_{3/2}$ and 250.79 (1) eV to Ar $2p_{1/2}$, giving the displacement in the photon energy scale. Therefore, we can obtain the real photon energy ($h\nu^{real}$) used in the measurement following the Equation 2.6.

$$E_{B(L_{2,3})}^{reference} - E_{B(L_{2,3})}^{measured} = h\nu^{real} - h\nu^{measured} \tag{2.6}$$

Total Resolution

One can determine the total resolution, which is related to the experimental and instrumental resolutions (Equation 2.7). The experimental resolution is associated with the Doppler effect contributions (thermal Doppler, $\phi_{t,D}$, and Doppler shift, $\phi_{D,s}$), while the instrumental resolution corresponds to the analyzer resolution ($\Delta\varepsilon$) and the photon bandwidth ($\phi_{h\nu}$).

$$\phi_{total}^2 = \Delta\varepsilon^2 + \phi_{h\nu}^2 + \phi_{t,D}^2 + \phi_{D,s}^2 \tag{2.7}$$

The thermal Doppler broadening ($\phi_{t,D}$) is related to the atom's thermal motion in the gas cell and can be obtained by the Equation (2.8). The variables E_k, T and $M_{a,nuc}$ correspond to the photoelectron kinetic energy (in electron volts), the absolute temperature (in Kelvin), and the molecular mass expressed in atomic mass units, respectively [103]. For example, considering the Argon 2p lines case, $E_k = 2050.5$ eV, $T = 300$ K, and $M_{a,nuc} = 39.948$ a.u.. Therefore, $\phi_{t,D} = 90$ meV.

$$\phi_{t,D} = 0.723\sqrt{\frac{E_k T}{M_{a,nuc}}} \tag{2.8}$$

The Doppler shift broadening ($\phi_{D,s}$) observed in the Auger spectra is related to the ion recoil as a result of the photoelectron emission. The formalism for calculating $\phi_{D,s}$ as a function of the angular distribution of the photoelectrons and the angle of emission of the electron relative to the axis of the analyzer is detailed in reference [67]. In our case, this angle is zero, and therefore we can describe $\phi_{D,s}$ as in the Equation 2.9.

$$\phi_{D,s} = m_e \cdot |\vec{v_{Auger}}||\vec{v_{nuc}}| = 2\frac{\sqrt{E_{k,Auger}E_{k,eff}}}{1836 M_{a,nuc}} \tag{2.9}$$

where $\vec{v_{Auger}}$ and $\vec{v_{nuc}}$ are the velocities of the Auger electron and the nucleus respectively and m_e is the mass of the electron. $E_{k,Auger}$ and $E_{k,eff}$ correspond to the kinetic energy of the Auger electron and the effective kinetic energy of the photoelectron with the relativistic corrections taken into account, respectively. The factor 1836 comes from the mass ratio of protons and neutrons to electrons and $M_{a,nuc}$ is the atomic mass number of the nucleus. Therefore, for the case of Argon LMM Auger spectrum presented in Figure 2.7 measured at 2300 eV photon energy, the Doppler shift, $\phi_{D,s}$, resulting from the emission of an Ar 2p photoelectron is 17.5 meV.

The spectrometer resolution value ($\Delta\varepsilon$) can be obtained by fitting the Ar LMM Auger lines using Voigt functions, which is a convolution of a Gaussian function and a Lorentzian function. The first function is related to the experimental and instrumental contributions and the second function is related to the lifetime of the state with a hole in the $L-$shell. Since the normal Auger lines are independent of the photon bandwidth, the total resolution of these Auger lines which is described by the Gaussian function, depends on the thermal Doppler broadening ($\phi_{D,t}$), the Doppler shift broadening ($\phi_{D,s}$) and the analyzer resolution, $\Delta\varepsilon$. Therefore, we can obtain $\Delta\varepsilon$ through the Equation (2.10). Here, $G_{\substack{Auger \\ resolution}}$ corresponds to the FWHM of the fitted Gaussian

function. Note that it is necessary to keep the spectrometer slits and pass energy fixed for all data acquisition during the experiment since the analyzer resolution depends on both of these parameters.

$$G^2_{\substack{Auger \\ resolution}} = \Delta\varepsilon^2 + \phi^2_{t,D} + \phi^2_{D,s} \tag{2.10}$$

In order to determine the photon bandwidth, Ar 2p photoelectron spectra are fitted with Voigt functions. The Lorentzian width is associated to the core-hole lifetime broadening, which is 0.118 eV for Ar 2p [104]. In our analysis, we kept the Lorentzian parameter fixed since we know the Ar 2p lifetime broadening. The Gaussian width corresponds to ϕ_{total}. Therefore, the Equation 2.7 provides the photon bandwidth ($\phi_{h\nu}$) value, once the other parameters were previously obtained.

Calibration measurements in Argon must be performed with care, beacause Argon Auger lines and the 2p photoelectron lines are intense so that the undulator requires to be detuned to avoid the detector's saturation. This saturation can lead to distortion of the peak shape resulting in an inaccurate estimate of the resolution.

Chapter

3 The Relativistic Nature of the Photoionization of the Spin-Orbit Doublets

Chapter content

Introduction

Photoionization is a physical process resulting from the system's response to the interaction with the ionizing electromagnetic radiation. The coupling between photon and the electrons of the target-system is weak so that the perturbation effects caused by the electromagnetic radiation over these electrons are small and assumed to be neglected. This assumption is important to investigate the target-systems' electronic properties through the photoionization process by applying spectroscopic techniques.

The increasing of the synchrotron radiation brilliance (third-generation synchrotron facilities) and the improvement of the electron detection system enabled measuring weak processes, i.e., processes of quite small cross-sections. These measurements can be done over an energy range from UV to X-ray regime. Specifically, in the harder X-ray regime (2 to 12 keV), the improvement of the experimental apparatus mentioned above was significant in the past five years, making it possible to perform experiments that were not possible to be carried out a few years ago [1, 63, 98].

The photoionization of subshells far above their thresholds in atoms and molecules is one of these small cross-section processes which can be experimentally studied thanks to the recent instrumentation improvements. Furthermore, the increase in resolution enabled measuring the ratio of the photoionization cross-section of the spin-orbit doublet components. Briefly, the spin-orbit coupling is a relativistic effect, where the spin angular momentum and the orbital angular momentum of the electron interact. This effect implies two non-degenerate states observed in the fine structure of the atomic spectra.

The possibility to measure the branching ratio of the spin-orbit components' photoionization cross-section far above their thresholds enabled us to investigate experimentally two long-term questions. The first question concerns the theoretical prediction that the branching ratio of the spin-orbit components' photoionization cross-section never approaches the statistical value (l+1)/l for a given subshell nl due to relativistic effects. [105–107] It was seen that the branching ratio is nonstatistical and energy-dependent in the near-threshold energy region. [108, 109] In this region, both the kinetic energy difference between the two spin-orbit components and the electron-electron correlation effects are significant. However, to the best of our knowledge, there are no experimental investigations concerning the high-energy branching ratios. The second

question comes from the spin-orbit cross-section's branching ratio in the vicinity of deeper photoionization thresholds, just below threshold, in the region of the infinite series of autoionization resonances, and just above threshold. In the latter case, previous works demonstrated relevant interchannel coupling effects. [110–112]

Owing to these open questions, we performed experimental and theoretical investigations on photoionization in a hard X-ray regime for Argon and Xenon atoms. It is important to remark that this work was performed in collaboration with Dr. Steven T. Manson's research group from Georgia State University in the United States, who performed the theoretical investigation in the present study, and with Dr. Ralph Püttner from Freie Berlin University, who performed the simulations on the partial cross-sections.

Three main results emerged from our findings. First, the experimental verification that the high-energy spin-orbit doublets' branching ratio does not approach the statistical value, which confirms the earlier predictions. Moreover, the experimental branching ratio deviates from the statistical ratio with increasing photon energy. Second, the resonances just below the photoionization threshold couple differently to each of the spin-orbit doublet components. This effect results in variations in the branching ratio in the order of a few eV. Third, the interchannel coupling can modify the intensity of the branching ratio in a wide energy range of about two keV.

3.1 Formalism

To understand the phenomena involved in this work, it is desirable to first discuss the formalism involved in the studied processes. We start by defining how the electron correlation term appears in the time independent Schrödinger Equation for multielectron atoms (3.1).

$$\hat{H}\Psi(R) = E\Psi(R) \tag{3.1}$$

Where $\hat{H}$ is the Hamiltonian operator, Ψ is the multielectron wavefunction, and R stands for the electronic spatial coordinates. The Equation 3.1 can be also written by using the Dirac

notation as in Equation 3.2.

$$\langle \Psi | \hat{H} | \Psi \rangle = E | \Psi \rangle \tag{3.2}$$

The Hamiltonian operator is a Hermitian operator whose eigenvalue is related to the system's total energy. The Hamiltonian (i.e., the electronic Hamiltonian, $\hat{H}_{el}$) terms for a multielectron system are shown in Equation 3.3. The operator $\hat{V}_{e,e}$ stands for the electrostatic repulsive interaction, $\hat{V}_{n,e}$ refers to the electrostatic attractive interaction between the atom's nucleus and electrons and $\hat{T}_e$ corresponds to the electrons' kinetic energy.

$$\hat{H}_{el} = \hat{V}_{e,e} + \hat{V}_{n,e} + \hat{T}_e \tag{3.3}$$

Such operators depend on the electrons coordinates (r_i and r_j), where i and j represent the electrons from the atom, and on the following constants: the electron mass, m_e, the electron charge, e, the vacuum permittivity, ϵ_0, and the reduced Planck constant, $\hbar$, as shown in Equation 3.4.

$$\hat{H} = \frac{1}{2} \sum_{i=1}^{N} \sum_{j>i}^{N} \frac{e^2}{4\pi\epsilon_0 |r_i - r_j|} - \sum_{i=1} \frac{Ze^2}{4\pi\epsilon_0 r_i} - \sum_{i=1}^{N} \frac{\hbar^2}{2m_e} \hat{\nabla}_i^2 \tag{3.4}$$

here, N is the number of electrons in the system, Z is the atomic number of the multielectron atom, and ∇ is the Laplace operator in spherical polar coordinates (the electrons are in a spherically symmetric potential). Meanwhile, the time independent Schrödinger Equation for a case of a multielectron atom cannot be analytically solved, i.e., there is no exact solution, due to the electron-correlation term generated from the electrostatic repulsive interaction operator, $\hat{V}_{e,e}$. In this way, quantum mechanic approximated methods are required to obtain its solutions. A well-known approximation is the Independent Particle Approximation, in which each electron is described by a single wave function named orbital. For example, the Hartree-Fock method defines the total multielectron wave function as a Slater determinant, which is an antisymmetric product of one-electron functions, and its total energy is calculated by the mean field of electronic interactions.

Although the Independent Particle model is an approximation that describes many quantum systems, this model cannot be applied in some circumstances. For cases where the relativistic

effects play a role, other approaches must be chosen. For example, the spin-orbit coupling is a relativistic phenomenon, so that it cannot be properly described through this approach. A model that describes well such phenomena is Dirac Equation since the relativistic effects are intrinsically included. Therefore, a suitable description of the spin-orbit coupling is possible.

Photoionization in X-ray regime far from inner-shell ionization threshold is accurately described by the Independent Particle Approximation theory. Therefore, such process is well-described in a single channel. [113] However, several theoretical and experimental works have shown the importance of electron correlation through interchannel coupling in both outer- and inner-shell photoionization of isolated atoms. [114, 115] An outstanding theoretical study showed the breaking down of the Independent Particle description for all atoms at the nl (where l>0) shells due to interchannel coupling with the neighbouring ns photoionization channels, although this description is valid for ns subshell photoionization. The relevance of the coupling between 2s and 2p channels in photoionization of Neon was evidenced by experimental measurements. [110]

In recent works, our research group demonstrated the effects of electron correlation by employing hard X-ray radiation to create double core-holes in atoms and molecules. In the Neon hypersatellite Auger spectrum, we demonstrated such electron correlation by the energy sharing between two photoelectrons leading to post-collision interaction [116]. In the study concerning the simultaneous core-excitation and core-ionization in CO_2 molecule, we observed the electron correlation effect through the competition between the direct and the conjugate shake-up processes. [117] In this way, these two studies presented an evidence that validity of the independent particle approximation needs to be considered carefully. Moreover, the interchannel coupling effect was also observed for chemical systems in condensed phase. A study of Ag and In solid-state samples showed a modulation of the 3d spin-orbit doublets' branching ratio near L_2- and L_3-edges. However, no clear indication of the coupling to the L_1 channel was observed. [111]

The photoionization process considering the interchannel coupling effects can also be formulated through the Independent Particle Model. To introduce this idea, we first consider a system in the ground state *i*. After a photoionization process, the system decays to a final state *f*. In this way, we can define a wave function that describes the ground state by ψ_i. Considering that there are two final channels, i.e., two energetically accessible final states, we define them by the wave functions $\psi_{1f,\varepsilon}$ and $\psi_{2f,\varepsilon}$ with ε being the total Hartree-Fock energy. The theoretical

description of the autoionization process includes the continuum states using the first order perturbation theory, by the term $\hat{H}_0$. [118] Therefore, the approximate final state wave functions, $\Psi_{1,E}$ and $\Psi_{2,E}$ are linear combinations of the exact final state wave functions, $\psi_{1f,\varepsilon}$ and $\psi_{2f,\varepsilon}$ as shown in Equations 3.5a and 3.5b.

$$\Psi_{1,E} = \psi_{1,E} + P\int \frac{\langle\psi_{2f,\varepsilon}|\hat{H}-\hat{H}_0|\psi_{1,E}\rangle}{E-\varepsilon}\psi_{2f,\varepsilon}d\varepsilon \tag{3.5a}$$

$$\Psi_{2,E} = \psi_{2,E} + P\int \frac{\langle\psi_{1f,\varepsilon}|\hat{H}-\hat{H}_0|\psi_{2,E}\rangle}{E-\varepsilon}\psi_{1f,\varepsilon}d\varepsilon \tag{3.5b}$$

where E is the total energy of the system when the continuum is included and P represents the principal value. Moreover, the transition process from the initial to the final state can be theoretically described through the transition matrix elements, where the transition process takes place under the action of a transition operator. Therefore, we can define the perturbed matrix elements by Equations 3.6a and 3.6b.

$$M_1(E) = D_1(E) + P\int \frac{\langle\psi_{2f,\varepsilon}|\hat{H}-\hat{H}_0|\psi_{1,E}\rangle}{E-\varepsilon}D_2(\varepsilon)d\varepsilon \tag{3.6a}$$

$$M_2(E) = D_2(E) + P\int \frac{\langle\psi_{1f,\varepsilon}|\hat{H}-\hat{H}_0|\psi_{2,E}\rangle}{E-\varepsilon}D_1(\varepsilon)d\varepsilon \tag{3.6b}$$

The terms $D_1(E)$ and $D_2(E)$ correspond to the exact transition matrix elements defined by the Equation 3.7, applying the dipole transition moment operator $\hat{T}$.

$$D_j(\varepsilon) = \langle\psi_i|\hat{T}|\psi_{j,\varepsilon}\rangle \tag{3.7}$$

The approximate final state wave functions (Equations 3.5) incorporate the concept of interchannel coupling, that is the modification of the transition matrix element of each channel since those wave functions involve a mixture of channels.

3.2 Calculation Details

Relativistic quantum-mechanics models guide the interpretation of the experimentally obtained photoionization branching ratios of spin-orbit doublets. Therefore, calculations were performed

through the Relativistic-Random-Phase Approximation (RRPA) [119, 120] together with Relativistic Multichannel Quantum Defect Theory (RMQDT) [121]. This *ab initio* method is based on the Dirac equation, which means that the relativistic effects are intrinsically included, as the spin-orbit interactions, for example. The RRPA calculations provided the cross-sections in the non-resonant continuum, and the RMQDT calculations concern the cross-section calculations in resonance regions. For Argon, all relativistic single-excitations were included, i.e., both discrete and continuum states for a total of 16 coupled channels. For Xenon, all relativistic single-excitations channels are also included, except the $1s$ channels for a total of 40 coupled channels. The omission of the $1s$ channels in this case is due to their binding energies, which are much higher than the considered energies, so that they have negligible influence.

Despite the partial cross-sections calculations for the non-resonant continuum agree qualitatively and quantitatively with the experiment, a different behavior was found for the resonant region. The RRPA/RMQDT calculations for inner-shells in the resonance region include the participator Auger channels, but the spectator Auger channels are omitted. Thus, while the RRPA/RMQDT methodology obtains the resonance positions quite well, the widths and the shape, $q-$parameters [118], will be quite unreliable owing to the omission. Therefore, the widths and shapes of the RRPA/RMQDT theoretical data must be augmented before those can sensibly be compared with experiment.

Close to thresholds, the cross-sections become more structured so that they need to be convoluted before taking the ratios, particularly for calculated Argon spin-orbit cross-sections. In this case, these cross-sections exhibit very narrow Fano line shapes slightly below the $1s$ ionization threshold. In this way, we convoluted the calculated spectra with a Lorentzian function using 655 meV as the full width at half maximum value (FWHM) related to the Ar $1s^{-1}$ core-hole lifetime. The cross-sections were also convoluted by a Gaussian function around 350 meV FWHM corresponding to the photon bandwidth. Although this procedure is also needed for Xenon calculations, the regions of $2s^{-1}np$ and $2p^{-1}ns, nd$ resonances close to threshold have several open channels, and the calculations become quite complicated. Therefore, because of the resulting energy gap, it is not possible to perform the convolution procedure. A more detailed explanation of the performed calculations and the simulations can be found in our paper related to the work described in this chapter [122].

3.3 Experimental Details

We performed Ar $2p^{-1}$ photoelectron spectra measurements between 3199 eV and 3207 eV near K-edge ionization threshold located at 3206.3(3) eV and at several photon energies between 2700 eV and 4000 eV. The photon bandwidth values were 0.25 eV at 2700 eV and 0.46 eV at 4000 eV. The Xe $3d^{-1}$, and Xe $4d^{-1}$ photoelectron spectra were measured between 5092 eV and 5118 eV of photon energy near the L_2 ionization threshold, which is located at 5018 eV. We also measured those photoelectron spectra between 4772 eV and 4800 eV photon energy near the L_3 ionization threshold located at 4787 eV. [123] The spectrometer resolution was 80 meV for Xe 4d and Ar 2p spectra acquisitions and 180 meV for Xe 3d measurements. These values are quite small when compared to the doublets spin-orbit splitting (approximately 2 eV for Ar $2p^{-1}$ and Xe $4d^{-1}$ and about 12 eV for Xe $3d^{-1}$). Therefore, they do not influence the experimental results. Photon bandwidth and spectrometer resolution values were obtained by the procedure detailed in subsection 2.2.4.

The pressure inside the gas cell was monitored and maintained during all acquisitions at $6 \cdot 10^{-6}$ mbar. The pressure in the spectrometer chamber is proportional to the pressure in the gas cell. We balanced the photon flux and the gas pressure to hold a low count rate, that is, below 1000 counts per sweep for a data acquisition time of 176 ms at each data point. Such adjustments were required to avoid the detector saturation effects, which causes systematic errors in the ratios between the integrated area of the photoelectron peaks (see 2.2.4). We performed the calibration on measured Argon photoelectron spectra in terms of the kinetic energy of the spectrometer and in terms of the photon energy following the procedure described in section 2.2.4. We calibrated Xenon spectra in terms of the photon energy scale on the absorption spectrum acquired before recording the photoelectron spectra [123]. The photon bandwidth value obtained following the procedure described in section 2.2.4 was approximately 0.5 eV.

It is important to point out that the integrated area of the photoelectron peak is proportional to the partial cross sections for measurements performed using an electron analyzer placed at the magic angle with respect to the polarization axis of the radiation [6]. However, the lens axis of the analyzer is placed parallel to the polarization of the incoming radiation at HAXPES end-station (see section 2.2.3), making it quite complex to perform experiments at magic angle. Considering such instrumental limitation, we performed our measurements at 0°, where the

effects of angular distributions play a role. Such angular distribution effects influence only to the extent that the angular distributions of the two components of a spin-orbit doublet differ.

Note that we cannot measure the experimental $nl_{l-1/2}$ and $nl_{l+1/2}$ partial cross sections with sufficiently high accuracy due to variations in the photon flux or gas pressure. Therefore, we compare the experimental and theoretical ratios $\sigma(nl_{l+1/2})/\sigma(nl_{l-1/2})$. In other words, our measurements were performed, not of cross sections, but of integrated peak areas, which are proportional to cross sections. Thus, the ratio of the integrated peak areas is equal to the ratio of cross sections.

The procedure performed to obtain the spin-orbit branching ratios from the studied photoelectron spectra requires the instrumental resolution (including the photon bandwidth and the spectrometer resolution) smaller than the spin-orbit splitting. Such consideration is needed to guarantee that the spin-orbit components do not overlap, stickling to obtain accurate ratio values. We obtained those spin-orbit branching ratios by the following procedure: first, we subtracted a linear background from the measured spectra; Second, from the spectra obtained after the background subtraction, we integrated the areas under the doublet peaks fixing the interval around each peak maximum; Third, the ratios of the respective integrated areas were plotted as a function of photon energy; Fourth, we obtained the error bars propagating the experimental statistical uncertainty. Small experimental error bars were required to measure the slight variations in the branching ratio provided by theory.

The interval chosen in the second step of our treatment for Ar $2p^{-1}$ and Xe $4d^{-1}$ photoelectron spectra was of 2 eV (i.e., an interval from 1 eV below the peak maximum to 1 eV above the maximum) and of 4 eV for Xe $3d^{-1}$ photoelectron spectra, with a range from 2 eV below to 2 eV above the peak maximum. Figure 3.1 shows the Ar $2p^{-1}$ photoelectron spectrum measured at a photon energy of 3201 eV. The depicted red boxes refer to the chosen fixed interval of 2 eV used to integrate the peak areas. We obtained the value of 1.930(3) for the ratio of the integrated peak areas for the spectrum shown. Specifically for the case of Argon measurements, the error bars were quite small. The required error bars were obtained performing $\cong$ 1670000 counts in the $2p_{3/2}$ peak and $\cong$ 865000 counts in the $2p_{1/2}$ peak. Considering the above mentioned conditions to prevent the detector saturation effects, those values were obtained by 80 sweeps with the total acquisition time around 3 hours for each data point.

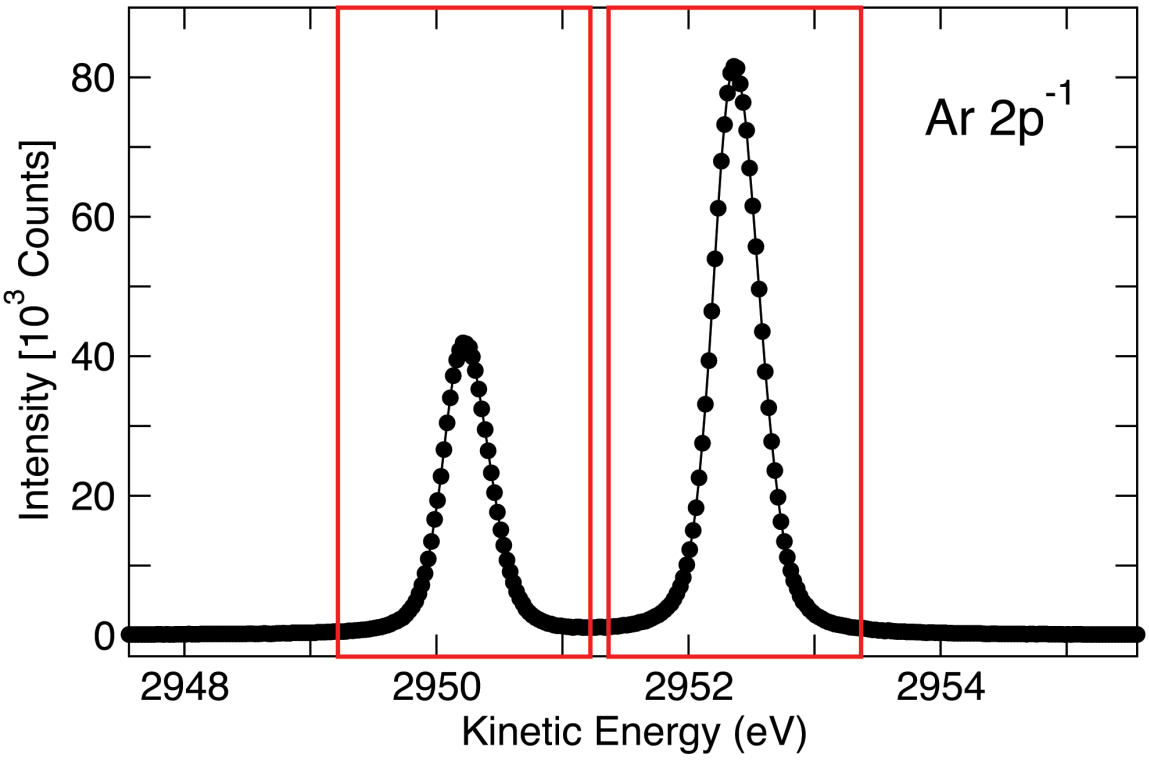

Figure 3.1: *Ar $2p^{-1}$ photoelectron spectrum measured at 3201 eV of photon energy. During this acquisition, the pass energy was kept at 100 eV and the curved slits widths are of 300 μm resulting in a detector resolution of 80 meV. In this photon energy the photon bandwidth value is $\cong$ 350 meV. The red boxes illustrate the fixed energy ranges used for integration in order to obtain the ratios between the integrated peak areas.*

3.4 Results and Discussion

3.4.1 Argon Results

Nonresonant Continuum

In Figure 3.2, we present the branching ratio obtained from Ar $2p_{3/2}$ over Ar $2p_{1/2}$ integrated areas as a function of the photon energy in the range from 2.7 keV to 4.0 keV. The black dots correspond to the branching ratio obtained from the measurements performed at 0°. Both hollow and solid blue dots correspond to the Ar 2p branching ratio data points corrected for the angular distribution ($\beta-$parameters) based on the theoretical results from reference [124]. We observed that such corrections are quite small. Moreover, the theoretical RRPA results are shown by the red curve. The structure observed at about 3.2 keV is due to the opening of the Ar 1s ionization channel.

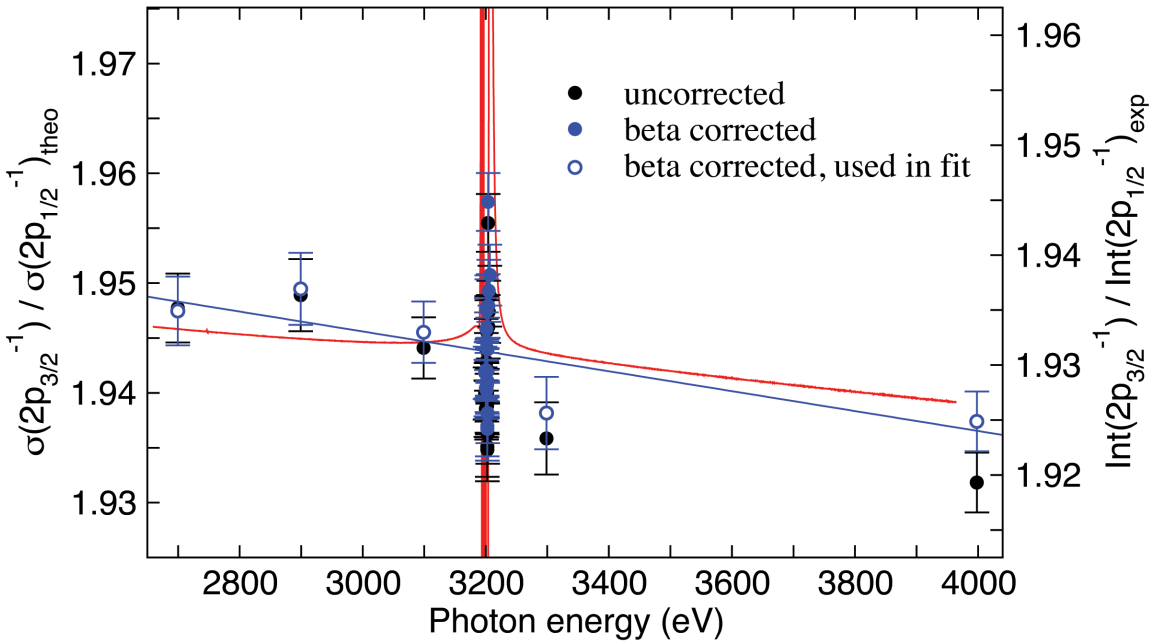

Figure 3.2: *Photoionization branching ratio for Ar 2p. The experimental data points measured at 0° are presented by the black dots. The experiment corrected by theoretical angular distribution parameters (β−parameters) is shown by the blue dots. The blue solid line is the result of a linear fit to the five off-resonance hollow blue dots. The calculated branching ratio is shown as the red curve. The theoretical data are shifted by 35.3 eV to lower photon energy to compare the theoretical and experimental Ar 1s ionization energies.*

The Ar $2p$ photoionization thresholds are about 250 eV whereas the photon energies studied are further than an order of magnitude above it. In this high-energy region, we observed the deviation of the branching ratio from the expected statistical value of 2 by increasing the photon energy. The off-resonance experimental data shown as the hollow blue dots were employed to perform a fit analysis by using a linear function. The result of the fit analysis is presented as the solid blue line. We observed both the experimental (blue line) and the calculated curve (red line) slopes diverging from the statistical value so that the calculations agree pretty well with experimental results. Note that the slope derived from the blue line is $9(3)\cdot10^{-6}\ eV^{-1}$ for the ratio, which is slightly larger than the slope value of $5.3\cdot10^{-6}\ eV^{-1}$ derived from the (theoretically obtained) red curve in the off-resonance region. Furthermore, in the higher off-resonance region above 3.2 keV, the calculated branching ratios are about 0.01 higher in comparison to the experiment. The observed branching ratio deviation from the statistical value at high energies suggests that the relativistic effects must play a role in this case.

It is important to point out that although the trends of the experimental and theoretical

branching ratios are the same, the absolute values are slightly different. There are several possible reasons for this small discrepancy. One possibility is the omission of ionization-plus-excitation (photoionization satellite) channels from the calculation. It is generally true that the interchannel coupling leads to changes for channels with small cross section coupling with degenerate (or nearly degenerate) channels with significantly larger cross sections. [110, 125–127] So, it is expected that the omission of the 1s satellite channels could have the small effect upon the branching ratio that is seen, thereby explaining a possible cause of the small quantitative difference between theory and experiment. In addition, the effect of quadrupole photoionization channels is omitted from the calculation. At photon energies in the 3 to 4 keV range, the quadrupole cross section could be of the order of 1% of the dipole. And, even though the lowest-order non-dipole effects vanish at 0°, if the quadrupole contributes to the spinorbit- split cross sections differently, this could have an effect upon the branching ratio.

The general phenomenology concerning the deviation from the statistical branching ratio value was predicted by earlier works [105–107]. The explanation for the branching ratio divergence from the statistical value involves the dipole matrix element being generated closer to the nucleus with the increase of the photon energy. This behavior can be physically thought of in terms of energy and momentum conservation of the photoionization process. The absorption of a high-energy photon involves a large momentum. Such quantity must be transferred to the remaining atom, which has its mass mostly concentrated at the nucleus. Thus, the photoabsorption probability is higher close to the atom's nucleus. In other words, considering r as the distance from the nucleus, the smaller the r value, the higher the absorption probability of high-energy photon.

Moreover, at large r values the wave functions that describe $2p_{3/2}$ and $2p_{1/2}$ are degenerate and depend on the orbital angular momentum l. Close to the nucleus, i.e., at small r values, those wave functions are not anymore degenerated and depend of the total angular momentum quantum number j. The degeneration breakdown of spin-orbit wave functions is obtained by the Dirac equation. [128] We calculated the probability density ratio between the Ar $2p_{1/2}$ and Ar $2p_{3/2}$ as a function of the nucleus distance for small r values as shown in Figure 3.3. The probability density ratio of $2p_{1/2}$:$2p_{3/2}$ becomes larger than the unity by decreasing r. This increase in the $2p_{1/2}$ wave function relative to the $2p_{3/2}$ wave function as r decreases explains the branching ratio deviation from non-relativistic value observed in Figure 3.2.

Furthermore, as the dipole matrix elements are generated closer to the nucleus where $2p_{1/2}$:$2p_{3/2}$ probability density is larger, such deviation becomes larger by the increase of the photon energy. Therefore, based on Dirac equation these ideas can be generalized as following: the probability density ratio $nl_{l-1/2}$:$nl_{l+1/2}$ increases with decreasing of r and diverges as $1/r^2$ as $r \to 0$ for all non-s subshell wave functions in both discrete and continuum. [128] In summary, the deviation from the non-relativistic value comes from differences in the radial dependence of both the wave functions and the dipole matrix elements of the two spin-orbit states.

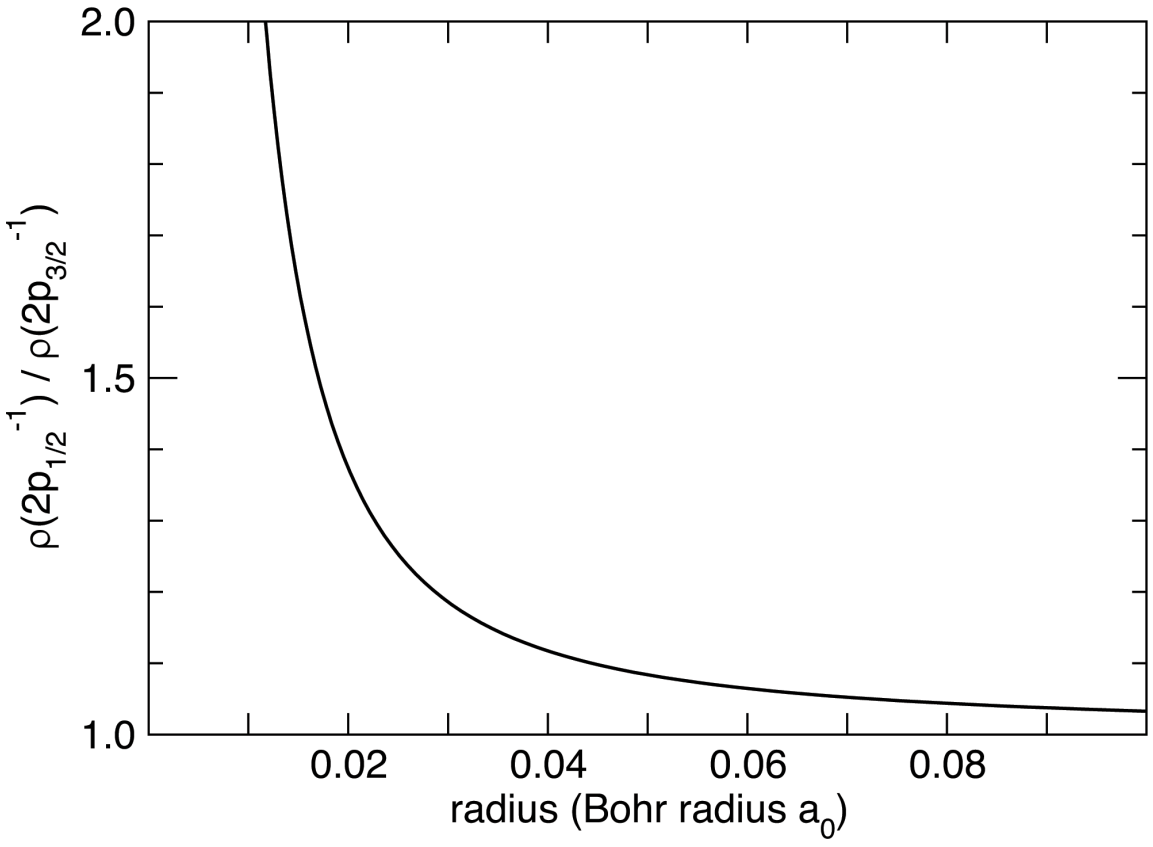

Figure 3.3: *Ratio of the calculated Ar 2p spin-orbit doublets probability density as a function of the radial coordinate.*

However, even though the trends of the experimental and theoretical branching ratios are in line, the absolute values are somewhat different. We observed from the results in Figure 3.2 that the experimental ratio deviates slightly more from statistical value than the theoretical ratio. There are two main possible reasons for this small discrepancy.

First, the omission of ionization-plus-excitation (satellite) channels from the calculation. The 1s cross section is calculated to be about two orders of magnitude larger than 2p cross section in the investigated energy range. The 1s ionization-plus-excitation channels are, in general, smaller by a factor of 10 compared to the main line. These contributions were calculated to be $\approx$ 15% for the case of Argon 1s ionization. [129] Then, the contributions from the 1s ionization-plus-excitation channels are expected to be an order of magnitude larger than the 2p cross sections. It is known by earlier works [110, 125–127] that the interchannel coupling causes changes in channels with small cross sections by the coupling with degenerate (or nearly degenerate) channels with larger cross sections. So, it is expected that the omission of the 1s satellite channels could affect the branching ratio, thereby being a potential cause for the slight quantitative difference between the theory and the experiment.

The second possibility is related to the effect of quadrupole photoionization channels, which were omitted from the calculation. The quadrupole cross section at photon energies from 3.0 to 4.0 keV range is expected to be of the order of 1% of the dipole. Despite the lowest order non dipole effects vanish at 0°, the quadrupole can affect the branching ratio if it contributes differently to each component of the spin-orbit splitting cross sections.

Branching Ratio in the Vicinity of the 1s Threshold

Figure 3.4 compares the Ar $2p_{3/2}$ and Ar $2p_{1/2}$ branching ratios in the vicinity of the 1s threshold (3206.3(3) eV). The branching ratios were obtained from the experimental data (red dots), from ab initio calculations (blue curve), and from the simulations (black curve). Starting with the simulation results, we shifted the branching ratios by 0.066 to lower values. This shift is required since the simulations do not include the general decreasing in the Ar $2p_{3/2}$:$2p_{1/2}$ (observed in Figure 3.2). Moreover, no energy corrections were performed in this case. An important result from the simulations is the dramatic increase in the branching ratio at 3203.6 eV, which corresponds to the position of the Ar$1s^{-1}4p$ resonance. Note that the experimental data present a similar behavior at this photon energy. In detail, the 16 data points lowest in energy, i.e.,

below 3203.6 eV, exhibit the 16 lowest branching ratios, while the 4 data points above this photon energy show the 4 highest ratios. The probability of the similarities between the experimental and the simulated data to be statistical is around 0.021%, which is a small probability.

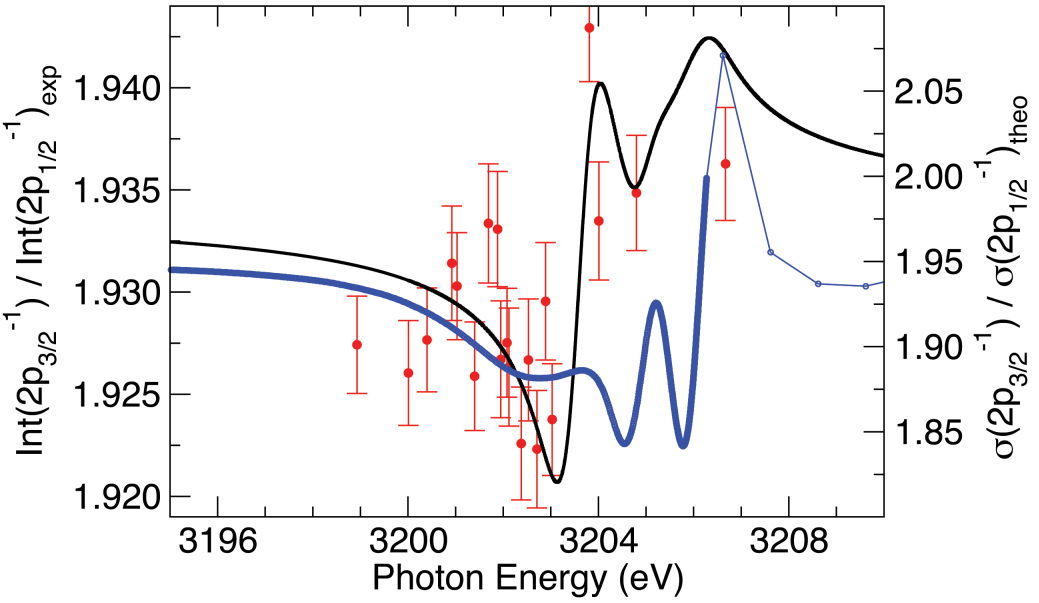

Figure 3.4: *Argon 2p photoionization branching ratio in the region of autoionizing resonances below the 1s threshold. The presented plots correspond to the experimental branching ratio (red), the simulated ratio for* $q(2p_{3/2}) = 2.5$ *and* $q(2p_{1/2}) = -2.5$ *with* $10\sigma(a) = \sigma(b)$ *(black), and the ratio of the convoluted ab-initio calculations (blue). The simulated branching ratio is shifted by 0.066 to lower values. The labels on the left axis apply for both experimental and simulated ratios whereas for the calculated ratio the labels on the right apply.*

Moving to the results from the *ab initio* calculations, we also observe the modulations of the branching ratio in the energy range of the Ar$1s^{-1}np$ resonances. However, the variation with energy is about an order of magnitude larger than the experimentally observed values. Note the scales for the experimental data (left axis) and for the *ab initio* calculations (right axis). Another important observation is that the calculated ratio variations do not follow the experimentally obtained results qualitatively. Even though, the *ab initio* calculations confirm that variation in the branching ratio is caused by the Ar$1s^{-1}np$ resonances.

It is mentioned in Section 3.2 that the spectator Auger decay channels are not included in our *ab initio* calculations. Indeed, the comparison between the experimental data points and the calculated results highlights that the spectator Auger decay channels contribute differently to the shapes of the Ar $2p_{3/2}$ and Ar $2p_{1/2}$ resonances. This effect is essentially relativistic, and it strongly affects the branching ratios in the resonances region and increases the widths of

the resonances. To overcome the calculation limitations, we performed simulations. Briefly, the partial cross sections defined in reference [130] were parametrized using the Fano formula for photoionization [118]. The result of the parametrization is given by the Equation 3.8:

$$\sigma_{(\epsilon)} = \sigma_{(a)} \cdot \frac{(q+\epsilon)^2}{1+\epsilon^2} + \sigma_{(b)} \tag{3.8}$$

where $\sigma_{(a)}$ and $\sigma_{(b)}$ are part of the continuum interacting or not interacting, respectively, with the Rydberg states. The q-parameter refers to the effective shape parameter and has no deeper physical meaning. Several simulations of the partial cross-sections were performed by varying the effective q- parameter. Following the convolution, the branching ratios were derived from these partial cross sections by combining different q- values and employing different $\sigma_{(b)}$ for the non-interacting background. The main result from the simulations is that the principle shape of the branching ratios depends mostly on the signs of the effective q-parameters compared to the exact values of q. More detailed and extensive explanations of the simulations performed in this work and the detailed plots for these several simulations are available in reference [122].

In the presented simulation results in Figure 3.4 (black curve), the combination for the effective q-parameters were 2.5 to Ar $2p_{3/2}$ and -2.5 to Ar $2p_{1/2}$ partial cross-sections. Moreover, both partial cross-sections were assumed as $10\sigma_a = \sigma_b$. This result agrees with the experimentally observed variations in the branching ratio owing to the $1s \rightarrow np$ resonances. We observed a significant variation of the experimentally obtained branching ratio over an energy range of less than 10 eV, a small range. This observation highlights the considerable differences between the resonance structures of the $2p_{3/2}$ and $2p_{1/2}$ ionization channels.

The positions and the widths of $1s \rightarrow np$ resonances are intrinsic properties of them, and they are independent of an outgoing channel. However, the shapes of these resonances are channel-dependent. We know from the simulations that the effective q-parameters are related to the shape of the resonances. Thus, comparing the experimental results to the simulation results, it is evident that the effective q-parameters are different for the two $2p_{3/2}$ and $2p_{1/2}$ ionization channels. An earlier work on the analysis of the branching ratios in the vicinity of a resonance showed similar results for the q-parameters. [130] Furthermore, the simulations suggest that the effective q-parameter is positive for the $2p_{3/2}$ partial cross-section and negative for the $2p_{1/2}$ partial cross-section. A previous work reported a mirroring behavior of resonances similar to

our findings concerning the differences in the resonance shapes in different partial cross-sections. [131]

Despite the good results concerning the effective q-parameter, it was not possible to obtain the exact values since the differences from the simulations are smaller than the experimental error bars. Even so, we could observe this purely relativistic effect: the $1s^{-1}np$ resonances couple differently to the $2p_{3/2}$ and $2p_{1/2}$ continua. There are two main reasons that explain this behavior as presented in the following.

First, the radial dependence of the autoionizing matrix element ($\langle 1s^{-1}np|1/r|2p_j^{-1}\epsilon l\rangle$), with both direct and exchange terms, can differ for $2p_{3/2}$ and $2p_{1/2}$ continua, especially quite close to the nucleus. The second reason concerns the angular momentum and parity selection rules. For the decay of the $1s \rightarrow np$ resonances to the $2p_{3/2}$ hole, $\epsilon s_{1/2}$, $\epsilon d_{3/2}$ and $\epsilon d_{5/2}$ are allowed. However, for the decay to the $2p_{1/2}$ hole, only $\epsilon d_{3/2}$ and $\epsilon s_{1/2}$ are allowed. Such differences for the allowed decays are still apparent even after the theoretical data's convolution to the experimental resolution, indicating the importance of the selection rules in this case. Finally, a third effect that affects the branching ratio is the interchannel coupling. However, in this case, this effect is quite small, increasing the branching ratio by less than 0.003 in the photon energy range of 3000 to 3150 eV. In the next group of results on Xenon, we will see that this small influence of interchannel coupling on the branching ratio seems to be characteristic for the cases where a s-shell is involved.

3.4.2 Xenon Results

We observe experimentally for the Xenon 3d and 4d branching ratios being affected by the resonances below the $2p_{3/2}$ and $2p_{1/2}$ thresholds over a range of a few eV. Moreover, these branching ratios are strongly influenced by interchannel coupling over a wide energy range of about three keV. In detail, the wavefunctions' relativistic behavior affects the branching ratio, causing an increasing divergence from the statistical value with increasing photon energy. However, this increasing divergence is presented by the calculations only due to the complications caused by the strong interchannel coupling for the Xenon case. [122]

We present in Figure 3.5, the experimental data points on Xe $3d$ and Xe $4d$ branching ratios in the vicinity of $2p_{3/2}$ and $2p_{1/2}$ ionization thresholds (red dots). The branching ratios derived from

the calculations are shown as black dots. Besides, the theoretically obtained branching ratios in the vicinity of the 2s threshold are also presented. Starting by comparing the experimental data and the results derived from the calculations in the vicinity of $2p_{3/2}$ and $2p_{1/2}$ thresholds, we observe that the calculated branching ratios follow the trend observed in the experimentally obtained results so that the theory agrees well with the experiment. Note that we did not adjust the calculated results for the experimental conditions since the resonances close to the threshold were not calculated.

Following, in the region below each threshold, we observe the beginning of the lowest-energy resonance in the calculated results. However, these resonances are inconspicuous in the experimental results due to the averaging implicit in the measurements. In detail, the cause for the averaging is the Xe 2p lifetimes that result in an energy width around 3 eV and the photon bandwidth around 0.5 eV. Moreover, we notice a rise at $2p_{3/2}$ threshold and a dip at $2p_{1/2}$ threshold in the experimental results. A similar trend is well-reproduced by the results from the calculations. This behavior evidences the different shapes of the resonances in the two cases.

Moreover, we observed that the $3d$ and $4d$ branching ratios in the vicinity of the $n = 2$ thresholds are quite similar in absolute values and variation with energy in both calculated and experimental results. The reason for such similarities follows the discussion on the Argon case. Essentially, the matrix elements for photoionization for both $3d$ and $4d$ are generated at a substantially small distance from the nuclei (i.e., a quite small r). In the case of a quite small r, the doublets wave function's ratio is independent of the orbital angular momentum, although the form of the wave functions that describe $3d$ and $4d$ depends on the orbital angular momentum.[128] It is known that the normalization factors of the $3d$ and $4d$ wave functions are different, but even these factors are canceled out since we are considering the branching ratios. Consequently, both $3d$ and $4d$ yield the same branching ratios at high-energy, as observed.

An important observation is the increasing of the branching ratio deviation from the non-relativistic value of 1.5 when increasing the photon energy. We observed that both $3d$ and $4d$ branching ratios in the vicinity of $2p_{3/2}$ threshold are about 1.4 whereas in the vicinity of $2p_{1/2}$ the branching ratios are about 1.3. Note that the energy is higher for the branching ratios in the vicinity of $2p_{1/2}$ threshold. Such observations agree with the trend seen in Argon, where the branching ratios move further away from the statistical ratio by increasing the photon energy. However, the $3d$ and $4d$ branching ratios in the vicinity of $2s$ threshold are close to 1.37 in

contradiction to this trend since the energy here is higher, but the deviation from the statistical value is lower than for $2p_{1/2}$ case.

More calculations were performed to understand the reason for the larger branching ratios of both Xe $3d$ and $4d$ near $2s$ threshold than those in the vicinity of $2p_{1/2}$ threshold. Such calculations covered a broad energy range of about 2.7 keV as shown in Figure 3.6. In order to further elucidate this behavior, we considered both cases with and without coupling with the n = 2 subshells. The calculations without considering coupling (blue curve) show the branching ratio smoothly decreasing due to the discrete wave functions' relativistic behavior near the nucleus. The behavior is entirely different when the coupling with n = 2 photoionization channels is considered (red curve). There are sharp drops in the ratios between $2p_{3/2}$ and $2p_{1/2}$ thresholds followed by a progressive increase above $2p_{1/2}$ and $2s$ thresholds. Such behavior seen in the red curve is caused by interchannel coupling, which explains the larger nd branching ratios near 2s threshold than those in the vicinity of $2p_{1/2}$.

Furthermore, the coupling effects of the $2s$ channel are much smaller than the $2p$ channels' effects on nd branching ratios. A hypothesis for this behavior involves the dependence of the interchannel coupling matrix elements on the angular momentum. There is a clear difference in the interchannel coupling of outer-shells with nl inner-shells: the coupling with ns channels is considerably weaker than the coupling with the np channels. However, further studies are necessary to obtain a categorical answer to this behavior. An important conclusion is that the interchannel coupling influences the branching ratios over a wide energy range. Moreover, the importance of interchannel coupling over a broad range from below to above inner-shell thresholds is clearly seen.

3.5 Conclusion

The branching ratios of the photoionization cross-sections of the spin-orbit doublets of Argon and Xenon were experimentally and theoretically investigated for energies well above their thresholds. Such detailed experimental investigations on these weak processes were possible since we have access to the state-of-the-art experimental resolution in the hard X-ray regime at GALAXIES beamline.

As predicted by earlier theoretical works [105–107], we found the spin-orbit branching ratios diverging from the nonrelativistic (statistical) value as the photon energy increases, rather than approaching the statistical value, in high energies. Such behavior of the photoionization branching ratios can be explained by the differences in the shape of each spin-orbit component's wave functions close to the nucleus (at small r). In detail, $j = l - 1/2$ wave function dominates well close to the nucleus, where r is quite small. This region becomes more important to the determination of the photoionization matrix elements as energy increases. We investigated how the branching ratio of the spin-orbit components is affected in regions close to the nucleus for Xenon $3d$ and $4d$ and for Argon $2p$. However, our findings can be generalized to the branching ratio of all doublets of all atoms since the Dirac equation shows a dominance of the $j = l - 1/2$ wave function compared to $j = l + 1/2$ close to the nucleus. Moreover, this explanation can be applied to molecules due to the atomic-like form of the molecular wave-functions near the nuclei. Therefore, this phenomenon can be entirely generalized.

We investigated the interchannel coupling affecting the branching ratios in the vicinity of inner-shell thresholds. Despite previous observations [111], we revealed new aspects of this phenomenology. We showed that for Xe $3d$ and Xe $4d$, the interchannel coupling around the $n = 2$ thresholds affects the branching ratio in a broad range of energies (around 3 keV) above and below the thresholds and not only at energies close to the thresholds. Accordingly, the inner-shells influence upon the branching ratios is not a localized effect on the thresholds' energies. Moreover, a strong dependence of the relativistic interchannel coupling matrix elements upon energy is shown by the rapid Xe branching ratios' variations with energy. This behavior is more pronounced between the $2p_{3/2}$ and $2p_{1/2}$ thresholds.

Furthermore, the resonances below deeper ionization thresholds and the components of the spin-orbit doublets couple differently. The measured Ar $2p$ ionization branching ratio in the

resonance region slightly below the $1s$ threshold shows a strong modulation in a small photon energy range due to a different coupling between each spin-orbit components and the resonances. The same behavior was observed for the Xe $3d$ and $4d$ branching ratios in the resonance region below the $2p$ thresholds. Therefore, further investigations on the branching ratios in inner-shell resonance regions are needed to elucidate the physics behind the processes occurring in this case.

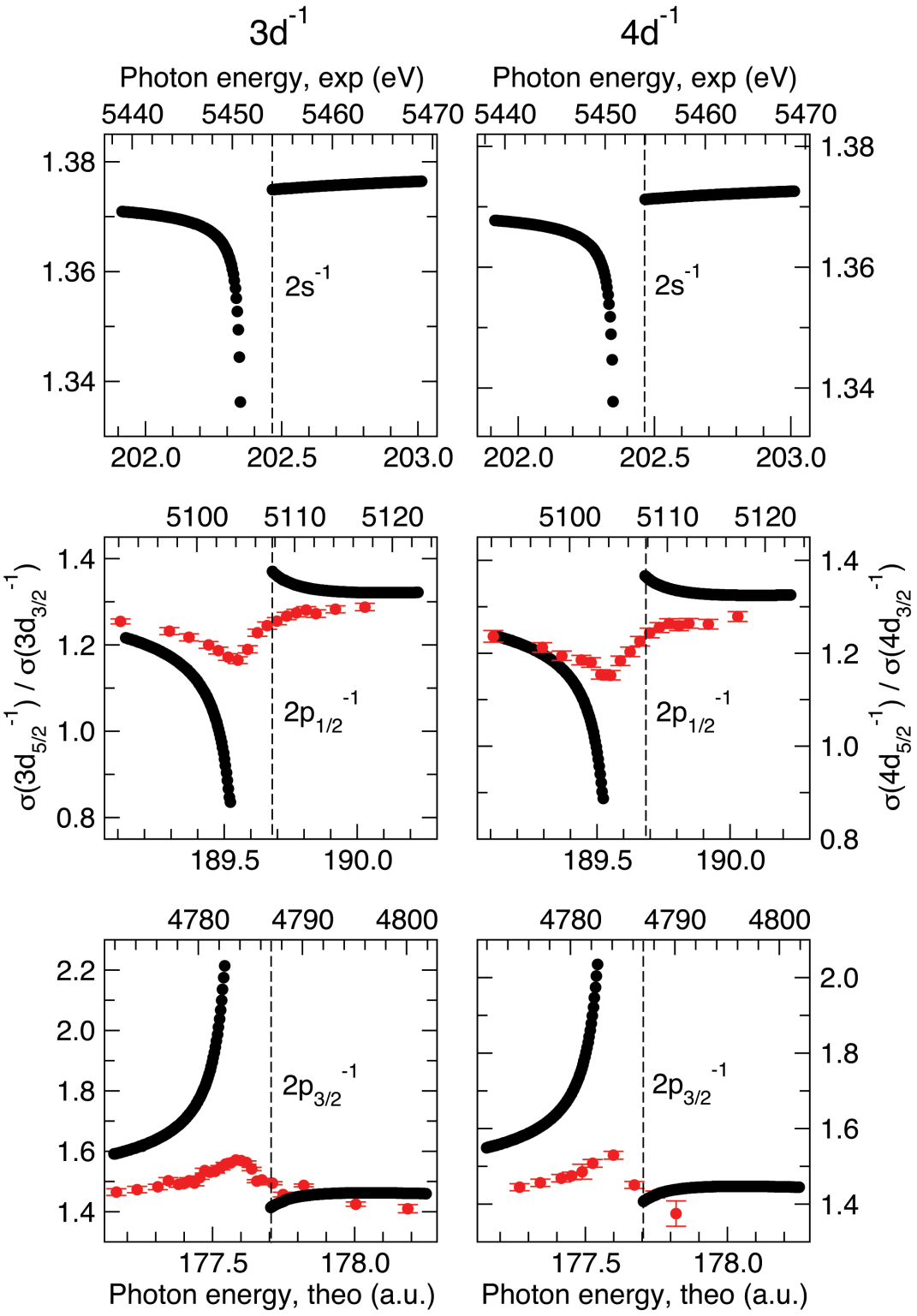

Figure 3.5: *Xe 3d and Xe 4d photoionization branching ratio in the vicinity of the L-thresholds. The experimental points are presented in red whereas the black points correspond to the theoretical results. The tailing (up or down) behavior in the calculated results is related to the beginning of the first resonance of each Rydberg series, which is averaged over in the experiment. The experimental and theoretical energy scales were shifted relative to each other to match the dashed lines, which correspond to the ionization energies.*

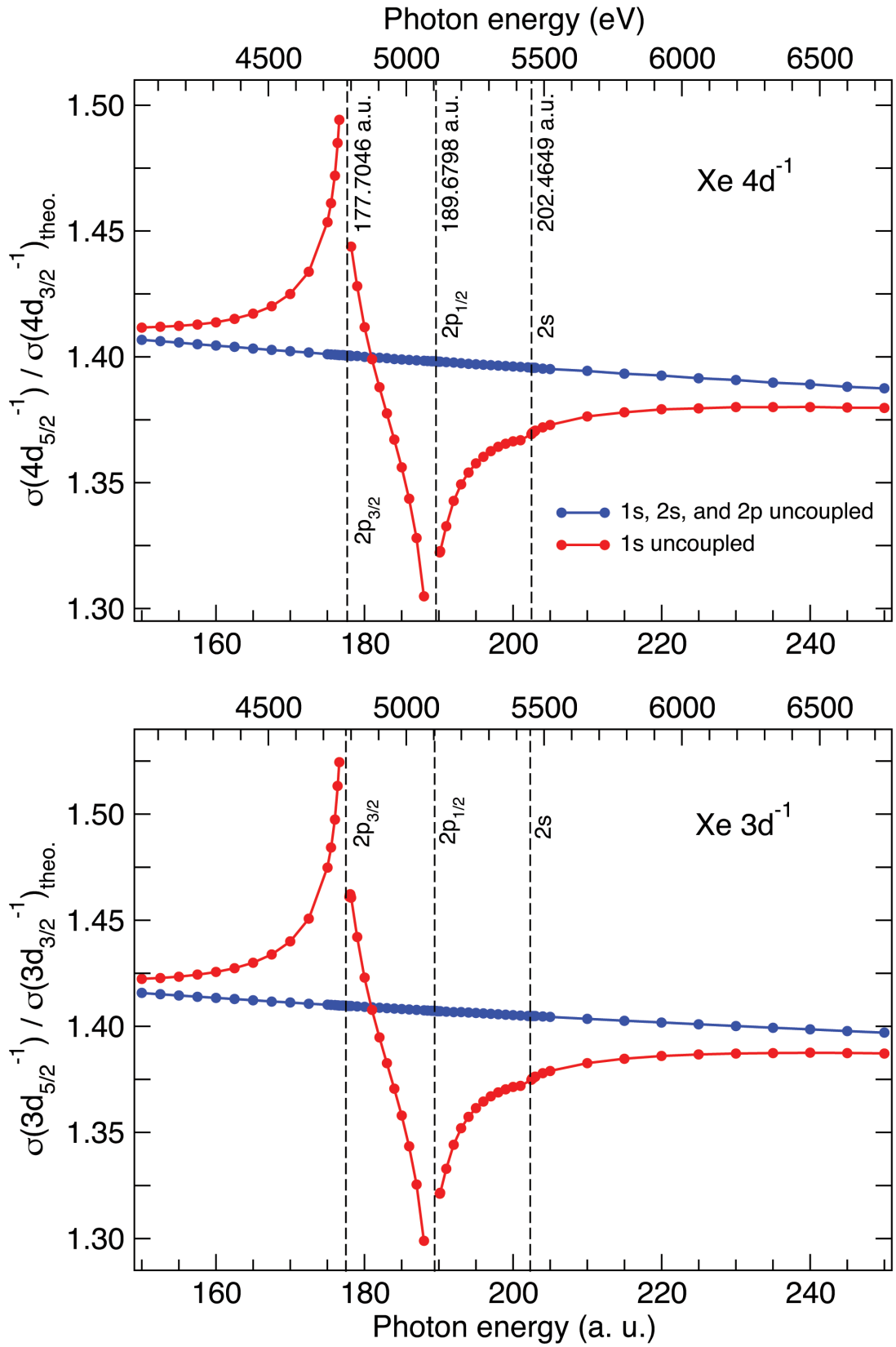

Figure 3.6: *Calculated Xe 3d and Xe 4d photoionization branching ratios. In the red points, the coupling with n = 2 channels were considered. In the blue points there is no coupling with n = 2 channels. In order to well reproduce the Xe 2s and Xe 2p ionization energies, the values in eV were obtained by multiplying the theoretical energy values by 0.99 Hartree (a.u.).*

Chapter

4 Resonant Auger Spectroscopy as a Probe of Conjugation Effects

Chapter content

Introduction

Thiophene (C_4H_4S) and thiazole (C_3H_3NS) are two sulfur-based heterocyclic aromatic molecules with several industrial applications. The growing attention to these molecules is due to their role as building blocks for promising organic materials used as solar cells, chemical sensors, photovoltaic devices, among other applications. [132–137] However, a large part of the studies on photo-induced processes in these molecules address the valence bands of the organic systems using visible light. Only a few studies were performed addressing the core levels of these aromatic molecules. An earlier study investigated the non-resonant and resonant Auger electron spectra in condensed layers of five-membered heterocyclic aromatic molecules using soft X-rays. [138] The investigation showed that different mechanisms for decay could be distinguished, depending on which atom was initially excited, Carbon or Nitrogen at the $K-$edge. A work performed

in hard X-ray regime investigated the selective bond breaking in condensed thiophene through photon stimulated ion desorption spectroscopy combined with resonant Auger spectroscopy. In this case, the resonant Auger decay measurements addressed the thiophene molecule at the Sulfur K-edge. Here, the importance of the antibonding character of the spectator electron to induce selective bond breaking was explored to obtain information on the fragmentation mechanism in thiophene. [139] These results were compared to a similar analysis for condensed thiolane (C_4H_8S), the saturated analog of thiophene, showing that the differences in the S^+ fragment yields are related to the spectator Auger decay process in both cases. [140] Despite these previous studies, investigations on deep core level for thiophene and thiazole molecules in the gas phase, where their electronic structure is not affected by a substrate, are still scarce.

An important electronic effect in thiophene and thiazole molecules is the conjugation effect. The stabilizing interactions between electronic orbitals in molecules, which can be summarized as "conjugation effects", were historically classified as ($\pi-$) conjugation, hyperconjugation, and σ conjugation, describing the consequences of electronic delocalization. Briefly, these divisions were based on which orbital types are involved in such interactions. In this way, the $\pi-$ conjugation refers to either $\pi-\pi$ bonds or between $\pi-$bonds and $p-$orbitals. Hyperconjugation is defined as the interaction between $\sigma-$ and $\pi-$ orbitals, whereas σ conjugation relates to the interaction between $\sigma-$orbitals. However, the distinction between these conjugation effects is purely didactic since it describes the same fundamental phenomenon, being different only according to the $\pi, \sigma-$model. The conjugation effect was ordinarily defined in the textbooks as the difference between a system represented by an ideally localized Lewis structure and a real molecule. In this case, the electronic delocalization is thought of as a two-center bonding interaction, acting as a correction factor once the Lewis model was conceived to be applied in localized systems. In this context, it is essential to emphasize that the classical understanding of a covalent chemical bond takes place between two-center/two-electron bonds. Therefore, the delocalization is treated as a deviation degree from the "pure" Lewis structure. It is crucial to point out that the description in terms of Lewis structure is incomplete because the molecular arrangement is described as a delocalized quantum system, and the delocalization concept in the description of chemical systems comes from the Molecular Orbital (MO) theory. From the MO theory, in conjugated systems, the overlapping of neighboring $p-$ character orbitals into a larger $\pi-$system results in electron delocalization over the molecule. In hyperconjugation, the interaction is characterized as between electronic orbitals, where one of these orbitals corresponds to

a $\sigma-$bond. Consequently, the highest energy orbital must be empty (or partially empty), thus acting as an acceptor while the lower energy orbital acts as a donor, i.e., it must be at least partially filled. [141, 142]

In this work, we applied resonant Auger spectroscopy to probe conjugation effects using thiophene and thiazole molecules in gas phase. We measured the spectator resonant $KL_{2,3}L_{2,3}$ Auger electron spectra for thiophene, thiazole, and thiolane molecules at the Sulfur $K-$edge and presented them as 2D maps, with the kinetic energy of the Auger electron as a function of the photon energy. The maps were recorded at different photon energies tuned with small steps from below the S 1s $\rightarrow$ LUMO resonance to beyond the ionization threshold. In the aromatic molecules, we observed an inversion in the order of the two lowest core-excited states between the intermediate and final states. This effect is absent in thiolane, saturated molecule. High-level quantum-mechanical calculations qualitatively reproduced the behavior observed in the experimental results. The interpretation of our observations in terms of the conjugation effect was given by the Natural Bond Orbitals method by evaluating the stabilization energy for the aromatic systems. The calculations were carried out in collaboration with Dr. Carlos E. V. de Moura, postdoc researcher in the group of Prof. Dr. Mario Barbatti at Aix-Marseille Université in Marseille, France.

4.1 Calculations Details

In order to estimate the transition energies of the core excited states, we applied the specific Inner-Shell Complete Active Space Self-Consistent Field (IS-CASSCF) procedure.[143] In this method, the molecular orbitals set of the active space is split in two groups: one group containing the inner-shell orbitals to be evaluated, and another group containing the remaining valence orbitals, usually obtained from a previous CASSCF calculation for the electronic ground state. Each of these groups has a particular electronic occupation assigned, according to the aimed state, and is optimized in particular SCF steps, avoiding the variational collapse for the convergence of highly excited states. The procedure is adjustable and can also be generalized to any construction of active spaces. [144] One advantage of the CASSCF wave function is its flexibility: using this procedure we can obtain the individual vertical absorption transitions, the shape of the molecular orbitals and estimate the kinetic energies of the Auger electron. [145]

Besides, we have performed the Natural Bond Orbitals (NBO) analysis, which provides information on chemical bonds and electron lone pairs from electronic densities. [146, 147] The method builds an orthonormal set of NBO orbitals, in which the electronic occupancy is maximal. Using NBO, we recover the Lewis-like description of the chemical structure. The NBO analysis was previously usefully applied in the assignment of core-excited states.[148, 149]

The stabilization of the chemical structure by the electronic delocalization plays an essential role for the excited states investigated by the Resonant Auger spectroscopy. Through the NBO formulation, the quantum-mechanical delocalization is described by the deviation when comparing the obtained NBO set with an ideal Lewis structure, in which each Lewis-type NBO orbital occupancy q is exact (2.0 for filled orbitals and 1.0 for open-shell orbitals). To quantify these effects, we applied the second-order perturbation analysis of the Fock matrix,[150–152] which enables the detailed evaluation of the stabilization energy $\Delta E_{ij}^{(2)}$ by the electronic delocalization between an occupied NBO(i) and a non-occupied NBO(j), characterized as donor and acceptor orbitals, respectively. Then, the delocalization can be rationalized by the electron transfer between a pair of NBOs, and the stabilization energies are calculated through:

$$\Delta E_{ij}^{(2)} = q_i \frac{F_{ij}^2}{|\epsilon_i - \epsilon_j|} \tag{4.1}$$

where q_i is the donor orbital occupancy, F_{ij} is the off-diagonal NBO Fock matrix element, and ϵ_i (resp. ϵ_j) is the donor (acceptor) orbital energy.

Two types of Lewis-type NBO interactions are relevant for the investigated heterocyclic molecules: the conjugation effect, which is related to the delocalization over π orbitals and n lone pairs, and the hyperconjugation effect, which is related to σ orbitals and n lone pairs.[153–155]

In order to estimate the transition energies of the core excited states, we applied the specific Inner-Shell Complete Active Space Self-Consistent Field (IS-CASSCF) procedure. For the ground state of the thiophene and thiazole molecules, we applied a wave function CASSCF(12,10), including the bonding and antibonding pairs of orbitals related to the σ_{SC} and π bonds, and two orbitals related to Sulfur lone pairs, totaling ten orbitals. An equivalent selection was made for the thiolane molecule, using a wave function CASSCF(8,6), and including the bonding and antibonding pairs related to the σ_{SC} and also two orbitals related to Sulfur lone pairs.

When calculating the core excited states using the IS-CASSCF method, we include in the active space their related core orbital. For the Sulfur K-shell excitations, the orbital equivalent to S 1s is included, and its occupation is constrained to one electron, moving the excited electron to the valence active space. For the final states, resulting from Sulfur Auger KLL decay spectator, the three S 2p orbitals are included, and their occupation is constrained to four electrons so that one electron is moved to the valence active space and another one, related to the Auger ionization, is removed from the system. In the last case, we also include a state-average between three states (SA3-IS-CASSCF), to describe all the 2p double-hole possibilities appropriately.

Electronic transition energies were obtained by ΔCASSCF calculations, by the difference between ground and excited states energies. Oscillator strengths for S 1s excitations were obtained using the molecular orbitals of the excited state as the basis for the electronic configurations. To be able to compare our calculated transitions to the experimental partial electron yield results, the theoretical sticks spectrum was broadened with Voigt functions. The Lorentzian part represents the lifetime broadening, 0.52 eV full-width at half-maximum (FWHM), The Gaussian part accounts for the photon bandwidth (0.2 eV FWHM) and the eventual dynamics broadening, which varies for different states. Equilibrium geometries were obtained by the geometry optimization procedure at second order MøllerPlesset perturbation theory (MP2) level. Thiolane has two enantiomers: envelope (C_S) and twisted (C_2), so both geometries were included in the inner-shell calculations. Relativistic scalar effects were recovered by 4^{th} Douglas-Kroll-Hess method (DKH). [156–158] We applied the core-extended Dunning's correlated consistent polarized basis set, aug-cc-pCVTZ-DK. [159–164] A similar approach was previously applied to Sulfur core states providing nice agreement with experiments. [165] All calculations were done using MOLPRO 2012 package. [166, 167]

Furthermore, we performed the Natural Bond Orbitals analysis by the Second Order Perturbation Analysis of the Fock Matrix. The threshold for considering the NBO interactions was set to 1.0 meV. The analysis requires a single electronic configuration wave function, using the Restricted Open-Shell Hartree-Fock (ROHF) method, in order to describe the core ionized states related to $1s^{-1}$ and $2p^{-2}$ cations. For comparison, calculations for the core excited states were also performed at the same level of theory. These wave functions were obtained by constraining the occupation of the desired inner-shell molecular orbitals, in a procedure similar to the IS-CASSCF. Correspondingly, these core states calculations at the ROHF level labelled as

IS-ROHF.

4.2 Experimental Details

We measured the resonant Auger S $KL_{2,3}L_{2,3}$ spectra for thiophene, thiolane, and thiazole molecules in gas phase. The spectra presented as two-dimensional maps were obtained by changing the incident photon energy between 2470 eV and 2480 eV in steps of 0.1 eV (0.2 eV for thiazole). The X-ray absorption-like partial electron yield (PEY) spectra for Sulfur K-edge were obtained by integrating the intensity signal along the kinetic energy axis of the 2D maps.

The pass energy of 200 eV and the 400 μm slit width of the analyzer, fixed during the measurements, provided a spectrometer resolution of 178 meV. The photon bandwidth was approximately 0.25 eV at 2473 eV photon energy, resulting in a total resolution of 0.31 eV. The related electron kinetic energy windows were 2090 eV to 2125 eV for thiophene and thiolane and, 2090 eV to 2120 eV for thiazole. The pressure inside the chamber was kept at 1.2 e-5 mbar for thiophene, 1.7 e-5 mbar for thiolane, and 4.5 e-5 mbar for thiazole measurements. We calibrated the kinetic energy scale through the known Argon KLL Auger lines measured with the same experimental parameters. The photon energy was calibrated using the known Ar $2p_{1/2}$ binding energy of 250.79 eV for the measured Argon $2p^{-1}$ photoline.[101]

4.3 Results and Discussion

The experimental partial electron yield (PEY) and calculated absorption spectra near Sulfur K-edge for thiolane, thiophene and thiazole molecules are presented in Figure 4.1.The calculated spectra were shifted by -3.2 eV for thiazole and -2.7 eV for thiophene and thiolane, respectively, to compare with the experimental spectra. The PEY spectra are obtaining by summing the measured S KLL Auger spectra over kinetic energies.

We start the discussion with the thiolane molecule (Figure 4.1a). The experimental spectrum shows an intense peak at the photon energy of 2472.6 eV and a shoulder at $\approx$ 2473.5 eV. Similar observations were made in an earlier experimental work [168] showing the transition energies of 2472.3 eV and 2473.1 eV for S 1s absorption spectrum in thiolane, in good agreement with our measurements.

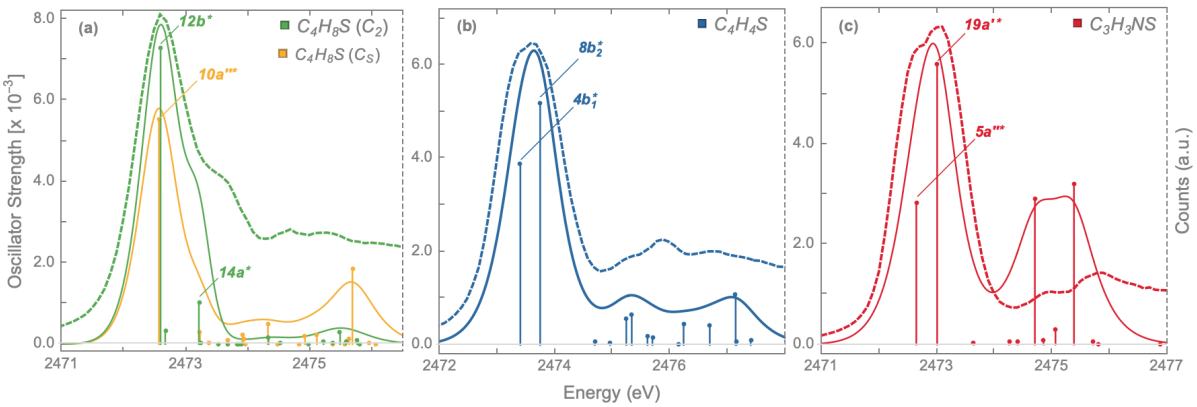

Figure 4.1: *The absorption spectra near S K-edge in thiolane (a), thiophene (b) and thiazole (c). The dashed and solid lines correspond to the experimental and the calculated spectra, respectively. The energy axis was shifted in the calculated spectra by -2.7 eV in thiolane and thiophene and by -3.2 eV in thiazole.*

It is known that the thiolane molecule has different conformers. Therefore, we performed the IS-CASSCF calculations for both thiolane enantiomers, twisted (C_2), and envelope (C_s) geometries. In twisted geometry, the most intense peak corresponds to the transition of the S 1s electron to the LUMO attributed to $12b^*$ in symmetry notation. The shoulder observed at 2473.5 eV is attributed to the transition of the S $1s$ electron to the $14a^*$ molecular orbital. The same feature is also present in the calculated spectrum for the envelope geometry; however, its intensity is strongly reduced. Therefore, the twisted geometry provides a better agreement with the experiment. This agreement is corroborated by Boese *et al.* [169] predictions for the dominance of the twisted conformation for thiolane molecule.

Following, thiophene spectra are presented in Figure 4.1b. The experimental thiophene PEY spectrum (dashed blue line) is dominated by a broad barely resolved peak composed by the transitions from S $1s$ shell to the first two unoccupied molecular orbitals at the photon energies of 2473.2 eV and 2473.6 eV. In Hitchcock's *et. al.* [168] study on X-ray absorption at the S 1s edge of the thiophene molecule, the broad main peak around 2473.4 eV includes the two first transitions, similar to our data. Our calculations (solid blue line) assign them as the excitation to the $4b_1^*$ and $8b_2^*$ molecular orbitals. Similar features observed in thiazole spectrum at 2472.6 eV and 2473.2 eV (Figure 4.1c) are assigned as the excitation to the $5a^{''*}$ and $19a^{'*}$ orbitals, respectively.

Although our theoretical investigation agrees quite well to the experimental data for the two lowest absorption transitions, discrepancies are observed at higher excitation energies due to

the limitations of the approach describing the electronic structure. First of all, the IS-CASSCF approach recovers only part of the electronic correlation energy, so-called dynamic correlation, which needs to be included for both ground and excited states. For excitation of deep core shells such as the Sulfur K-edge, strong relativistic effects must be involved, whereas the DKH approximate Hamiltonian recovers only part of these significant effects. Finally, the appropriate description of the high-energy diffuse states with a mixed valence-Rydberg character requires a larger basis set than the one used in the present study, where we focused our interest on the lowest absorption transitions. A limited basis set is also the reason for the relative energy shift between the experimental and the calculated spectra. However, the value of this shift is only around 0.1% of the transition energies values and the shifted calculated spectra are in good agreement with the experimental data.

An interesting advantage of the IS-CASSCF method is the detailed description of each core excited state by the related wave function. For the S 1s core excitations to LUMO and LUMO+1, which are the focus of our analysis, we found natural orbitals related to the spectator electron. We present these orbitals for all the studied molecules in Figure 4.2.

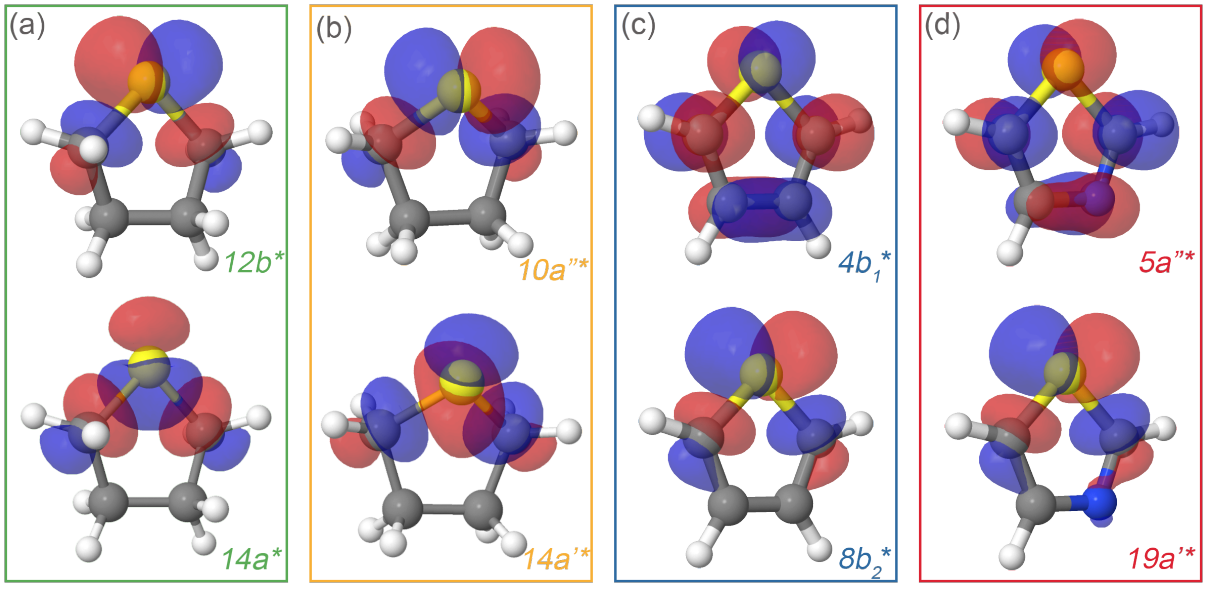

Figure 4.2: *Natural orbitals obtained at IS-CASSCF level, which represent excited electrons for first S 1s absorption transitions for thiolane in twisted (a) and envelope (b) conformations, thiophene (c) and thiazole (d).*

For the thiolane molecule, the shapes of the obtained natural orbitals allow us to assign the 12b^* (Figure 4.2a) and 10$a"^*$ (Figure 4.2b) LUMO orbitals of the twisted and envelope

enantiomers as the σ^*_{SC} orbital. The $14a^*$ (Figure 4.2a) and the $14a'^*$ (Figure 4.2b) orbitals are related to the LUMO+1. An earlier work [168] previously assigned this orbital as a $\pi^*_{CH_2}$, by an analogy with the transition observed in cyclic [170] and non-cyclic [171] alkanes. However, our theoretical analysis shows that it is related to an antibonding σ^*_{SC} orbital which has a mixed Rydberg character of *s*- and *p*- atomic orbitals from Sulfur and the nearest Carbon atoms. The same analysis for the $1s^{-1}$V excited states is presented in Figure 4.2c and Figure 4.2d to thiophene and thiazole, respectively. In both molecules, the LUMO and LUMO+1 are attributed to π^* and σ^*_{SC} orbitals, respectively. Our chemical assignment regarding thiophene agrees with the one proposed by Hitchcock *et. al.* [168] and is confirmed by ΔSCF [172] and PBE [173] calculations.

The core-excited states for the two lowest absorption transitions were described by the analysis of the absorption spectra. Now, we focus on the relaxation process and the final states. The process of KLL Auger electron emission after resonant Sulfur 1*s* excitation can be written as in Equation 4.2.

$$h\nu + S \rightarrow S^*(1s^{-1}V') \rightarrow e^-_{KLL} + S^+(2p^{-2}V) \tag{4.2}$$

where in the first part of the equation, $h\nu$ represents the energy of the incoming X-ray photon and the S is the Sulfur atom in the ground state. In the second part, we have the intermediate state $S^*(1s^{-1}V')$. Here, V' stands for the core-shell electron excited to a valence orbital. The prime on V represents the electron in the valence orbital in the presence of the S $1s^{-1}$ core-hole. The last part of the equation shows the final state $S^+(2p^{-2}V)$, where V without prime represents the electron in the valence orbital in the presence of the S $2p^{-2}$ core-hole. e^-_{KLL} is the resonant KLL Auger electron ejected during the spectator Auger decay of the *K* vacancy. A schematic picture of the spectator resonant Auger decay is given in Section 1.3.

The resonant KLL Auger spectra for the three molecular systems investigated are presented as 2D maps in Figure 4.3. The spectra are vizualized as 2D maps showing the kinetic energy of the Auger electron as a function of the incident photon energy. The intensity is represented by a colorscale. Above the ionization threshold (around 2478 eV), the onset of non-dispersive lines is highlighted by the solid dark blue lines. These non-dispersive lines correspond to *KLL* normal Auger lines, which are independent of the photon energy since the excess of incident energy is transferred to the photoelectron's kinetic energy. Close to the ionization threshold, the presence of the PCI effect is evidenced by the normal Auger lines distorted to higher kinetic energy. The

sloped curves below the ionization threshold highlighted by the dashed lines around the photon energy of 2473 eV correspond to the resonant excitation of the S *1s* electron to LUMO and LUMO+1 orbitals and the subsequent KLL Auger spectator decay.

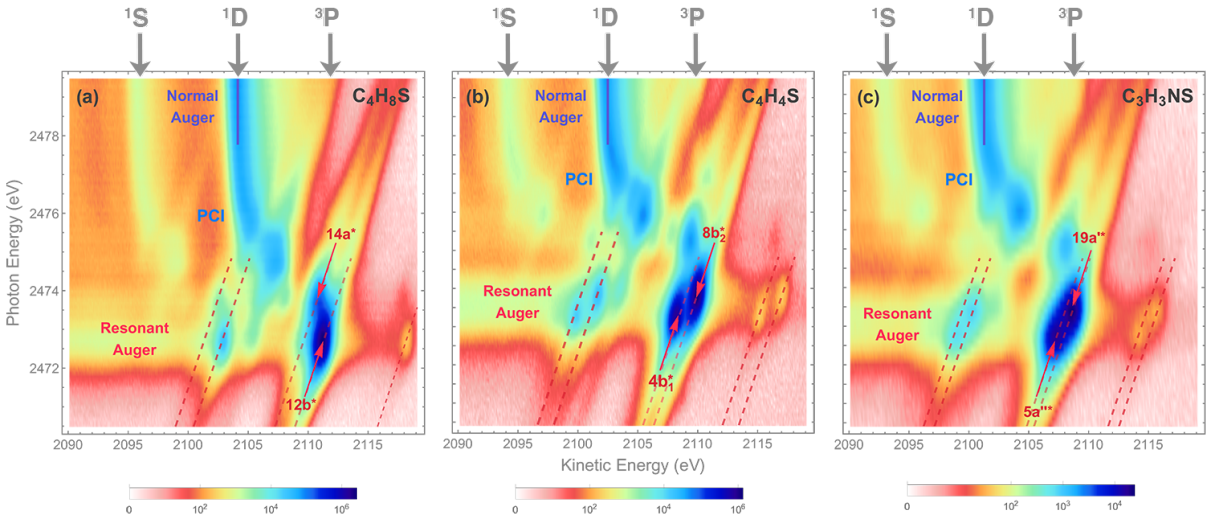

Figure 4.3: *Resonant Auger $KL_{2,3}L_{2,3}$ spectra recorded for (a) thiolane, (b) thiophene and (c) thiazole near the S K-edge.*

The normal Auger spectrum consists of three multiplet lines corresponding to the ^1S, ^1D, and ^3P terms of $2p^{-2}$ final state. Naturally, the multiplets of the normal Auger spectrum observed above the ionization potential (IP) are reproduced for every $2p^{-2}$V final state in the resonant spectator Auger spectrum. However, due to the screening of the core by the spectator electron in the molecular orbital V, the resonant Auger electrons "gain" kinetic energy and the whole multiplet structure is blue-shifted. The screening effect is most efficient for a spectator electron located in the LUMO and weakens for higher molecular orbitals, so that the shift in kinetic energy decreases with the increase of the excitation energy of the spectator electron. Thus, the multiplet structure of the resonant Auger spectrum with a spectator electron in a Rydberg state is only slightly shifted ($1 - 2$ eV) to higher kinetic energies with respect to the normal Auger spectrum, whereas the Auger spectrum with a spectator electron in the LUMO is observed at kinetic energies around 7 eV higher than the normal Auger spectrum. This is illustrated in Figure 4.3. For the case o thiolane (Figure 4.3a) the resonant Auger spectrum with the largest blue shift with respect to the normal Auger spectrum corresponds to the case with an electron in the LUMO $12b^*$. However, in thiophene and thiazole, (Figures 4.3b and 4.3c), the largest shift towards higher kinetic energies corresponds to the resonant Auger decay with

the spectator electron in the σ^*(LUMO+1) $-$ $8b_2^*$ and $19a^{'*}$, respectively. Whereas the resonant Auger decay with the spectator electron in the π^*LUMO ($4b_1^*$ and $5a^{"*}$) manifests a smaller shift of the multiplet structure with respect to the normal Auger spectrum. This indicates a stronger screening of the core in the final state by the electron in the σ^* orbital than by the electron in the π^* orbital. This experimental observation points at the inversion of the orbital order between the S1$s^{-1}V'$ core-excited and final states S2$p^{-2}V$.

High-level quantum-mechanical calculations were applied to elucidate the reason for the observed behavior of the valence orbitals in the aromatic molecules. Once more, we explored the versatility of the IS-CASSCF method. The calculations provide the excitation energies of the intermediate S1$s^{-1}V'$ and the final S2$p^{-2}V$ electronic states, and also a kinetic energy evaluation for the emitted Auger electrons by $E_{exc}(1s^{-1}V') - E_{exc}(2p^{-2}V)$. Our multi configurational state-averaged wave function includes all the three possible electronic states for a singly ionized molecule with two holes in the S $2p$ shell. For the three molecules, the lower energy final states found are related to open-shell configurations, in which the most relevant contains each vacancy in a different S $2p$ orbital. The results for all the investigated molecular systems, are in agreement with the experimental observations (Table 4.1). In thiophene and thiazole, the calculations show that a core-excited intermediate state with an electron in the LUMO S1$s^{-1}\pi^*$ relaxes into a final state S2$p^{-2}\pi^*$ with the energy around 360 eV with respect to the ground state, whereas the intermediate state with an electron in the LUMO+1 S1$s^{-1}\sigma^*_{\mathrm{SC}}$ relaxes into a final state S2$p^{-2}\sigma^*_{\mathrm{SC}}$ with energy close to 359 eV. Thus, our calculations demonstrate the inversion of orbital order between the intermediate and the final states. The corresponding Auger electron energies obtained from the calculations qualitatively reproduce the trends observed in the experimental Auger spectra. Concerning the thiolane molecule, the intermediate state with the spectator electron in LUMO+1 (S 1s^{-1} $14a^*$ for C2 and S 1s^{-1} $16a^{'*}$ for Cs geometries) lead to resonant Auger electron with lower kinetic energy compared with the excited state with the spectator electron in LUMO (S 1s $12b^*$ for C2 and S 1s $10a^{''*}$ for Cs geometries), which leads to a resonant Auger electron with higher kinetic energy. In this case, the orbital order remains unchanged as observed in the experimental data.

Table 4.1: *Experimental and theoretical excitation energies and Auger electron energies. Excitation energies are given in electron-volts (eV) with respect to the ground state.*

Molecule	Intermediate State			Final State	Excitation Energy	Auger Electron Energy	
	Attribution	Exp.	Calc.	Main Configuration	Calc.	Exp.	Calc.
C_4H_8S (C_2)	S 1s $\rightarrow 12b^*$ ($S\ 1s^{-1}\sigma^*_{SC}$)	2472.6	2475.29	S $2p_x^{-1}2p_z^{-1}12b^*$	356.25		2119.04
				S $2p_x^{-1}2p_y^{-1}12b^*$	356.63	2111.1	2118.66
				S $2p_y^{-1}2p_z^{-1}12b^*$	356.71		2118.58
	S 1s $\rightarrow 14a^*$ ($S\ 1s^{-1}\sigma^*_{SC}$)	2473.5	2475.91	S $2p_x^{-1}2p_y^{-1}14a^*$	357.76		2118.15
				S $2p_x^{-1}2p_z^{-1}14a^*$	357.98	2110.9	2117.93
				S $2p_y^{-1}2p_z^{-1}14a^*$	358.14		2117.76
C_4H_8S (C_s)	S 1s $\rightarrow 10a''^*$ ($S\ 1s^{-1}\sigma^*_{SC}$)	2472.6	2475.26	S $2p_x^{-1}2p_z^{-1}10a''^*$	356.27		2118.99
				S $2p_x^{-1}2p_y^{-1}10a''^*$	356.64	2111.1	2118.62
				S $2p_y^{-1}2p_z^{-1}10a''^*$	356.73		2118.53
	S 1s $\rightarrow 16a'^*$ ($S\ 1s^{-1}\sigma^*_{SC}$)	2473.5	2475.92	S $2p_x^{-1}2p_y^{-1}16a'^*$	358.18		2117.75
				S $2p_x^{-1}2p_z^{-1}16a'^*$	358.44	2110.9	2117.49
				S $2p_y^{-1}2p_z^{-1}16a'^*$	358.58		2117.34
C_4H_4S	S 1s $\rightarrow 4b_1^*$ ($S\ 1s^{-1}\pi^*$)	2473.2	2476.10	S $2p_x^{-1}2p_y^{-1}4b_1^*$	360.01		2116.09
				S $2p_x^{-1}2p_z^{-1}4b_1^*$	360.09	2108.2	2116.00
				S $2p_y^{-1}2p_z^{-1}4b_1^*$	360.18		2115.91
	S 1s $\rightarrow 8b_2^*$ ($S\ 1s^{-1}\sigma^*_{SC}$)	2473.6	2476.44	S $2p_x^{-1}2p_z^{-1}8b_2^*$	358.47		2117.97
				S $2p_x^{-1}2p_y^{-1}8b_2^*$	358.88	2109.8	2117.56
				S $2p_y^{-1}2p_z^{-1}8b_2^*$	359.10		2117.34
C_3H_3NS	S 1s $\rightarrow 5a''^*$ ($S\ 1s^{-1}\pi^*$)	2472.6	2475.84	S $2p_x^{-1}2p_y^{-1}5a''^*$	359.77		2116.07
				S $2p_x^{-1}2p_z^{-1}5a''^*$	359.88	2107.2	2115.96
				S $2p_y^{-1}2p_z^{-1}5a''^*$	359.95		2115.89
	S 1s $\rightarrow 19a'^*$ ($S\ 1s^{-1}\sigma^*_{SC}$)	2473.2	2476.20	S $2p_x^{-1}2p_z^{-1}19a'^*$	358.58		2117.62
				S $2p_x^{-1}2p_y^{-1}19a'^*$	358.96	2108.5	2117.24
				S $2p_y^{-1}2p_z^{-1}19a'^*$	359.18		2117.02

The comparison between the two aromatic molecules with thiolane, a saturated molecule, suggests that the observed orbital order inversion is related to the conjugation character of thiophene and thiazole. In order to reveal the role of conjugation effects, we applied the NBO analysis for the ground, and the core ionized states S $1s^{-1}$ and S $2p^{-2}$, relevant for the analysis of the intermediate and final states, respectively. The Lewis-like description for these states enables the evaluation of the orbital interactions by the Second Order Perturbation Analysis of the Fock Matrix. The analysis is limited to Hartree-Fock wave functions, which were applied here whithin the IS-ROHF approach for the ionized states, and the stabilization energies values,

$\Delta E^{(2)}$, quantify the results. We focused the analysis in terms of two relevant chemical concepts which can be rationalized in the scope of the interaction between pairs of NBOs: the conjugation effect, related to interactions between π-type orbitals, and the hyperconjugation effect, mostly related to interactions between σ-type orbitals. Both effects are significant for stabilizing the chemical structure in core excited states, and they can explain the change in the energy order found for the two lowest excited states, when comparing the S $1s^{-1}$V' and S $2p^{-2}$V states, in thiophene and thiazole molecules.

The discussion on NBO interactions begins by the conjugation effect, where the π^* orbital plays the acceptor role. There are two lone pairs in the Sulfur atom: one with hybrid sp^2 character (LP(1) S in NBO notation) and another one with pure $p-$ character (LP(2) S), which has the same orientation of the other π^* orbitals. As should be expected, only the $p-$type lone pair takes part in the interaction with the π^* NBOs. Another important interaction in thiophene comes from the bonding π (BD(2) (C-C)) and the alternate antibonding π^* (BD*(2) (C-C)) NBOs. A similar shape is also found for the interactions of the antibonding π^* orbitals (BD*(2) (C-C) and BD*(2) (C-N)) in thiazole molecule. The representation of these interactions can be found in Figure 4.4.

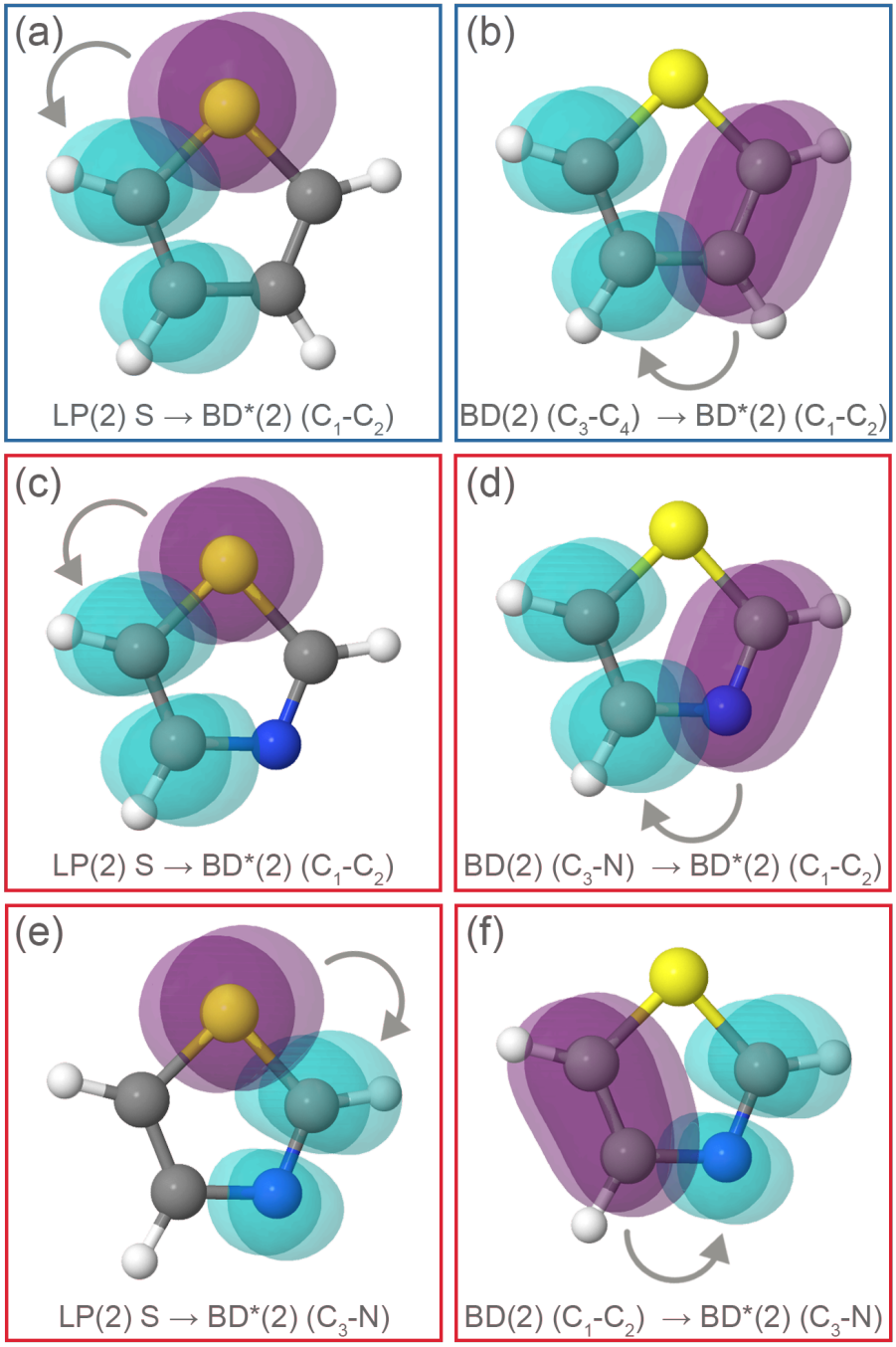

Figure 4.4: *Natural Bond Orbitals representation of the Second-Order Perturbation interaction between donor (in purple) and π^* acceptor (in cyan) for (a, b) thiophene and (c, d, e, f) thiazole.*

The stabilization energies $\Delta E^{(2)}$ obtained for the most relevant interactions are presented in Table 4.2. Starting from the ground state, the interactions between Sulfur $p-$type lone pairs and antibonding π^* NBOs quantify the effect of the stabilization by the aromatic character of both molecules. This quantification highlights the importance of the pair interaction for the electronic ground state's chemical structure. The situation dramatically changes when considering the

intermediate and final states, where the stabilization energy values noticeably decrease, implying a reduction in the chemical structure stability in the core-ionized states. It means that the conjugation effect becomes less effective. A similar behavior can be observed for the interaction between alternate π and π^* NBOs, where the stabilization energies also decrease from the ground state to the final states. Moreover, the promotion of a core electron to the antibonding π^* orbitals should also contribute to the chemical structure destabilization once it lowers the electronic conjugation and, therefore, the aromaticity of the heterocyclic molecules.

Table 4.2: *Results from Second-order Perturbation Theory Analysis of Fock Matrix in NBO Basis. Stabilization energies $\Delta E^{(2)}$ for the conjugation interactions in eV. Symmetrically equivalent NBO interactions are omitted due to redundancy.*

Molecule	NBO Orbital		Stabilization Energy $\Delta E^{(2)}$				
	Donor	Acceptor	Ground	S $1s^{-1}$	S $2p_x^{-1}p_z^{-1}$	S $2p_x^{-1}p_y^{-1}$	S $2p_y^{-1}p_z^{-1}$
C_4H_4S	LP(2) S	BD*(2) (C_1-C_2)	1.753	1.090	0.990	0.995	0.992
	BD(2) (C_3-C_4)	BD*(2) (C_1-C_2)	1.197	0.801	0.401	0.412	0.438
C_3H_3NS	LP(2) S	BD*(2) (C_1-C_2)	1.565	0.722	0.378	0.378	0.404
	LP(2) S	BD*(2) (C_3-N)	2.447	1.005	0.565	0.567	0.602
	BD(2) (C_3-N)	BD*(2) (C_1-C_2)	1.572	1.173	1.163	1.166	1.164
	BD(2) (C_1-C_2)	BD*(2) (C_3-N)	1.023	0.828	0.743	0.749	0.746

Furthermore, the stabilization energies resulting from the interaction of the π^* NBO orbitals when interacting with the S sp^2 lone pair orbital are negligible ($\Delta E^{(2)}$ <0.01 eV). The sp^2 lone pair LP(1) S has a perpendicular orientation to the π system of the molecule, meaning that the interaction between these NBO pairs is minimal and is ineffective in stabilizing the ideal Lewis chemical structure, even for the ground state.

Another insight can be achieved if one considers the hyperconjugation effects. In this case, we focus our analysis on the orbital interactions where the pair of σ^*_{SC} (BD*(1) (S-C)) NBOs acts as acceptors. We found mainly two types of donor NBOs: the σ bond between carbon and hydrogen atoms (BD(1) (C-H)) and between the adjacent carbon atoms (BD(1) (C-C)). Taking the sulfur atom position as reference, it should be noticed that the interactions with σ_{CH} NBOs can be geminal, when related to the nearest carbon atom, or vicinal, when from the next neighbor carbon atom. Particularly for the thiazole molecule, we also have the equivalent of these donors, by the Nitrogen lone pair (LP(1) N) and its σ bond with the related carbon atom

(BD(1) (C-N)). The representation of all the mentioned interactions can be found in Figure 4.5.

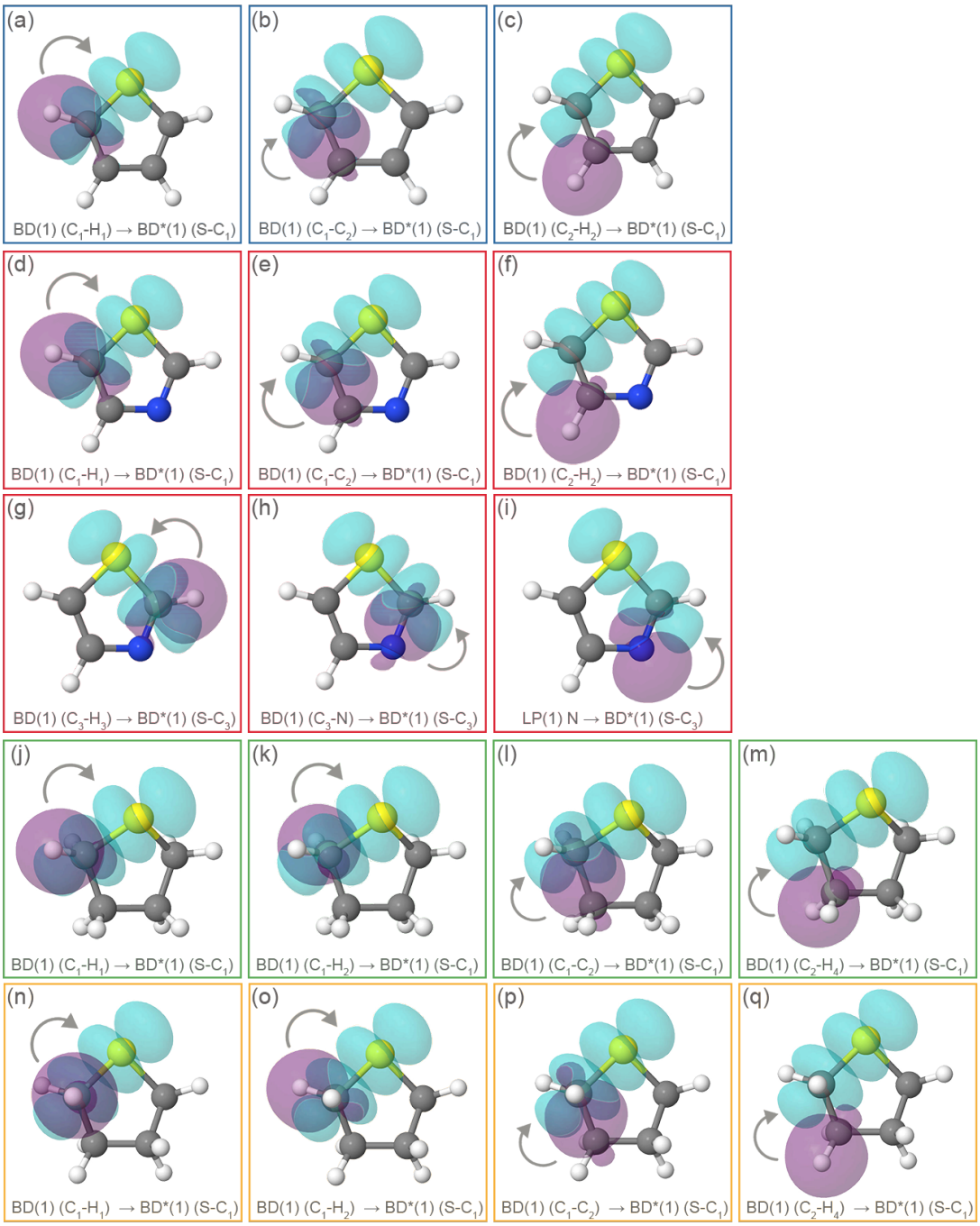

Figure 4.5: *Natural Bond Orbitals representation of the Second-Order Perturbation interaction between donor (in purple) and σ^*_{SC} acceptor (in cyan) for (a-c) thiophene, (d-i) thiazole, (j-m) envelope thiolane conformer and (n-q) twisted thiolane conformer.*

The stabilization energies $\Delta E^{(2)}$ for the most relevant $\sigma-$type interactions are presented in Table 4.3 for all investigated systems. For the ground state, the major stabilizing interactions come from the vicinal σ_{CH} NBOs. Including the intermediate and final states in the analysis, the

stabilization energy values increase for all the selected NBO pairs. Consequently, we can assume that the hyperconjugation effect surprisingly becomes more relevant to the chemical structure of these heterocyclic molecules in core ionized states. Comparing over the different core ionization levels, we also found that the interactions of the σ^*_{SC} NBOs with its geminal σ_{CC} NBOs have the smallest energetic contribution. In contrast, the nitrogen lone pair NBO (LP(1) N), exclusive for the thiazole molecule, stands out with the highest stabilization energy values.

Table 4.3: *Results from Second-order Perturbation Theory Analysis of Fock Matrix in NBO Basis. Stabilization energies $\Delta E^{(2)}$ for the hyperconjugation interactions in eV. Symmetrically equivalent NBO interactions are omitted due to redundancy.*

Molecule	NBO Orbital		Stabilization Energy $\Delta E^{(2)}$				
	Donor	Acceptor	Ground	S $1s^{-1}$	S $2p_x^{-1}p_z^{-1}$	S $2p_x^{-1}p_y^{-1}$	S $2p_y^{-1}p_z^{-1}$
C_4H_4S	BD(1) (C_1-H_1)	BD*(1) (S-C_1)	<0.010	0.118	0.292	0.309	0.302
	BD(1) (C_1-C_2)	BD*(1) (S-C_1)	<0.010	0.041	0.150	0.143	0.149
	BD(1) (C_2-H_2)	BD*(1) (S-C_1)	0.210	0.303	0.460	0.460	0.462
C_3H_3NS	BD(1) (C_1-H_1)	BD*(1) (S-C_1)	0.010	0.113	0.274	0.290	0.284
	BD(1) (C_3-H_3)	BD*(1) (S-C_3)	0.033	0.175	0.346	0.363	0.355
	BD(1) (C_1-C_2)	BD*(1) (S-C_1)	<0.010	0.051	0.166	0.157	0.164
	BD(1) (C_6-N)	BD*(1) (S-C_3)	<0.010	0.059	0.150	0.145	0.150
	BD(1) (C_2-H_2)	BD*(1) (S-C_1)	0.181	0.270	0.415	0.413	0.415
	LP(1) N	BD*(1) (S-C_3)	0.691	1.088	1.739	1.746	1.751
C_4H_8S (C_s)	BD(1) (C_1-H_1)	BD*(1) (S-C_1)	0.017	0.147	0.363	0.378	0.374
	BD(1) (C_1-H_3)	BD*(1) (S-C_1)	0.020	0.147	0.351	0.351	0.356
	BD(1) (C_1-C_2)	BD*(1) (S-C_1)	<0.010	0.087	0.233	0.228	0.235
	BD(1) (C_2-H_4)	BD*(1) (S-C_1)	0.162	0.264	0.432	0.434	0.435
C_4H_8S (C_2)	BD(1) (C_1-H_2)	BD*(1) (S-C_1)	0.019	0.148	0.356	0.362	0.363
	BD(1) (C_1-H_1)	BD*(1) (S-C_1)	0.018	0.147	0.358	0.369	0.368
	BD(1) (C_1-C_2)	BD*(1) (S-C_1)	<0.010	0.090	0.235	0.228	0.235
	BD(1) (C_2-H_4)	BD*(1) (S-C_1)	0.172	0.291	0.481	0.483	0.484

Our analysis shows that in aromatic molecules relaxation of a core-excited S $1s^{-1}$ state via Auger decay to the final S $2p^{-2}$ state is accompanied by a significant drop of the stabilization energy resulting from conjugation interactions of π-type and by the enhancement of stabilization energy resulting from hyperconjugation interactions of σ-type. The combination of both stabilization energy $\Delta E^{(2)}$ trends is in line with the changes observed for the relative energy order

of the π^* and σ^* inner-shell excited states, as observed for thiophene and thiazole molecules.

Although the stabilization energy $\Delta E^{(2)}$ is a useful notion to describe the electronic structure changes in aromatic molecules, it does not provide a quantitative comparison to the calculated transitions energies at the same level of theory or to the experimental results. These energy values do not have a direct physical comparable observable, and they are related only to the NBO Lewis-like description of the chemical structure. An extensive investigation of the NBO interactions and the application of the same analysis for a larger group of molecules is needed to obtain more quantitative statements. A similar approach was successfully applied in the interpretation of vibrational spectroscopic measurements by the evaluation of the hyperconjugation effects in amide molecules.[174]

The ionization of inner-shell orbitals should differ from the valence ionization, in which the electronic system can be rearranged spatially over the molecule to reduce the deficiency of the negative charge. By the NBO analysis, the first valence ionization breaks the π bonds and removes any electronic conjugation effect from the chemical structure of these molecular systems. However, the core electrons removal outcome would be the increase of the effective nuclear charge, primarily on the electrons located near the core ionized atom; *i.e.*, the Sulfur atom. Their electronic density would be tight to the nucleus and then the overlap between NBO pairs involved in the electronic conjugation decreases while it increases for hyperconjugation pairs. Our analysis shows that the core ionization, or even the core excitation, has a strong and localized electrostatic character over the molecular electronic structure. The energy reorders of the first two final states S $2p^{-2}$V in comparison with intermediate S $1s^{-1}$V states is a particular behavior of inner-shell states created by a localized charge inequality.

4.4 Conclusion

The opportunity to conduct HAXPES experiments under state-of-the art conditions at GALAXIES beamline enabled us to perform high-resolution resonant Auger spectroscopy. The measured resonant Auger Sulfur $KL_{2,3}L_{2,3}$ 2D maps for thiophene and thiazole show the inversion of the energy order of the two lowest core-excited states between the intermediate (S $1s^{-1}$V') and the final (S $2p^{-2}$V) states. This effect is absent in the similar measurements in thiolane, the saturated analog of thiophene. We applied high-level quantum-mechanical calculations to understand this

behavior. The intensities and excitation energies for the core-excited states and the excitation energies of the final states were obtained by applying the IS-CASSCF method. This multi configurational approach recovers important effects of relaxation and electronic correlation through a self-consistent procedure. We also obtained the kinetic energies of the Auger electron from the calculated final and intermediate states' excitation energies. For the conjugated molecules, the two lowest S $1s^{-1}$V' excited states are assigned to the core electron promotion to the π^* and σ^*_{SC} orbitals, respectively. Our calculations agree with the measurements in the three molecules studied. It reproduced the inversion in the two lowest states' energy levels between the excited and final states in thiophene and thiazole, as well as the absence of this effect in thiolane.

In order to reveal the effect of electronic orbital interactions, we performed NBO analysis for the ground, and the core ionized states S $1s^{-1}$ and S $2p^{-2}$, relevant to the S $1s^{-1}$V excited and S $2p^{-2}$V final states. The NBO analyses allowed us to give a chemical description for the behavior observed in thiophene and thiazole 2D maps since the conjugation effect presents itself as a clue in explaining the reason for the observed phenomenon. The second-order perturbation analysis of the Fock matrix allow us to obtain the stabilization energy ($\Delta E^{(2)}$), which provides qualitative information on the orbitals pair interactions. The observed inversion of the orbital order is attributed to the electronic conjugation and hyperconjugation effects, which contribute to the chemical structure stabilization. Our calculations reveal a strong interaction between the pure S p-type lone pair and the antibonding π^* orbital from the ring in the ground state. A drastic downtrend in $\Delta E^{(2)}$ occurs in the core-ionized states S $1s^{-1}$ and S $2p^{-2}$, meaning a decrease in the stabilization of the chemical structure of the thiophene and thiazole molecules following the Auger decay. The opposite trend was found for hyperconjugation interactions, between the pairs of σ_{CH} and σ_{CC} orbitals with the antibonding σ^*_{SC} orbital.

Therefore, a combination of both trends provides a chemical interpretation of the observed inversion of the orbital order in aromatic molecules undergoing resonant core-excitation and Auger decay. The described effect is specific to the conjugated heterocycles since it emerges from the interaction between the lone pair of the heteroatom and the $\pi-$system in the aromatic ring. The discovered phenomenon has been recently observed in polythiophene (as presented in the Chapter 5) and, thus, is not limited to isolated molecules. This effect is expected to be general for other conjugated heterocycles as well as for larger conjugated systems like polymers.

Chapter

5 Electron Dynamics in Sulfur-Based Polymers Using Core-Hole Clock Spectroscopy

Chapter content

Introduction

Ultrafast processes are commonly investigated performing laser pump-probe experiments. Briefly, a laser pump pulse excites the target system, and a probe pulse tracks its temporal evolution as a function of the delay between the two pulses. So, the measurement is carried out in the time domain. Recently, pulse compression in the extreme ultraviolet down the subfemtosecond timescale has been demonstrated, allowing studies on electron delocalization in small molecules.

[41, 42] Notwithstanding that this tool is used to measure processes on the timescale of hundreds of attoseconds in molecules, the optical laser pulses experiments typically last several femtoseconds for studies on more complex systems such as conjugated organic molecules. Alternatively, the CHCS can be applied to obtain information on dynamical processes. The CHC method is based on core-level excitation and decay with an intrinsic time scale based on the lifetime of the intermediate (core-hole) state. So, in this case, the measurements are performed in the energy domain. Furthermore, core electrons are involved, enabling the atomic specificity singular to core spectroscopies. The lifetime of the intermediate state is in the order of few femtoseconds or even hundreds of attoseconds. Electron delocalization in organic semiconductors usually occurs at ultrafast electron dynamics on time scales of few femtoseconds. Therefore, CHC is a desirable approach in the study of electron-transfer dynamics in conjugated organic molecules.

Conjugated organic molecules have been widely studied in materials sciences in the past years since it was discovered in 1977 the polymers' conductive properties. [175] Briefly, the electric conduction is formed by the $\pi-$electrons delocalized over several carbon atoms along the polymer backbone. Organic semiconductors allow for solution-based fabrication, enabling low-cost, low-weight, flexible, and more sustainable materials. Thiophene-based conjugated polymers such as polythiophene (PT) are particularly relevant for application as semiconducting polymers due to their stability in several redox states and their optical, mechanical, and electronic properties. Alkyl side-chains, among which hexyl chains, have been added to PT to make it soluble in organic solvents. The PT analog with hexyl chains is P3HT (poly(3-hexylthiophene)). The presence of the side chains plays a major role also in the polymer organization, which influences changes in the properties of the material, such as the charge transport. Due to these characteristics, this class of materials can be applied in electronic devices and photonics. Among the numerous examples of devices are organic field-effect transistors (OFETs), span LEDs, and organic photovoltaics (OPVs). [176–178] An important characteristic of the OPVs is charge transport, which represents one of the significant limitations for their performances. [179] In detail, the charge transport in OPVs is linked to the electron transfer between neighbor molecules. Note that the electron transfer to neighboring molecules is generally referred to as charge transfer in several studies involving electron dynamics on semiconducting polymers.

Ultrafast electron dynamics phenomenon was reported in studies on thiophene-based oligomers and polymers using resonant Auger electron spectroscopy, one of the CHC techniques. Recently,

a work performed RAS measurements at the carbon K-edge in the polycrystalline oligothiophene thin-film series quaterthiophene (T4), quinquethiophene (T5), and sexithiophene (T6) to investigate the effect of the oligomer length on ultrafast electron transfer times [180]. The most considerable ultrafast charge transfer rates were observed for T5 around three times higher compared with the T6. The manifestation of the odd/even effect is suggested to explain these differences in the charge transfer rates. The effect of structural periodicity on the conduction properties was explored using an example of conjugated polythiophene polymers [181]. Interestingly, despite the periodic structure and extended electronic states across the polymer chain, no signature of electron delocalization using resonant Auger spectroscopy has been observed in the powdered samples. However, a subsequent study of the same polymer deposited on a substrate as a thin film revealed electron delocalization in the low-femtosecond regime [59]. The possible interpretation of this effect relates the observed electron dynamics to the interaction between the polymer chains in the highly ordered films. This hypothesis was further corroborated by the studies in poly(3-hexylthiophene) [60] and poly(bithiophene) [182] showing a correlation between the conductive properties of the material and its morphology: highly oriented configuration favors a more efficient electron delocalization process. However, further studies are required to clarify the mechanisms responsible for this correlation.

We investigated ultrafast electron dynamics in PT and P3HT thin-film polymers deposited onto an ITO (indium tin oxide) substrate coated glass. We performed resonant Auger electron spectroscopy measurements at two different angles of the photon beam incidence to the samples, 10° and 70°, which will be referred to as measurements at grazing and normal photon beam incidence to the samples. P3HT thin films were characterized by XRD and AFM measurements to obtain information on orientation and thickness. P3HT thin-films exhibit a strong angular dependence evidenced by the difference of relative intensities of the spectator Auger contributions resulting from resonant excitation to π^* and σ^* molecular orbitals depending on the incident photon beam angle with respect to the surface sample. This behavior is due to relatively well-organized polymer chains in the film. In contrast, for PT, weak angular dependence was observed. Our results suggest that the spectator electron delocalizes mainly from the σ^* (LUMO+1) for both studied cases. Moreover, a hint of an additional delocalization pathway from the π^* (LUMO) is observed for P3HT. Furthermore, we obtained the charge transfer rate for both cases. Theoretical calculations are necessary to get information on the mechanism of electron delocalization.

This work was performed in collaboration with Prof. Dr. Maria Luiza Rocco, full professor at Instituto de Química, Universidade Federal do Rio de Janeiro (Brazil), who provided the PT samples and the expertise for polymers measurements. The P3HT film preparation, characterization by XRD and AFM was performed in collaboration with Dr. Laure Fillaud, maître de conferences at LISE, Sorbonne Université.

5.1 Formalism

5.1.1 Electronic Structure of Semiconducting Materials

Essentially, a polymer backbone comprises a large number of repeated units of molecules named monomers. The electric properties and the conductivity in a material are directly related to its electronic structure. For metals, the atomic orbitals overlap with equivalent orbitals of neighboring atoms in all directions, creating continuous molecular orbitals proportional to the number of atoms involved. This effect gives rise to an energy band responsible for the conductive properties of metals. The so-called semiconducting polymers are $\pi-$conjugated polymers. Their electronic structure originates from the sp^2p_z hybridized wavefunctions of the carbon atoms in the repeat unity. These chemical systems are described in terms of the energy bands that arise from the bonding and anti-bonding energy levels related to the $\sigma-$bonds between adjacent carbon atoms created from the sp^2 wavefunctions and the orthogonal $\pi-$bonds that originate from the p_z wavefunctions. Despite the $\sigma-$bonds maintain the structure together, the $\pi-$bonds are the heart of the properties that characterize conjugated polymers as semiconductors. A pictorial representation of the band diagram for $\pi-$conjugated polymers is shown in Figure 5.1.

The wavefunctions of the $\pi-$bands are linear combinations of the p_z orbitals from the carbon atoms in each repeat unit. In the one-electron approximation, where the electron-electron Coulomb interaction is neglected, the number of sub$-\pi-$bands is determined by the number of carbon atoms in the monomer of the polymer. These bands have similar behavior as the energy bands in metals leading to electron delocalization along the polymer's backbone. This electronic delocalization provides a kind of "path" for charge mobility along the backbone of the polymer chain. In other words, the explanation for the semiconductor characteristic of organic polymeric materials lies in the conjugated structure of its monomers. Because of this characteristic, when the polymer is formed, the orbitals are extended along the polymer chain, acting equivalently to

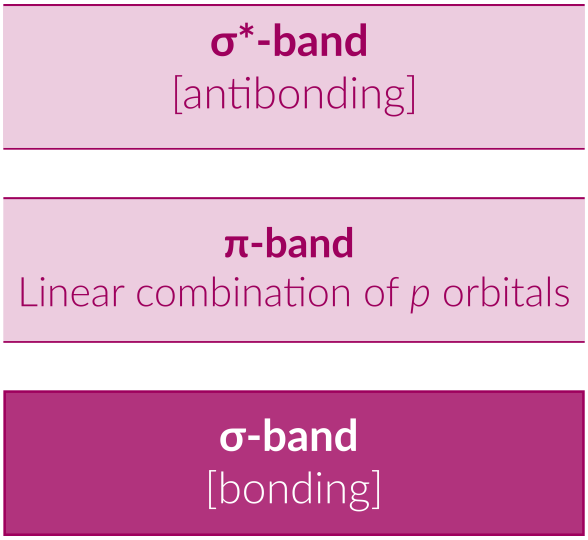

Figure 5.1: *Pictorial representation of the band diagram for $\pi-$conjugated polymers. Adapted from [183].*

the formation of the valence band in inorganic semiconductors. [183]. The extent of the system and its interactions are crucial for the electronic structure of the film, which in turn controls key parameters for its application in materials science, such as molecular absorption and optical emission, redox characteristics, among others.

5.1.2 Charge Transfer Rate

In Section 1.3, we introduced the core-excitation and its subsequent relaxation processes. In the photoexcitation of a target chemical system, the electron is promoted to an unoccupied molecular orbital. During the excited-state lifetime, this promoted electron might remain localized in the vicinity of the core-hole. In other words, the molecular orbital's wavefunction where the excited electron is placed overlaps with that of the core-hole. In the electron transfer process, the promoted electron delocalizes, i.e, transfers away from the core-hole. In this case, the overlapped wavefunction drops to zero leading to a quenching of the resonant channels (participator and spectator) in the decay of the intermediate state. Then, the decay channel converges to normal Auger decay, leading to a two-hole final state configuration. The quenching of the resonant channels represents, in this way, a signature of dynamic electron transfer.

The charge transfer rate can be defined as the characteristic time required for the promoted core electron to delocalize to a neighbor system and is given in relation to the lifetime of the core-excited state, τ_{CH}. The necessary conditions for observing charge transfer dynamics are

the strength of the intermolecular electronic coupling and the relative (local) energy levels. If one assumes the electron transfer to a neighbor molecule as a tunneling process with exponential probability as a function of time, one can directly compare this process with the core-hole decay rate, which is also described by an exponential probability. Here, it is assumed that the two processes are independent. [47] According to Fermi Golden Rule, the electron delocalization and Auger decay can be treated as first-order processes (Equation 5.1).

$$\frac{dN(t)}{dt} = -\frac{\Gamma}{\hbar}N(t) \tag{5.1}$$

where $dN(t)/dt$ is the decay rate, $\hbar/\Gamma$ is the characteristic time for the decay ($\hbar/\Gamma \equiv \tau$), Γ is the lifetime width of the process, and N is the set of identical core-excited states. A solution for Equation 5.1 is given by Equation 5.2.

$$N(t) = N_0 e^{-t/\tau} \tag{5.2a}$$

$$N(t) = N_0 exp\left(-\frac{\hbar}{\Gamma}t\right) \tag{5.2b}$$

where $N(t)$ is the number of systems left in the excited state at time t and N_0 is the set of decaying systems at an arbitrarily chosen time zero. Therefore, the Equation 5.2 gives the information about the systems which remain in the excited state upon the decay time t. The time-dependent decay event probability, $P(t)$, for the decay events to occur for times less than or equal to a given time T can be obtained by the integral of the ratio between the Equation 5.1 and N_0 over that time T (see Equation 5.3).

$$P(t) = 1 - \int_0^T \frac{\Gamma}{\hbar} exp\left(-\frac{\Gamma}{\hbar}t\right)\, dt \tag{5.3}$$

Since the resonant decay channel and the charge transfer channel compete, the ratio of the total numbers of events through the two channels has to be considered. Measuring a spectrum corresponds to $T \to \infty$. From the combination of the possible events, one can obtain the Equation 5.4 (see reference [47]).

$$P_{CH}^{CT} = \frac{\Gamma_{CT}}{\Gamma_{CH} + \Gamma_{CT}} \tag{5.4}$$

where $\hbar/\Gamma_{CH}$ and $\hbar/\Gamma_{CT}$ are the characteristic times for the core-hole decay and charge transfer, respectively. Γ_{CH} is the lifetime width of the core-hole, and Γ_{CT} is the lifetime width of the

charge transfer. These widths are proportional to the measurable spectral integrated intensities *I*. Therefore, one can write the Equation 5.5a.

$$\frac{\Gamma_{CT}}{\Gamma_{CH}+\Gamma_{CT}} = \frac{I_{Auger}}{I_{Auger}+I_{res}} \tag{5.5a}$$

$$\frac{\frac{\hbar}{\tau_{CT}}}{\frac{\hbar}{\tau_{CH}}+\frac{\hbar}{\tau_{CT}}} = \frac{I_{Auger}}{I_{Auger}+I_{res}} \tag{5.5b}$$

where I_{res} is the intensity of resonant spectator decay spectral contribution and I_{Auger} corresponds to the decay where final state configuration is *2h* similar as in the normal Auger decay, respectively. The Equation 5.5b can be written as presented in Equation 5.6 for the charge transfer rate, τ_{CT}. [47, 184]

$$\tau_{CT} = \frac{I_{res}}{I_{Auger}}\tau_{CH} \tag{5.6}$$

We obtained the charge transfer rates for our studied polymers. Note that this quantity does not directly describe the transfer time, which can be much faster. The τ_{CT} is rather a characteristic of the conduction properties of the polymer and describes the possibility of an electron to delocalize from the initially excited orbital to where the excited electron is being transferred to.

5.2 Experimental Details

5.2.1 Sample Preparation

Commercial polymers from Sigma-Aldrich® have been used throughout this study [185]. The P3HT polymer depositions in this work were done by spin-coating 0.5 wt% (5 mg/ml) regioregular P3HT solution in chloroform ($CHCl_3$) on ITO substrates with 1500 - 2000 revolutions per minute (rpm) spin frequency. In this method, a small pump maintain the substrate on its holder without mechanical constraint by aspiration. A small amount of the polymer in solution is deposited on the substrate. Then, the high-speed rotation spreads evenly the polymer solution on the substrate and enables the uniform evaporation of the solvent. This method is typically used for deposition of thin and uniform layers on small substrates in the order of a few square centimeters. One can consider a film to be thin, ranging from 10 nm to a few hundred nanometers.

In particular for P3HT, the $\pi-$stacking of the polymer chains occurs during the solvent evaporation process. It was evidenced by changing in color from orange to purple, which is induced by the formation of well-ordered P3HT aggregates. PT film was prepared by the potentiostatic deposition method on ITO substrate and the thickness was controlled by time deposition.

5.2.2 Atomic Force Microscopy Characterization

The polymer films thickness was determined using Atomic Force Microscopy (AFM) scratching measurements. The results are presented in Figure 5.2. Essentially, the AFM tip is scanned under strong loading forces to remove the film, leaving deep trenches in the sample. The deepness of this trenches are obtained and then, thickness of the film is known. In detail, a 5 μm x 5 μm P3HT pristine was imaged (Figure 5.2a). Then, the pristine was scratched using an AFM tip in contact mode by applying a force$_1$ (Figure 5.2b), and we find a thickness of 33 nm (Figure 5.2d). A force$_2$, was applied (Figure 5.2c) where force$_2$ > force$_1$ to assure that the bottom of the layer was reached and a similar thickness of 34 nm was found (Figure 5.2e). Since the thickness of thin-films range from few nanometers up to around 100 nanometers our samples can be considered as thin-films.

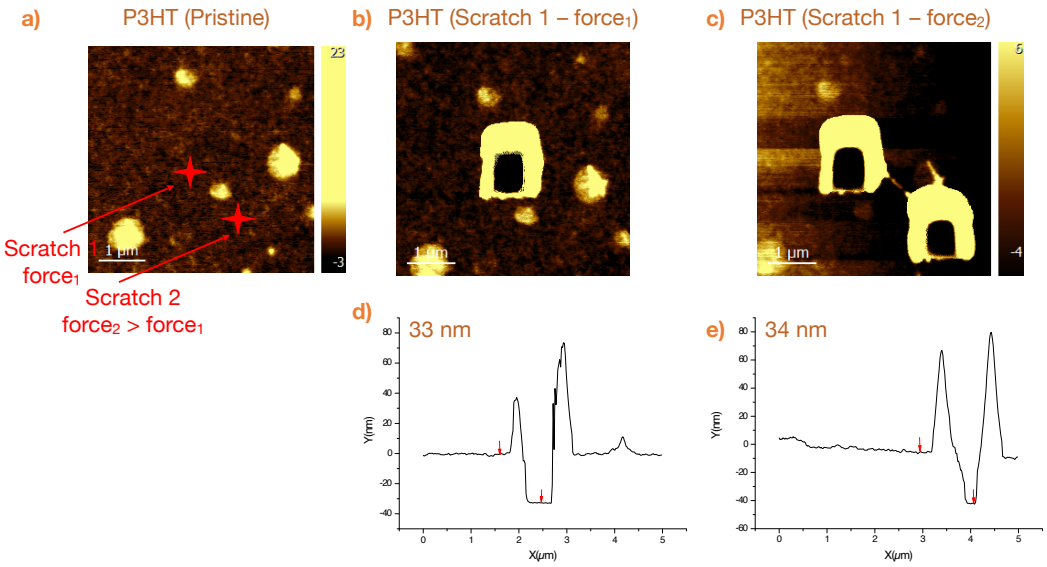

Figure 5.2: *Images of the scratching of P3HT sample by AFM to determine the sample thickness. 5.2a: pristine P3HT sample. 5.2b: first scratch on the sample by a loading force$_1$. 5.2c: second scratch on the sample by a loading force$_2$, where force$_2$ > force$_1$. The panels 5.2d and 5.2e shows the depth of 33 nm and 34 nm, resulting from the scratch using force$_1$ and force$_2$, respectively.*

5.2.3 Resonant Auger Electron Spectroscopy Measurements

The measurements were performed at Synchrotron SOLEIL at GALAXIES beamline. The samples were mounted on a standard omicron-type stainless steel plate (18 mm x 15 mm) using conducting carbon tape to glue the sample on top of the plate. We added this carbon tape also on the sides (Figure 5.3), so that the tape touched both plate and sample. This procedure was performed to minimize sample charging, typical for organic semiconductors samples.

The resonant Sulfur $KL_{2,3}L_{2,3}$ Auger electron spectra were recorded as a function of photon energy using the HAXPES spectrometer. We tuned the photon energy with 0.1 eV step from 2468.0 eV to 2485.0 eV. The electron kinetic energy window used for the experiments was 2097.0 eV to 2125.0 eV. For each photon energy, a RAS spectrum was measured at different non-overlapping points across the sample. The sample was constantly moved during measurements. This scan procedure was applied to avoid radiation damage. We plotted the spectra in the form of two-dimensional (2D) maps, which highlights the qualitative difference in the behavior of the spectral lines. We performed the measurements at two different angles of the photon beam incidence with respect to the sample surface. The measurements at the 10° angle is further

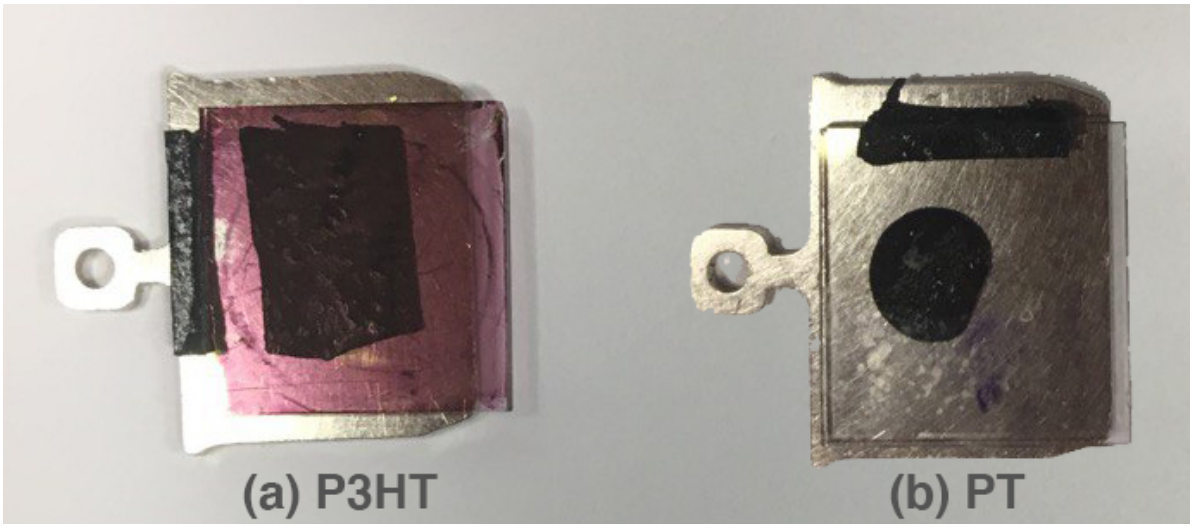

Figure 5.3: *Photography of the two samples used in this work. The samples were glued in a stainless steel plate with conducting carbon tape. A small piece of the same carbon tape was glued around the samples in a way to contact both the films and the plate. This procedure was done to avoid sample charging.*

considered as grazing incidence and the 70° angle represents the conditions of normal incidence.

The spectra were collected with a pass energy of 200 eV. The slits of the beamline monochromator were set to 400 μm yielding a total resolution of 0.31 eV. Both the pass energy and the slits were kept fixed during all measurements. We calibrated the kinetic energy scale through the known Au $4f_{7/2}$ photoelectron line (E_B = 84.0 eV) [186] measured with the same experimental parameters. The photon energy was calibrated using the absorption spectrum measured by Arantes *et. al.* [59] as the reference. The resonant Auger spectra were fitted by multiple Voigt profiles using the SPANCF macro package. [100]

5.3 Results and Discussion

The resonant Sulfur $KL_{2,3}L_{2,3}$ Auger 2D maps for PT and P3HT thin-film polymers measured at grazing incidence and at normal incidence are shown in Figures 5.4 and 5.5. In detail, the 2D maps present the Auger electrons' kinetic energy as a function of the photon energy. The peak intensity is represented by the color scale. The kinetic energy of the normal Auger lines equals 2111 eV and is independent of the photon energy. This behavior is observed at the photon energies from around 2474 eV and above.

For photon energies below 2474 eV, we observe the dispersive behavior of the electron kinetic

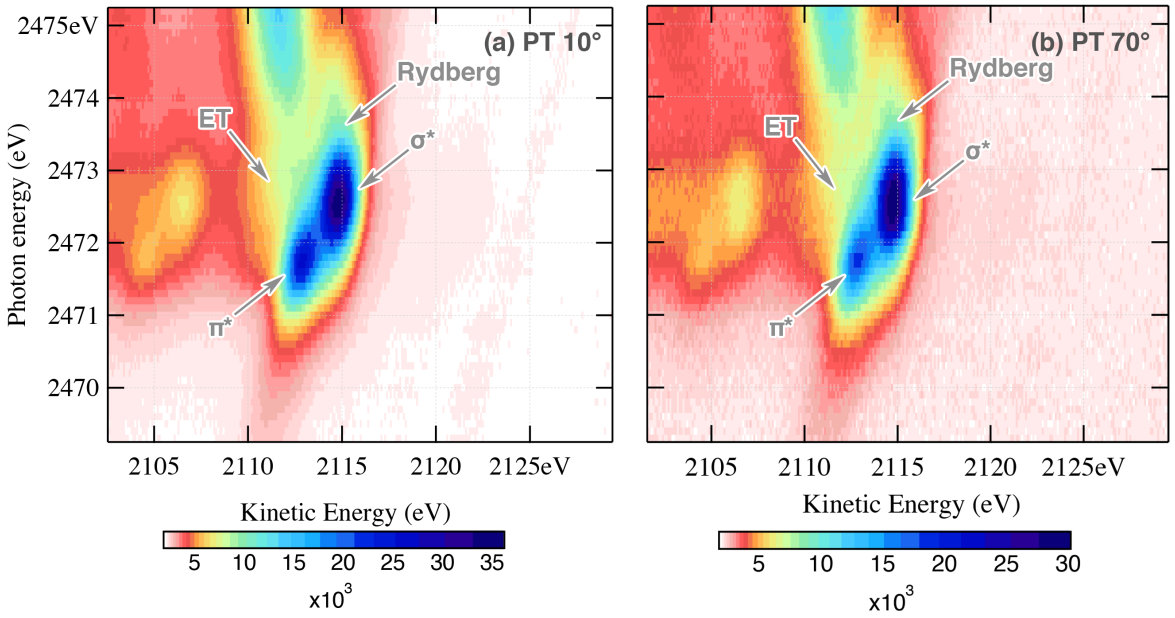

Figure 5.4: *Resonant KLL Auger two-dimensional maps at sulfur 1s for PT. Left: for grazing incidence. Right: for normal incidence. Similar intensities for π^* and σ^* resonances in both maps.*

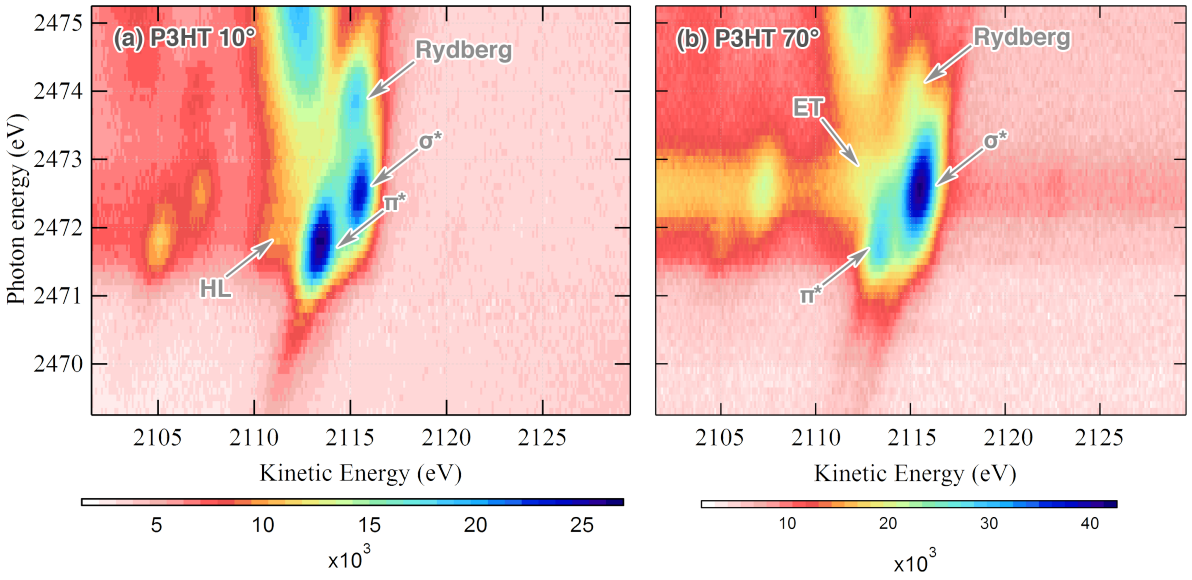

Figure 5.5: *Resonant KLL Auger two-dimensional maps at sulfur 1s for P3HT. Left: grazing incidence. Right: normal incidence. The intensity of σ^* resonance is stronger than π^* resonance for normal incidence measurement.*

energy with the photon energy, characteristic of the spectator Auger decay channel. The features at photon energy around 2472 eV, at kinetic energy around 2105 eV and 2112 eV, correspond to, respectively, the $^1S_0$ and $^1D_2$ configurations of the $2p^{-2}V$ final state, where V is the valence orbital populated by the spectator electron. The two main features labelled in each map as π^* and σ^* correspond to the promotion of the S 1s electron to the π^* (LUMO) orbital and to

the σ^* (LUMO+1) orbital and decay to the $2p^{-2}\pi^*$ and $2p^{-2}\sigma^*$ final states, respectively. So, the excitation energy of the core-excited states is 2471.7 eV for $1s^{-1}\pi^*$ state and 2472.6 eV for $1s^{-1}\sigma^*$ state, whereas the Auger electron kinetic energy for the final states are 2112 eV for $2p^{-2}\pi^*$ state and 2115 eV for $2p^{-2}\sigma^*$ state.

For the case of electron delocalizing from the LUMO or (LUMO+1), one can expect an additional contribution in the Auger spectrum at the kinetic energy of 2111 eV. This feature is labelled in Figures 5.4 and 5.5 as ET (electron transfer). Note that the kinetic energy of the additional contribution related to the electron delocalization is the same as of the normal Auger line since the electron transfer causes the quenching of the resonant channels leading to a final state configuration equivalent to the normal Auger decay. Another feature is observed in P3HT measured at grazing incidence (Figure 5.5, left panel), around the photon energy of 2471.9 eV and the kinetic energy of 2110 eV. This feature, labelled as HL, appears at the photon energy close to the resonant excitation of the π^*LUMO orbital and might be related to shake-up of an electron from HOMO to π^*LUMO.

We start our discussion by the angular dependence of relative in intensities of the two main resonant features. If the investigated material has a regular structure, with the molecules ordered with respect to the surface of the material, we should observe differences in intensity between the $1s^{-1}\pi^*$ and the $1s^{-1}\sigma^*$ core-excited states. This difference in intensity is a result of the different overlap between the polarization vector for the electric field $\vec{E}$, which is perpendicular to the propagation direction of the incident radiation beam and the orientation of the antibonding orbitals π^* and σ^*. Therefore, the greater the overlap between $\vec{E}$ and the antibonding orbital, the greater the intensity at the corresponding resonance. The intensities of both resonances on PT 2D maps (Figure 5.4) did not reveal a strong angular dependence. In contrast, a strong angular dependence has been observed for P3HT samples (Figure 5.5), suggesting that P3HT can be considered better organized compared to PT. P3HT is known to undergo self-organization with formation of lamella structure of 2D sheets formed by interchain stacking [187]. There are two main possible orientations of the polymeric chains of P3HT with respect to the surface of the substrate (see Figure 5.6): edge-on and face-on [188]. Edge-on orientation is characterized by the lamella sheets placed perpendicular to the substrate, whereas in face-on orientation the lamella sheets are parallel to the substrate.

The angular dependence observed in our measurements on P3HT suggests the dominance of

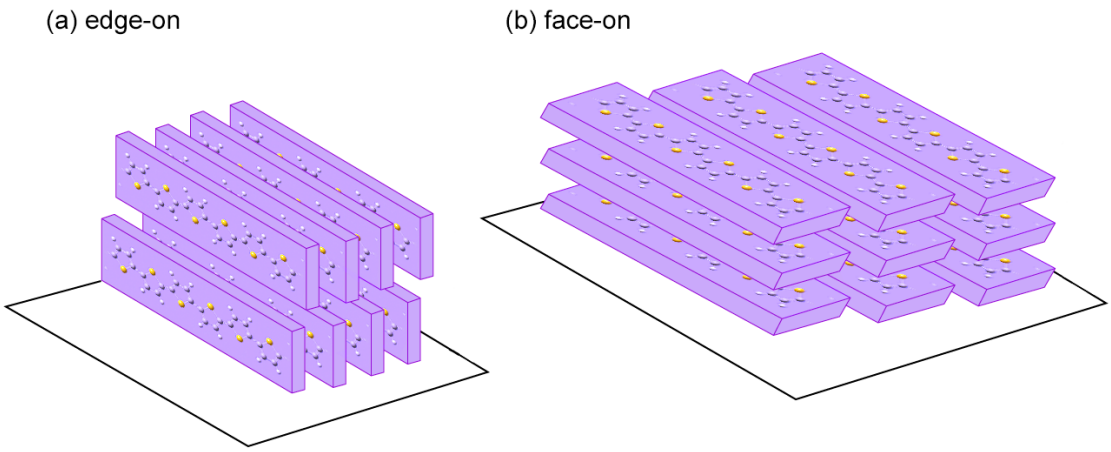

Figure 5.6: *Pictorial representation of the two main possible orientations for the P3HT thin-films: (a) edge-on orientation, where the polymer chains are placed perpendicular to the substrate and (b) face-on orientation, where the chains are placed parallel to the substrate surface.*

the face-on orientation. In our experiment the directions of the photon beam and of the light polarization vector $\vec{E}$ are fixed in the horizontal plane. For angle-dependence studies we can rotate the sample around the vertical axis. Under the grazing incidence conditions polarization is perpendicular to the sample surface, whereas for the normal incidence polarization is parallel to the substrate (see Figure 5.7). If we assume a face-on orientation of P3HT as shown in Figure 5.6b, then grazing incidence geometry provides favourable conditions for excitation of the π^* orbital, whereas normal incidence geometry should provide dominant excitation of the σ^* orbital. This is exactly what we observe in our P3HT 2D maps (Figure 5.5). The relative intensity of the π^* resonance is higher for the grazing incidence geometry, and the intensity of the σ^* resonance is significantly enhanced for the normal incidence geometry.

The preferential orientation depends on the conditions of the sample preparation and on the regioregularity of the P3HT [187]. According to our preparation method, we can expect face-on orientation of our P3HT films. In previous works, X-ray Diffraction (XRD) was employed for a systematic study of the orientation of the P3HT conjugate plane in films prepared by spin coating of P3HT in chloroform solutions as a function of the rotational spin-coating frequency and the solution concentration [189]. According to this study, the film preparation using the same

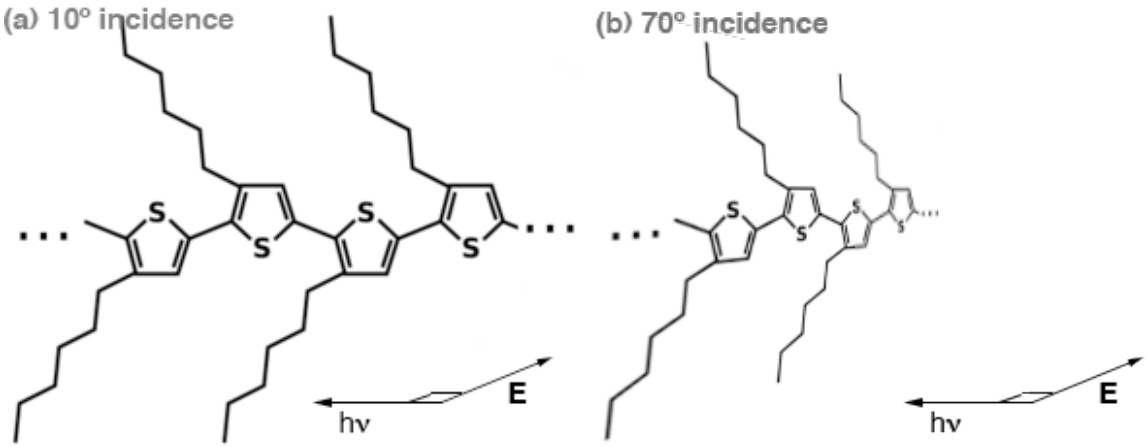

Figure 5.7: *Pictorial representation of the measurements at different angles of photon incidence. We represented the sample by the stick structure of the P3HT polymer. 5.7a: 10° of the photon beam incidence to the sample (grazing incidence) and 5.7b: 70° of the photon beam incidence to the sample (conditions of the normal incidence).*

experimental conditions as ours correspond to formation of face-on (plane-on) orientation. In a second study, P3HT samples prepared by spin-coating 0.5 wt% in chloroform, were characterized by grazing incidence XRD [190]. In this configuration XRD is mostly sensitive to crystallographic planes non-parallel to the sample surface. The corresponding XRD spectrum confirms face-on orientation in the as-spun sample. We characterized the P3HT sample by XRD using Cu Kα source (about 8 keV photon energy) in the symmetric $\theta/2\theta$ geometry scanning the 2θ angle in the range from 5° to 90°. Our characterization agrees with the previous XRD studies on P3HT films prepared using a protocol similar to ours: the dominance of the face-on structure, evidenced by the features related to the interchain $\pi - \pi$ stacking.

Back to the resonant S $KL_{2,3}L_{2,3}$ Auger electron spectra, we analysed each individual spectrum from the maps. In Figure 5.8, we show a set of spectra selected from the PT 2D map recorded at grazing incidence as an example. We observe an evolution of the resonant Auger spectra with the photon energy. At hν = 2471.7 eV the spectrum is dominated by the π^*(LUMO) resonance (Figure 5.8a), at higher photon energies the contribution of the σ^*(LUMO+1) resonance increases and becomes dominant at hν = 2472.6 eV (Figure 5.8c). A small peak at the kinetic energy of 2111 eV, labelled as ET and attributed to electron transfer to a neighbor molecule, can be observed in all the panels. Its contribution enhances significantly at the photon energies above the σ^* resonance (Figure 5.8d). As the photon energy approaches 2474 eV, the

ET peak merges into a normal Auger line (Figure 5.8f). Similar analysis was performed for all the measurements. It is important to point out that the resonant Auger spectrum consists of three multiplet lines corresponding to the ^1S, ^1D, and ^3P terms of $2p^2$ final state. So, the peaks labelled as $^1S_0$ correspond to the ^{1}S multiplet lines.

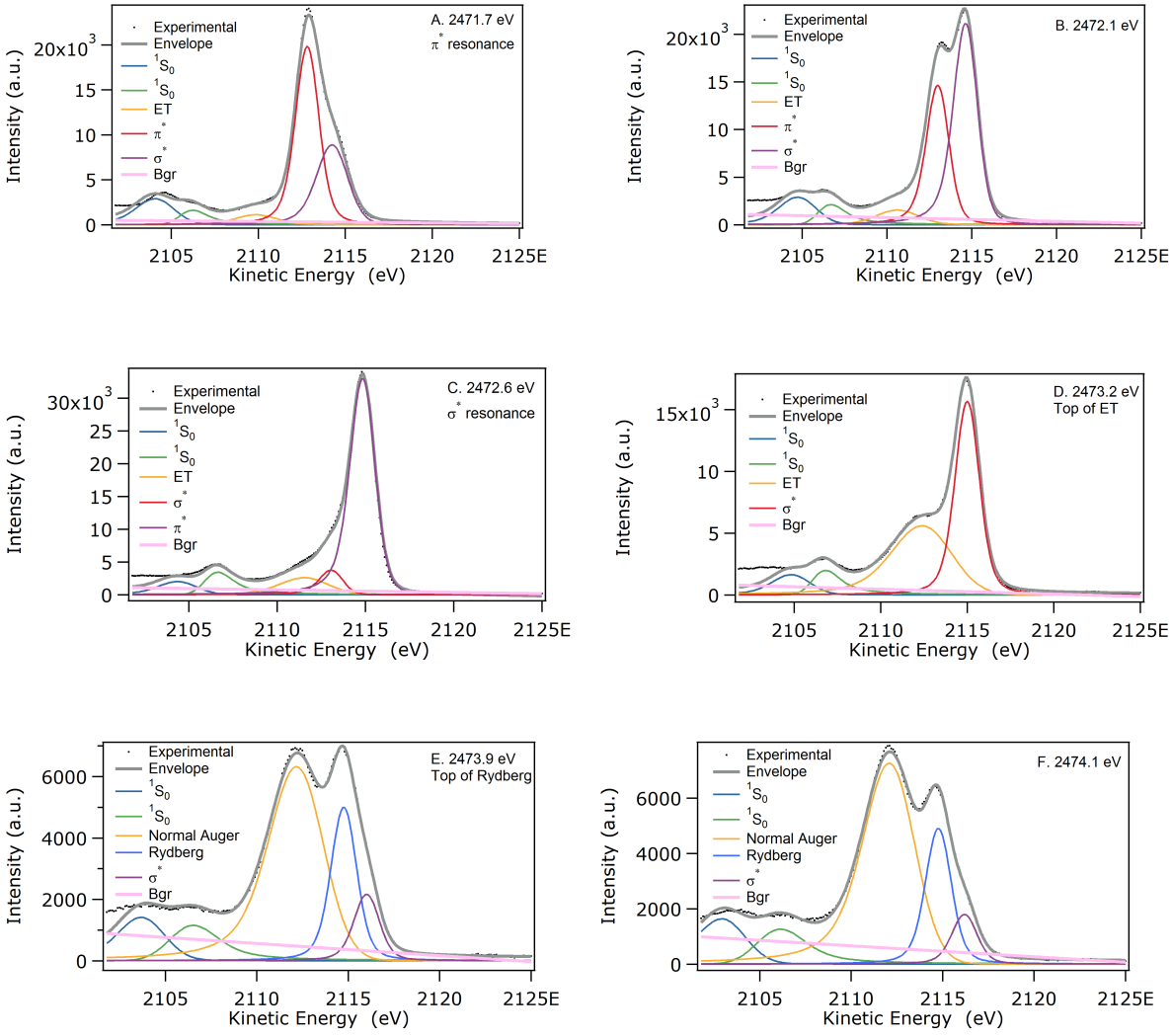

Figure 5.8: *Fitted resonant KLL Auger spectra at sulfur 1s for PT measured at grazing incidence.*

Results of the fitting allowed us to plot the peak areas as a function of the photon energy (Figure 5.9). Remarkably, in PT (Figures 5.9a and 5.9b) the area of the ET peak (yellow symbols) becomes substantial only at the photon energies close to the resonant excitation of σ^* orbital ($h\nu = 2472.6$ eV). It reaches a local maximum around $h\nu = 2473.2$ eV, and then shows a further enhancement above $h\nu = 2474$ eV, corresponding to the onset of the normal Auger line. In P3HT (Figure 5.9c) the ET peak area is substantial already at the photon energies around the resonant excitation of the π^* orbital ($h\nu = 2471.7$ eV). In normal incidence measurements (P3HT 70°) the ET peak area exhibits a local maximum around $h\nu = 2472.8$ eV, at the photon energy slightly above the σ^* resonant excitation. Further increase of the photon energy leads to the drop of the ET peak area followed by enhancement related to the onset of the normal Auger line. Our observations indicate that the appearance of the ET peak related to electron transfer is correlated with the resonant excitation of the σ^* orbital.

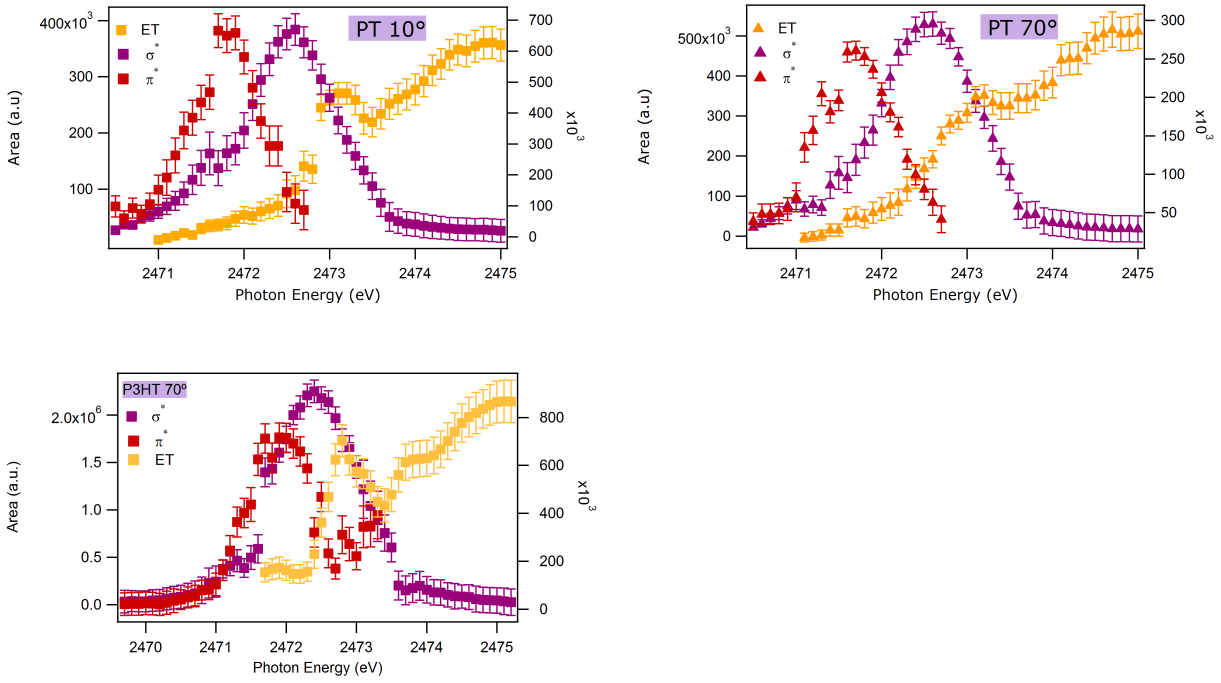

Figure 5.9: *Areas from π^*, σ^* and ET as a function of the photon energy for PT (5.9a: grazing incidence and 5.9b: normal incidence) and P3HT (5.9c: normal incidence).*

Previous studies employing RAS to investigate ultrafast electron dynamics in PT thin films on ITO suggested the interchain electron transfer pathway [59]. This interpretation is based on the former work by Ikeura-Sekiguchi and Sekiguchi [181], where resonant Auger spectroscopy measurements were performed to identify closely lying states, not resolved by XAS on PT pow-

dered samples. Although this work did not directly discuss electron dynamics, an important observation can be made: RAS spectra did not indicate the presence of electron transfer dynamics. In contrast, Arantes *et. al.* [59] observed electron transfer dynamics on the PT films. Considering that interchain interactions should be weak in powders since they are amorphous, whereas in a thin-film such interactions should be present, the available pathway for electron transfer should be between the polymer layers. However, in such studies it was not possible to obtain information from which orbital the electron delocalizes. We observed from our analysis on PT 2D maps that the maximum of the ET peak has energy close to the σ^* resonance, suggesting that the transferred electron delocalizes from the σ^* (LUMO+1) molecular orbital. In the P3HT films, which exhibits a better organized structure, an additional mechanism of electron delocalization in the $\pi - \pi$ stacking direction becomes possible. This may be the reason for an observable ET peak around the π^* resonance.

In addition, the curve fitting analysis enabled us to obtain the charge transfer rate, τ_{CT}, as a function of photon energy applying the Equation 5.6. In detail, I_{res} is the area of the σ^* resonant Auger line and I_{Auger} is the area of the labelled ET peak in the resonant Auger spectrum. The natural lifetime of the S 1s core hole $\tau_{\mathrm{CH}} = 1.27$ fs [191]. We obtain similar curves for PT and P3HT measurements (Figure 5.10). The electron delocalization time varies on the order of 1 fs to 3 fs at the photon energies close to the σ^* resonant excitation. The obtained values are comparable to the S 1s core hole lifetime τ_{CH}. The τ_{CT} describes the probability of an electron to delocalize from the initially excited orbital to where the excited electron is being transferred to. Therefore, we can assume that this parameter should depend on 1) whether the electron is excited to the σ^* or π^* orbital and 2) whether the delocalization occurs along the polymer chain or through the $\pi - \pi$ stacks. From our analysis, we suggest the σ^* (LUMO+1) as the orbital from which the spectator electron delocalizes, transferring to a neighbor system. Following the selection rules, one can assume that the electron transfers from σ^* to a π^* orbital. However, theoretical calculations must be performed to the obtain further information on which π^* orbital the electron delocalizes, along or at the next polymer chain.

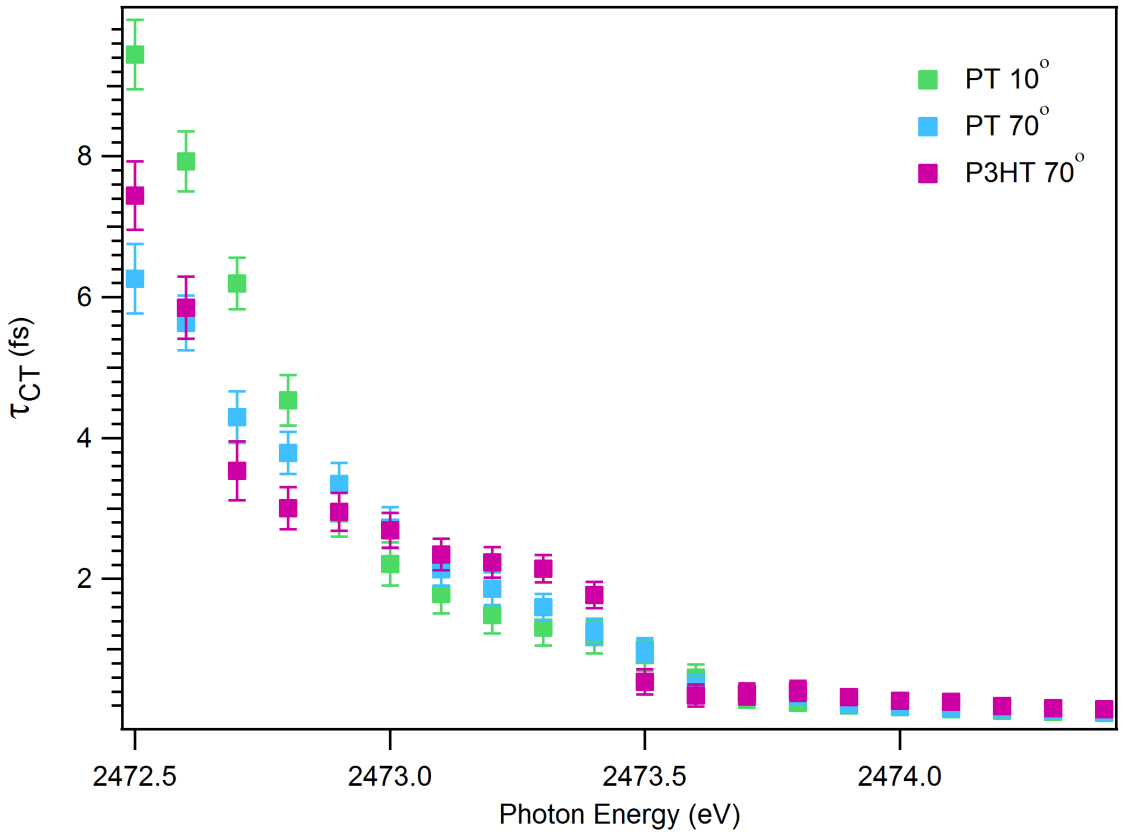

Figure 5.10: *Electron transfer rate in fs as a function of the photon energy for PT measured at 10° and 70° (green and blue squares, respectively) of photon incidence and for P3HT measured at 70° of photon incidence (pink squares). The error bars are derived from the standard deviation of the spectral curve fitting.*

5.4 Conclusion

The access to the state-of-the-art in terms of the photon energy resolution on the GALAXIES beamline enabled us to conduct resonant Auger electron spectroscopy in the tender X-ray photon energy domain under the so-called Raman conditions, where the total experimental resolution is narrower than the natural lifetime broadening of the core-excited state. Such conditions allowed us to study ultrafast electron dynamics using the core-hole clock spectroscopy, CHCS, in which the main idea is to use the lifetime of the core-excited state as a timer to obtain information on the studied system's dynamics. Applying the CHCS, we investigated ultrafast electron dynamics in PT and P3HT thin-films deposited onto ITO substrate using resonant Auger electron spectroscopy, one of the CHCS techniques. The measurements were carried out at two different photon incidence angles to the substrate surface: at 10°, corresponding to the grazing incidence, and at 70°, which stands for the conditions of normal incidence. Our samples

are assumed to be thin-films, which was confirmed by AFM characterization.

We recorded each resonant Sulfur $KL_{2,3}L_{2,3}$ Auger spectrum by tuning the photon energy in small steps from below resonances to above the ionization threshold. The spectra were presented as 2D maps, highlighting the qualitative difference in the spectral lines' behavior. The PT thin-films did not show strong angle dependence whereas the P3HT films exhibits stronger angle dependence, observed by the difference in the intensities of the $1s^{-1}\pi^*$(LUMO) and $1s^{-1}\sigma^*$(LUMO+1) states for grazing and normal incident measurements. This dependence suggests a well-organized P3HT film with its lamella sheets placed at face-on orientation. Since the P3HT film orientation strongly depends on the preparation method, we performed XRD measurements to assure the face-on orientation in our samples. The results agree with the literature for P3HT thin-films prepared in similar conditions as ours, confirming the face-on orientation for our P3HT thin-films.

From the PT maps measured at both incidence angles to the sample surface and from P3HT maps measured at normal incidence, we observed an additional contribution appearing at the kinetic energy of the normal Auger lines. This feature is related to the electron delocalization since the final state configuration has two-holes similar to the normal Auger decay final state' configuration. We performed curve fitting analysis of the individual spectra from the 2D maps, which enabled us to plot the peak areas related to the states where the spectator Auger electron is at π^* and σ^* molecular orbitals as well as the peak areas of the feature related to the electron transfer as a function of the photon energy. We observed the maximum of the electron transfer peak close in energy to the top of σ^* resonance for the PT measurements (at 10° and 70° of the photon beam incidence with respect to the sample) and for the P3HT measurements at 70° of photon incidence. This result suggests the electron being transferred from the σ^* (LUMO+1) orbital. In P3HT, our analysis showed an indication of the electron being transferred also from the π^* (LUMO), suggesting this additional transfer pathway.

We obtained charge transfer rates, τ_{CT}, by the ratio of the spectator (σ^*) and electron transfer peak areas multiplied by the S 1s core-hole lifetime (τ_{CH}). We plotted the obtained values as a function of the photon energy. We obtained similar curves for both PT and P3HT analysis. We observed values comparable to τ_{CH} at photon energies close to the σ^* resonant excitation. The τ_{CT} is interpreted as the probability of the electron to delocalize from the initially excited orbital. Therefore, one can have two considerations. First, which molecular orbital the core-electron is promoted to. Second, whether this electron delocalizes along the polymer chain or through the $\pi - \pi$ stacks between chains. From our experimental analysis, one can suggest the electron transferring from the σ^* (LUMO+1) orbital. However, theoretical support is necessary to obtain determine in which direction the transferred electron delocalizes.

Chapter

6 Conclusions and Outlooks

In this thesis, we have demonstrated the potential of HAXPES end-station installed at the GALAXIES beamline of the SOLEIL synchrotron facility. This set-up enabled us to perform photoexcitation and photoionization experiments under state-of-the art conditions in terms of photon and electron energy resolution. Such conditions allowed us to carry out electron spectroscopy measurements aiming to study complex phenomena which could not be performed in hard X-rays few years ago.

We addressed our first investigations to atomic systems in gas phase. The advance in brilliance of the synchrotron sources combined with the instrumental development of the spectrometers enabled experimental investigations of quite small cross-section processes, specially in tender to hard X-ray regime. The access to these state-of-the-art experimental technologies enabled us to perform photoionization of shells far above their thresholds in rare-gas atoms. We measured the ratio of the photoionization cross-section of the spin-orbit doublet components for Argon and Xenon rare-gas atoms. The investigation enabled us to experimentally confirm the predictions that the branching ratio of the spin-orbit components' photoionization cross-section never approaches the statistical value (l+1)/l for a given subshell nl due to relativistic effects. Second, we found that the resonances just below the photoionization threshold couple differently to each spin-orbit doublet component. A third result is related to the interchannel coupling effects on the intensity of the spin-orbit doublet branching ratio in a wide energy range of about two keV.

In the photoionization process, the interchannel coupling is a manner to describe the electron correlation in the final state. The interchannel coupling can significantly influence the photoionization cross section or the angular distribution of the emitted photoelectrons, in particular, close to deeper ionization thresholds. The study of the interchannel coupling between the continua of two spin-orbit split levels explicitly probes the manifestations of relativistic effects in the photoionization process, since the effect owes to relativistic interactions. This phenomenon

has been studied for several atoms. However, such studies are restricted to the channels of the spin-orbit doublet. Recently calculations of the photoionization cross section of Xe 5p, 5s, 4d, 4p, and 4s levels in the vicinity of the Xe 3d thresholds were performed in collaboration with Prof. Dr. Steven Manson. The predictions showed that interchannel coupling also significantly affects these outer shell cross sections via interchannel coupling. We intend to perform further experimental investigations on interchannel coupling at the Xe 5p, 5s, 4d, and 4s cross sections to compare them with the predicted results. We expect to gain valuable information on the physical processes that must be included by theory to correctly represent relativistic interactions in the final continuum state of an atomic photoionization process.

In the second part of our results, we studied organic aromatic molecules, thiophene and thiazole, in gas phase. In this work, we employed resonant Auger spectroscopy as a tool to probe the conjugation effects in these molecules. We observed the effect of inversion in the energy order of deep core-excited states. The absence of such inversion in thiolane, the saturated analog of thiophene, suggested that the conjugation effects play a role in the observed behavior. High-level quantum chemistry calculations and NBO calculations were carried out to interpret the experimental observations. We have shown that the effect of the orbital order inversion is specific to core-excitation in conjugated molecules since it emerges from the interaction between the lone pair of the heteroatom and the $\pi-$system in the aromatic ring. The discovered phenomenon has been also recently observed in our studies on polythiophene and, thus, is not limited to isolated molecules. This effect is expected to be general for other conjugated heterocycles as well as for larger conjugated systems like polymers undergoing core-excitation and Auger decay. Therefore, we showed that the resonant Auger spectroscopy can be applied in the study of any conjugated system.

In the last part of the results of this thesis, we moved to larger systems: thiophene-based thin-film polymers. In this case, we explored the potential of core-hole clock spectroscopy to understand the electron delocalization in polythiophene (PT) and poly[3-hexylthiophene-2,5-diyl] (P3HT) deposited onto an ITO substrate. We used resonant Auger spectroscopy to monitor delocalization from a core-excited state. The resonant S $KL_{2,3}L_{2,3}$ Auger decay spectra were measured at two different angles of the photon beam incidence with respect to the sample surface and they were presented as two-dimensional maps. A strong angle dependence was observed for P3HT suggesting the face-on organization of the polymer layers, and it was confirmed by X-ray

diffraction characterization. We observe an indication that the electron delocalization in these films is correlated with the resonant excitation to the σ^* orbital. The charge transfer times were determined by quantifying the integrated intensity ratio between spectator Auger and the electron transfer peak contributions from the resonant Auger spectra. The obtained values are comparable to the S 1s core hole lifetime.

For future investigations on polymers, we expect to perform theoretical calculations to have a complete description of the charge transfer mechanisms. Moreover, we expect to perform resonant Auger electron spectroscopy on powdered polythiophene. This system was already investigated few years ago by other research group and the electron transfer was not observed [181]. However, only several spectra at selected photon energies could be measured. We can perform the resonant Auger electron spectroscopy on powdered polythiophene with better resolution and plot the 2D maps. Therefore, we expect to obtain more information on this system, compared to the earlier studies which suffered from to experimental limitations. We expect to combine the results from these future measurements with our present results to gain further information concerning the electron delocalization pathways in polymers. Finally, an interesting observation which deserves more detailed investigation is the PCI effect (a brief description of this effect can be found in Subsection 2.2.2) in polymers (see Figure 6.1). To the best of our knowledge, this effect was never observed before in polymer systems.

Besides the main subject of this thesis, I also had an active participation in other projects in collaboration with Prof. Dr. Yoshiro Azuma (from Sophia University in Tokyo, Japan) using soft X-rays. We recently investigated the recapture of photoelectrons induced by post-collision interaction following near-threshold Ar 2p photoionization. [192]. We also studied the configuration interaction between $3p^{-1}$ and $3p^{-2}nl$ states in the high-resolution Kr photoelectron spectrum in the region close to the 3p ionization threshold [193].

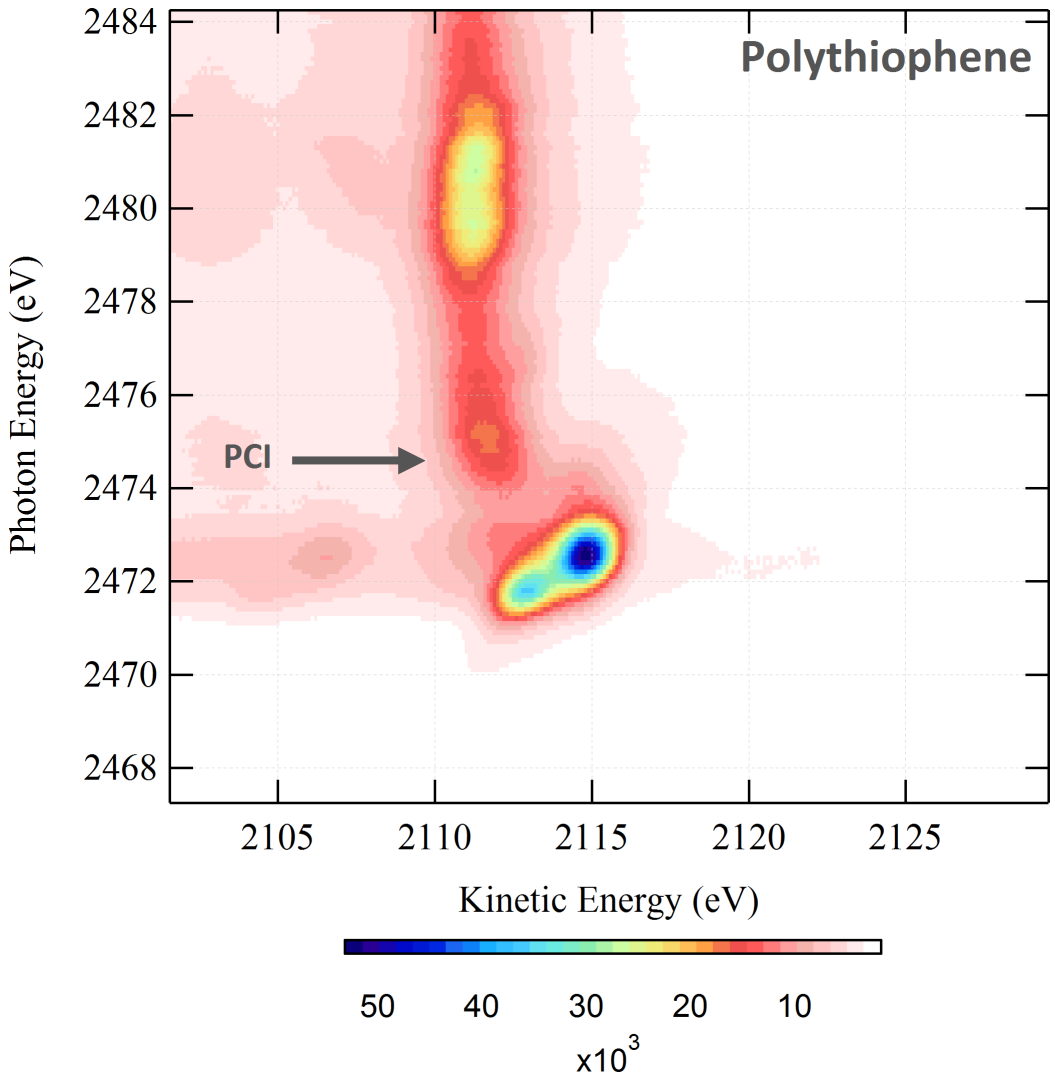

Figure 6.1: *Resonant Sulfur $KL_{2,3}L_{2,3}$ Auger 2D map for polythiophene thin film on an ITO substrate measured at 10° of the photon beam incidence with respect to the sample. The PCI signature, characterized by the shift of the Auger electron to higher kinetic energies close to the ionization threshold, is highlighted on the map.*

Bibliography

References for Chapter 1: Introduction

[1] Maria Novella Piancastelli et al. "Hard x-ray spectroscopy and dynamics of isolated atoms and molecules: a review." In: *Reports on progress in physics. Physical Society (Great Britain)* 83.1 (2019), p. 016401. ISSN: 0034-4885. DOI: 10.1088/1361-6633/ab5516 *Cited on pages 3, 29, 44.*

[2] Heinrich Hertz. "Ueber einen Einfluss des ultravioletten Lichtes auf die electrische Entladung". In: *Annalen der Physik* 267.8 (1887), pp. 983–1000 *Cited on page 4.*

[3] A Einstein. "Generation and conversion of light with regard to a heuristic point of view". In: *Annalen Der Physik* 17.6 (1905), pp. 132–148 *Cited on page 4.*

[4] K. Siegbahn et al. "ESCA Applied to Free Molecules". In: (1969) *Cited on page 5.*

[5] James AR Samson and JL Gardner. "Branching ratios in photoelectron spectroscopy". In: *JOSA* 62.7 (1972), pp. 856–858 *Cited on page 7.*

[6] James A.R Samson. "Photoionization of atoms and molecules". In: *Physics Reports* 28.4 (1976), pp. 303–354. ISSN: 0370-1573. DOI: 10.1016/0370-15737690012-0 *Cited on pages 7, 50.*

[7] WALTER BAMBYNEK et al. "X-Ray Fluorescence Yields, Auger, and Coster-Kronig Transition Probabilities". In: *Rev. Mod. Phys.* 44 (4 Oct. 1972), pp. 716–813. DOI: 10.1103/RevModPhys.44.716 *Cited on page 9.*

[8] William Henry Bragg and William Lawrence Bragg. "The reflection of X-rays by crystals". In: *Proceedings of the Royal Society of London. Series A, Containing Papers of a Mathematical and Physical Character* 88.605 (1913), pp. 428–438 *Cited on page 11.*

[9] Manne Siegbahn. *Spektroskopie der röntgenstrahlen*. Springer-Verlag, 2013 *Cited on page 11.*

[10] Wilhelm Conrad Röntgen. "Abdruck der 1. und 2. Originalmitteilung von 1895, uber eine neue art von strahlen, und der 3. Mitteilung von 1897, weitere beobachtungen uber die eigenschaften der x-strahlen". In: *Ann. Phys. Chem.* 64 (1898), pp. 1–37 *Cited on page 11.*

[11] AE Lindh and O Lundquist. "Die Struktur der KSS,-Linie des Schwefels". In: *Ark. Mat. Astr. Fysi* 18.14 (1924), pp. 3–11 *Cited on page 11.*

[12] Alfred Faessler and Margot Goehring. "Röntgenspektrum und Bindungszustand". In: *Naturwissenschaften* 39.8 (1952), pp. 169–177 *Cited on page 11.*

[13] Roman L Barinski and Vladimir Dmitrievich Nefedov. "Rontgenspektroskopische Bestimmung der Atomladungen in molekulen". In: (1969) *Cited on page 11.*

[14] Rolf Manne. "Chemical shifts in x-ray emission". In: *Inner-Shell and X-Ray Physics of Atoms and Solids*. Springer, 1981, pp. 699–706 *Cited on page 11.*

[15] Armin Meisel, Gunter Leonhardt, and Rüdiger Szargan. "X-ray spectra and chemical binding". In: *Springer Series in Chemical Physics* 37 (1989), pp. VIII–458 *Cited on page 11.*

[16] Lise Meitner. "Über die entstehung der β-strahl-spektren radioaktiver substanzen". In: *Zeitschrift für Physik* 9.1 (1922), pp. 131–144 *Cited on page 11.*

[17] P Auger. "The compound photoelectric effect". In: *J. Phys. Radium* 6.6 (1925), pp. 205–208 *Cited on page 11.*

[18] Chandrasekhara Venkata Raman. "A new radiation". In: *Indian Journal of physics* 2 (1928), pp. 387–398 *Cited on page 11.*

[19] F Kh Gel'Mukhanov, LN Mazalov, and AV Kondratenko. "A theory of vibrational structure in the X-ray spectra of molecules". In: *Chemical Physics Letters* 46.1 (1977), pp. 133–137 *Cited on pages 12, 13.*

[20] Faris Gel'mukhanov and Hans Ågren. "Resonant X-ray Raman scattering". In: *Physics Reports* 312.3-6 (1999), pp. 87–330 *Cited on pages 12, 17, 19.*

[21] Hendrik A Kramers and Werner Heisenberg. "Über die streuung von strahlung durch atome". In: *Zeitschrift für Physik* 31.1 (1925), pp. 681–708 *Cited on pages 12, 13.*

[22] Victor Frederick Weisskopf and Eugene Paul Wigner. "Calculation of the natural brightness of spectral lines on the basis of Dirac's theory". In: *Z. Phys.* 63 (1930), pp. 54–73 *Cited on page 12.*

[23] Viktor Weisskopf. "Zur theorie der resonanzfluoreszenz". In: *Annalen der Physik* 401.1 (1931), pp. 23–66 *Cited on page 12.*

[24] George S Brown et al. "Observation of the Auger Resonant Raman Effect". In: *Physical Review Letters* 45.24 (1980), pp. 1937–1940. ISSN: 0031-9007. DOI: 10.1103/physrevlett.45.1937 *Cited on pages 12, 16.*

[25] M.N. Piancastelli. "Auger resonant Raman studies of atoms and molecules". In: *Journal of Electron Spectroscopy and Related Phenomena* 107.1 (2000), pp. 1–26. ISSN: 0368-2048. DOI: https://doi.org/10.1016/S0368-2048(99)00099-7 *Cited on page 16.*

[26] G Bradley Armen et al. "Threshold excitation of short-lived atomic inner-shell hole states with synchrotron radiation". In: *Physical review letters* 54.11 (1985), p. 1142 *Cited on page 16.*

[27] A. Kivimäki et al. "Subnatural linewidths in the Kr $M_5N_{2,3}N_{2,3}$ and Xe $N_5O_{2,3}O_{2,3}$ resonant Auger spectra". In: *Phys. Rev. Lett.* 71 (26 Dec. 1993), pp. 4307–4310. DOI: 10.1103/PhysRevLett.71.4307 *Cited on page 16.*

[28] A Baev et al. "Picturing molecular femtosecond processes through an ultra-fast controllable X-ray shutter". In: *Chemical physics* 289.1 (2003), pp. 51–56 *Cited on page 17.*

[29] P Morin and I Nenner. "Atomic autoionization following very fast dissociation of core-excited HBr". In: *Physical review letters* 56.18 (1986), p. 1913 *Cited on page 17.*

[30] H Aksela et al. "Decay channels of core-excited HCl". In: *Physical Review A* 41.11 (1990), p. 6000 *Cited on page 18.*

[31] H Aksela et al. "Decay channels of core-excited H 2 S studied by synchrotron-radiation-excited photoelectron spectroscopy". In: *Physical Review A* 45.11 (1992), p. 7948 *Cited on page 18.*

[32] SJ Schaphorst et al. “Evidence for atomic features in the decay of resonantly excited molecular oxygen”. In: *Chemical physics letters* 213.3-4 (1993), pp. 315–320 *Cited on page 18.*

[33] P Saek et al. “Dynamical suppression of atomic peaks in resonant dissociative photoemission”. In: *Chemical physics letters* 343.3-4 (2001), pp. 332–338 *Cited on page 18.*

[34] I Hjelte et al. “Evidence for ultra-fast dissociation of molecular water from resonant Auger spectroscopy”. In: *Chemical physics letters* 334.1-3 (2001), pp. 151–158 *Cited on page 18.*

[35] Ingela Hjelte et al. “Evidence of ultra-fast dissociation in ammonia observed by resonant Auger electron spectroscopy”. In: *Chemical physics letters* 370.5-6 (2003), pp. 781–788 *Cited on page 18.*

[36] K Le Guen et al. “H 2 S ultrafast dissociation probed by energy-selected resonant Auger electron–ion coincidence measurements”. In: *The Journal of chemical physics* 127.11 (2007), p. 114315 *Cited on page 18.*

[37] Marc Simon et al. “Femtosecond nuclear motion of HCl probed by resonant x-ray Raman scattering in the Cl 1 s region”. In: *Physical Review A* 73.2 (2006), p. 020706 *Cited on page 19.*

[38] T Marchenko et al. “Resonant inelastic x-ray scattering at the limit of subfemtosecond natural lifetime”. In: *The Journal of chemical physics* 134.14 (2011), p. 144308 *Cited on page 19.*

[39] L El Khoury et al. “Resonant inelastic x-ray scattering of methyl chloride at the chlorine K edge”. In: *The Journal of chemical physics* 136.2 (2012), p. 024319 *Cited on page 19.*

[40] Oksana Travnikova et al. “Hard-x-ray-induced multistep ultrafast dissociation”. In: *Physical review letters* 116.21 (2016), p. 213001 *Cited on page 19.*

[41] MF Kling et al. “Control of electron localization in molecular dissociation”. In: *Science* 312.5771 (2006), pp. 246–248 *Cited on pages 19, 88.*

[42] Giuseppe Sansone et al. “Electron localization following attosecond molecular photoionization”. In: *Nature* 465.7299 (2010), pp. 763–766 *Cited on pages 19, 88.*

[43] A. Föhlisch et al. "Direct observation of electron dynamics in the attosecond domain". In: *Nature* 436.7049 (2005), pp. 373–376. ISSN: 0028-0836. DOI: 10.1038/nature03833 *Cited on pages 19, 20.*

[44] O Björneholm et al. "Determination of time scales for charge-transfer screening in physisorbed molecules". In: *Physical review letters* 68.12 (1992), p. 1892 *Cited on page 19.*

[45] O Björneholm et al. "Femtosecond dissociation of core-excited HCl monitored by frequency detuning". In: *Physical review letters* 79.17 (1997), p. 3150 *Cited on page 19.*

[46] C Keller et al. "Ultrafast charge transfer times of chemisorbed species from Auger resonant Raman studies". In: *Physical review letters* 80.8 (1998), p. 1774 *Cited on page 19.*

[47] PA Brühwiler, O Karis, and N Mårtensson. "Charge-transfer dynamics studied using resonant core spectroscopies". In: *Reviews of Modern Physics* 74.3 (2002), p. 703 *Cited on pages 19, 92, 93.*

[48] Dietrich Menzel. "Ultrafast charge transfer at surfaces accessed by core electron spectroscopies". In: *Chem. Soc. Rev.* 37.10 (2008), pp. 2212–2223. ISSN: 0306-0012. DOI: 10.1039/b719546j *Cited on page 19.*

[49] T Marchenko et al. "Electron dynamics in the core-excited CS 2 molecule revealed through resonant inelastic x-ray scattering spectroscopy". In: *Physical Review X* 5.3 (2015), p. 031021 *Cited on page 20.*

[50] T Marchenko et al. "Potential energy surface reconstruction and lifetime determination of molecular double-core-hole states in the hard x-ray regime". In: *Physical review letters* 119.13 (2017), p. 133001 *Cited on page 20.*

[51] Emad F Aziz et al. "Interaction between liquid water and hydroxide revealed by core-hole de-excitation". In: *Nature* 455.7209 (2008), pp. 89–91 *Cited on page 20.*

[52] Emad F Aziz et al. "Probing the electronic structure of the hemoglobin active center in physiological solutions". In: *Physical review letters* 102.6 (2009), p. 068103 *Cited on page 20.*

[53] Wandared Pokapanich et al. “Auger electron spectroscopy as a probe of the solution of aqueous ions”. In: *Journal of the American Chemical Society* 131.21 (2009), pp. 7264–7271 *Cited on page 20.*

[54] Emad F Aziz et al. “Charge transfer to solvent identified using dark channel fluorescence-yield L-edge spectroscopy”. In: *Nature Chemistry* 2.10 (2010), pp. 853–857 *Cited on page 20.*

[55] Joachim Schnadt et al. “Experimental evidence for sub-3-fs charge transfer from an aromatic adsorbate to a semiconductor”. In: *Nature* 418.6898 (2002), pp. 620–623 *Cited on page 20.*

[56] Hiromi Ikeura-Sekiguchi and Tetsuhiro Sekiguchi. “Attosecond electron delocalization in the conduction band through the phosphate backbone of genomic DNA”. In: *Physical review letters* 99.22 (2007), p. 228102 *Cited on pages 20, 21.*

[57] Hiromi Ikeura-Sekiguchi and Tetsuhiro Sekiguchi. “Femto-and attosecond electron dynamics in 5-Guanosine monophosphate interface as probed by resonant Auger spectroscopy”. In: *Surface and Interface Analysis* 42.6-7 (2010), pp. 1085–1088 *Cited on page 20.*

[58] Wallace CH Choy, Wai Kin Chan, and Yuping Yuan. “Recent advances in transition metal complexes and light-management engineering in organic optoelectronic devices”. In: *Advanced Materials* 26.31 (2014), pp. 5368–5399 *Cited on page 21.*

[59] C Arantes et al. “Femtosecond electron delocalization in poly (thiophene) probed by resonant auger spectroscopy”. In: *The Journal of Physical Chemistry C* 117.16 (2013), pp. 8208–8213 *Cited on pages 21, 89, 96, 102, 103.*

[60] Hiromi Ikeura-Sekiguchi and Tetsuhiro Sekiguchi. “Molecular ordering effect of regioregular poly (3-hexylthiophene) using sulfur K-edge X-ray absorption spectroscopy”. In: *Japanese Journal of Applied Physics* 53.2S (2014), 02BB07 *Cited on pages 21, 89.*

References for Chapter 2: Experimental Techniques and Instrumentation

[1] Maria Novella Piancastelli et al. “Hard x-ray spectroscopy and dynamics of isolated atoms and molecules: a review.” In: *Reports on progress in physics. Physical Society (Great*

Britain) 83.1 (2019), p. 016401. ISSN: 0034-4885. DOI: 10.1088/1361-6633/ab5516 *Cited on pages 3, 29, 44.*

[61] D. H. Tomboulian and P. L. Hartman. "Spectral and Angular Distribution of Ultraviolet Radiation from the 300-Mev Cornell Synchrotron". In: *Physical Review* 102.6 (1956), pp. 1423–1447. ISSN: 0031-899X. DOI: 10.1103/physrev.102.1423 *Cited on page 24.*

[62] Philip Willmott. "An Introduction to Synchrotron Radiation". In: (2019). DOI: 10.1002/9781119970958 *Cited on page 25.*

[63] J.-P. Rueff et al. "The GALAXIES beamline at the SOLEIL synchrotron: inelastic X-ray scattering and photoelectron spectroscopy in the hard X-ray range". In: *Journal of Synchrotron Radiation* 22.1 (2015), pp. 175–179. ISSN: 1600-5775. DOI: 10.1107/s160057751402102x *Cited on pages 27, 44.*

[64] *GALAXIES Beamline User Guide, SOLEIL Synchrotron WebPage Cited on pages 27, 28, 33, 34.*

[65] Joseph C. Woicik, ed. *Hard X-ray Photoelectron Spectroscopy (HAXPES)*. 2016. ISBN: 9783319240411 *Cited on page 29.*

[66] R. Guillemin et al. "Postcollision interaction effects in KLL Auger spectra following argon 1s photoionization". In: *Physical Review A* 92.1 (2015), p. 012503. ISSN: 1050-2947. DOI: 10.1103/physreva.92.012503 *Cited on page 29.*

[67] Marc Simon et al. "Atomic Auger Doppler effects upon emission of fast photoelectrons". In: *Nature Communications* 5.1 (2014), p. 4069. DOI: 10.1038/ncomms5069 *Cited on pages 30, 40.*

[68] E. Kukk et al. "Photoelectron recoil in CO in the x-ray region up to 7 keV". In: *Physical Review A* 95.4 (2017), p. 042509. ISSN: 2469-9926. DOI: 10.1103/physreva.95.042509 *Cited on page 30.*

[69] E. Kukk et al. "Energy Transfer into Molecular Vibrations and Rotations by Recoil in Inner-Shell Photoemission". In: *Physical Review Letters* 121.7 (2018), p. 073002. ISSN: 0031-9007. DOI: 10.1103/physrevlett.121.073002 *Cited on page 30.*

[70] Maria Novella Piancastelli et al. "Core-hole-clock spectroscopies in the tender x-ray domain". In: *Journal of Physics B: Atomic, Molecular and Optical Physics* 47.12 (2014), p. 124031 *Cited on page 30.*

[71] Gildas Goldsztejn et al. “Electronic state-lifetime interference in resonant Auger spectra: a tool to disentangle overlapping core-excited states”. In: *Physical Chemistry Chemical Physics* 18.22 (2016), pp. 15133–15142 *Cited on page 30.*

[72] Oksana Travnikova et al. “Hard-X-Ray-Induced Multistep Ultrafast Dissociation”. In: *Physical Review Letters* 116.21 (2016), p. 213001. ISSN: 0031-9007. DOI: 10.1103/physrevlett.116.213001 *Cited on page 30.*

[73] Dimitris Koulentianos. “Double Inner-Shell Vacancies in Molecules”. Doctoral Dissertations in Physics. University of Gothenburg and Sorbonne Université, Apr. 2019 *Cited on page 31.*

[74] LS Cederbaum et al. “On double vacancies in the core”. In: *The Journal of chemical physics* 85.11 (1986), pp. 6513–6523 *Cited on page 31.*

[75] M. Zitnik et al. “Auger hypersatellites in Ne atoms induced by electron impact”. In: *Phys. Rev. A* 49 (2 Feb. 1994), pp. 1480–1483. DOI: 10.1103/PhysRevA.49.1480 *Cited on page 31.*

[76] Dennis L Matthews et al. “High-resolution K-Auger spectra for multiply ionized neon”. In: *Physical Review Letters* 31.22 (1973), p. 1331 *Cited on page 31.*

[77] CW Woods et al. “K-shell Auger-electron hypersatellites of Ne”. In: *Physical Review A* 12.4 (1975), p. 1393 *Cited on page 31.*

[78] S Hagmann et al. “Recoil-charge-state–target-K-Auger-electron coincidences: A technique to study excitation patterns in K-K charge transfer”. In: *Physical Review A* 34.4 (1986), p. 2897 *Cited on page 31.*

[79] R Feifel et al. “Cationic double K-hole pre-edge states of CS 2 and SF 6”. In: *Scientific reports* 7.1 (2017), pp. 1–11 *Cited on page 31.*

[80] G Goldsztejn et al. “Experimental and theoretical study of the double-core-hole hypersatellite Auger spectrum of Ne”. In: *Physical Review A* 96.1 (2017), p. 012513 *Cited on page 31.*

[81] T Marchenko et al. “Ultrafast nuclear dynamics in the doubly-core-ionized water molecule observed via Auger spectroscopy”. In: *Physical Review A* 98.6 (2018), p. 063403 *Cited on page 31.*

[82] Tatiana Marchenko et al. "Single and multiple excitations in double-core-hole states of free water molecules". In: *Journal of Physics B: Atomic, Molecular and Optical Physics* 53.22 (2020), p. 224002 *Cited on page 31.*

[83] *GALAXIES beamline publication's list* *Cited on page 32.*

[84] Zhesheng Chen et al. "Band Gap Renormalization, Carrier Multiplication, and Stark Broadening in Photoexcited Black Phosphorus". In: *Nano Letters* 19.1 (2018), pp. 488–493. ISSN: 1530-6984. DOI: 10.1021/acs.nanolett.8b04344 *Cited on page 32.*

[85] D. Céolin et al. "Ultrafast Charge Transfer Processes Accompanying KLL Auger Decay in Aqueous KCl Solution". In: *Physical Review Letters* 119.26 (2017), p. 263003. ISSN: 0031-9007. DOI: 10.1103/physrevlett.119.263003 *Cited on page 32.*

[86] M Oura et al. "Hard x-ray photoelectron spectroscopy on heavy atoms and heavy-element containing molecules using synchrotron radiation up to 35 keV at SPring-8 undulator beamlines". In: *New Journal of Physics* 21.4 (2019), p. 043015 *Cited on page 32.*

[87] Maria Novella Piancastelli et al. "X-ray versus Auger emission following Xe 1 s photoionization". In: *Physical Review A* 95.6 (2017), p. 061402 *Cited on page 32.*

[88] Nacer Boudjemia et al. "Deep core photoionization of iodine in CH3I and CF3 I molecules: how deep down does the chemical shift reach". In: *Physical Chemistry Chemical Physics* 21.10 (2019), pp. 5448–5454 *Cited on page 32.*

[89] S Ueda et al. "Coherent metallic screening in core-level photoelectron spectra for the strongly correlated oxides La1xBaxMnO3 and V1xWxO2". In: *Physical Review B* 89.3 (2014), p. 035141 *Cited on page 32.*

[90] Ashish Chainani et al. "Quantifying covalency and metallicity in correlated compounds undergoing metal-insulator transitions". In: *Physical Review B* 87.4 (2013), p. 045108 *Cited on page 32.*

[91] T Ohtsuki et al. "Role of Ti 3d Carriers in Mediating the Ferromagnetism of Co TiO2 Anastase Thin Films". In: *Physical Review Letters* 106.4 (2011), p. 047602 *Cited on page 32.*

[92] C Schlueter et al. "The new dedicated HAXPES beamline P22 at PETRAIII". In: *AIP conference proceedings*. Vol. 2054. 1. AIP Publishing LLC. 2019, p. 040010 *Cited on page 33.*

[93] Anastasia Chouprik et al. "Origin of the retention loss in ferroelectric Hf0. 5Zr0. 5O2-based memory devices". In: *Acta Materialia* 204 (2021), p. 116515 *Cited on page 33.*

[94] Stephen Southworth et al. "Inner-shell electron spectroscopy using hard x-rays". In: *51st Annual Meeting of the APS Division of Atomic, Molecular and Optical Physics*. Vol. 65. 4. Advanced Photon Source. 2020 *Cited on page 33.*

[95] *DiffMAX Beamline WebPage* *Cited on page 33.*

[96] *HAXPES Conference 2017* *Cited on page 33.*

[97] *HAXPES Conference 2019* *Cited on page 33.*

[98] D. Céolin et al. "Hard X-ray photoelectron spectroscopy on the GALAXIES beamline at the SOLEIL synchrotron". In: *Journal of Electron Spectroscopy and Related Phenomena* 190 (2013), pp. 188–192. ISSN: 0368-2048. DOI: 10.1016/j.elspec.2013.01.006 *Cited on pages 34, 44.*

[99] "Microchannel Plate Patent" *Cited on pages 35, 37.*

[100] E. Kukk. *Curve Fitting Macro Package SPANCF* *Cited on pages 37, 96.*

[101] L Avaldi et al. "Near-threshold photoionization of the Ar 2p subshell". In: *Journal of Physics B: Atomic, Molecular and Optical Physics* 27.17 (1994), pp. 3953–3966. ISSN: 0953-4075. DOI: 10.1088/0953-4075/27/17/019 *Cited on pages 38, 39, 72.*

[102] *NIST Atomic Spectra Database Energy Levels* *Cited on page 38.*

[103] P Baltzer et al. "Resolution and signaltobackground enhancement in gasphase electron spectroscopy". In: *Review of Scientific Instruments* 64.8 (1993), pp. 2179–2189. ISSN: 0034-6748. DOI: 10.1063/1.1143957 *Cited on page 40.*

[104] M. Jurvansuu, A. Kivimäki, and S. Aksela. "Inherent lifetime widths of Ar 2p-1, Kr 3d-1, Xe 3d-1, and Xe 4d-1 states". In: *Physical Review A* 64.1 (2001), p. 012502. ISSN: 1050-2947. DOI: 10.1103/physreva.64.012502 *Cited on page 41.*

References for Chapter 3: The Relativistic Nature of the Photoionization of the Spin-Orbit Doublets

[1] Maria Novella Piancastelli et al. "Hard x-ray spectroscopy and dynamics of isolated atoms and molecules: a review." In: *Reports on progress in physics. Physical Society (Great Britain)* 83.1 (2019), p. 016401. ISSN: 0034-4885. DOI: 10.1088/1361-6633/ab5516 *Cited on pages 3, 29, 44.*

[6] James A.R Samson. "Photoionization of atoms and molecules". In: *Physics Reports* 28.4 (1976), pp. 303–354. ISSN: 0370-1573. DOI: 10.1016/0370-15737690012-0 *Cited on pages 7, 50.*

[63] J.-P. Rueff et al. "The GALAXIES beamline at the SOLEIL synchrotron: inelastic X-ray scattering and photoelectron spectroscopy in the hard X-ray range". In: *Journal of Synchrotron Radiation* 22.1 (2015), pp. 175–179. ISSN: 1600-5775. DOI: 10.1107/s160057751402102x *Cited on pages 27, 44.*

[98] D. Céolin et al. "Hard X-ray photoelectron spectroscopy on the GALAXIES beamline at the SOLEIL synchrotron". In: *Journal of Electron Spectroscopy and Related Phenomena* 190 (2013), pp. 188–192. ISSN: 0368-2048. DOI: 10.1016/j.elspec.2013.01.006 *Cited on pages 34, 44.*

[105] T. E. H. Walker et al. "Nonstatistical Ratios of Photoionization Cross Sections for States Split by Spin-Orbit Coupling". In: *Phys. Rev. Lett.* 31 (11 Sept. 1973), pp. 678–681. DOI: 10.1103/PhysRevLett.31.678 *Cited on pages 44, 54, 62.*

[106] Akiva Ron, Young Soon Kim, and R. H. Pratt. "Subshell branching ratios of partial photoionization cross sections". In: *Phys. Rev. A* 24 (3 Sept. 1981), pp. 1260–1263. DOI: 10.1103/PhysRevA.24.1260 *Cited on pages 44, 54, 62.*

[107] Young Soon Kim, R. H. Pratt, and Akiva Ron. "Nonstatistical behavior of photoeffect subshell branching ratios at high energies". In: *Phys. Rev. A* 24 (4 Oct. 1981), pp. 1889–1893. DOI: 10.1103/PhysRevA.24.1889 *Cited on pages 44, 54, 62.*

[108] J. Berkowitz. *Photoabsorption, Photoionization and Photoelectron Spectroscopy.* Academic, New York, 1979 *Cited on page 44.*

[109] J. A. R. Samsom. *Handbuch der Physik*. Ed. by W. Mehlhorn. Vol. 31. Berlin and New York: Springer-Verlag, 1982 *Cited on page 44.*

[110] E. W. B. Dias et al. "Breakdown of the Independent Particle Approximation in High-Energy Photoionization". In: *Phys. Rev. Lett.* 78 (24 June 1997), pp. 4553–4556. DOI: 10.1103/PhysRevLett.78.4553 *Cited on pages 45, 47, 54, 56.*

[111] W Drube et al. "Pronounced effects of interchannel coupling in high-energy photoionization". In: *Journal of Physics B: Atomic, Molecular and Optical Physics* 46.24 (2013), p. 245006. ISSN: 0953-4075. DOI: 10.1088/0953-4075/46/24/245006 *Cited on pages 45, 47, 62.*

[112] D. A. Keating et al. "Intershell-correlation-induced time delay in atomic photoionization". In: *Phys. Rev. A* 98 (1 July 2018), p. 013420. DOI: 10.1103/PhysRevA.98.013420 *Cited on page 45.*

[113] Steven T. Manson. "Atomic Photoelectron Spectroscopy, Part I". In: *Advances in Electronics and Electron Physics* 41 (1976), pp. 73–111. ISSN: 0065-2539. DOI: 10.1016/s0065-2539(08)60398-4 *Cited on page 47.*

[114] V Schmidt. "Photoionization of atoms using synchrotron radiation". In: *Reports on Progress in Physics* 55.9 (Sept. 1992), pp. 1483–1659. DOI: 10.1088/0034-4885/55/9/003 *Cited on page 47.*

[115] J. M. Bizau et al. "Photoionization of atomic barium: Ba atoms in the ground state". In: *Physical Review A* 40.6 (1989), pp. 3002–3025. ISSN: 1050-2947. DOI: 10.1103/physreva.40.3002 *Cited on page 47.*

[116] G. Goldsztejn et al. "Double-Core-Hole States in Neon: Lifetime, Post-Collision Interaction, and Spectral Assignment". In: *Physical Review Letters* 117.13 (2016), p. 133001. ISSN: 0031-9007. DOI: 10.1103/physrevlett.117.133001 *Cited on page 47.*

[117] S. Carniato et al. "Photon-energy dependence of single-photon simultaneous core ionization and core excitation in CO2". In: *Physical Review A* 94.1 (2016), p. 013416. ISSN: 2469-9926. DOI: 10.1103/physreva.94.013416 *Cited on page 47.*

[118] U. Fano. "Effects of Configuration Interaction on Intensities and Phase Shifts". In: *Physical Review* 124.6 (1961), p. 1866. DOI: 10.1103/physrev.124.1866 *Cited on pages 48, 49, 58.*

[119] W. R. Johnson and C. D. Lin. "Multichannel relativistic random-phase approximation for the photoionization of atoms". In: *Phys. Rev. A* 20 (3 Sept. 1979), pp. 964–977. DOI: 10.1103/PhysRevA.20.964 *Cited on page 49.*

[120] W R Johnson et al. "Relativistic Random-Phase Approximation". In: *Physica Scripta* 21.3-4 (Jan. 1980), pp. 409–422. DOI: 10.1088/0031-8949/21/3-4/029 *Cited on page 49.*

[121] C. M. Lee and W. R. Johnson. "Scattering and spectroscopy: Relativistic multichannel quantum-defect theory". In: *Phys. Rev. A* 22 (3 Sept. 1980), pp. 979–988. DOI: 10.1103/PhysRevA.22.979 *Cited on page 49.*

[122] Ralph Püttner et al. "Nonstatistical behavior of the photoionization of spin–orbit doublets". In: *Journal of Physics B: Atomic, Molecular and Optical Physics* 54.8 (2021), p. 085001 *Cited on pages 49, 58, 59.*

[123] Marianne Breinig et al. "Atomic inner-shell level energies determined by absorption spectrometry with synchrotron radiation". In: *Physical Review A* 22.2 (1980), pp. 520–528. ISSN: 1050-2947. DOI: 10.1103/physreva.22.520 *Cited on page 50.*

[124] A. Derevianko, W.R. Johnson, and K.T. Cheng. "NON-DIPOLE EFFECTS IN PHOTOELECTRON ANGULAR DISTRIBUTIONS FOR RARE GAS ATOMS". In: *Atomic Data and Nuclear Data Tables* 73.2 (1999), pp. 153–211. ISSN: 0092-640X. DOI: 10.1006/adnd.1999.0818 *Cited on page 52.*

[125] D. L. Hansen et al. "Validity of the independent-particle approximation in x-ray photoemission: The exception, not the rule". In: *Phys. Rev. A* 60 (4 Oct. 1999), R2641–R2644. DOI: 10.1103/PhysRevA.60.R2641 *Cited on pages 54, 56.*

[126] H. S. Chakraborty et al. "Interchannel coupling in the photoionization of the M shell of Kr well above threshold: Experiment and theory". In: *Phys. Rev. A* 63 (4 Mar. 2001), p. 042708. DOI: 10.1103/PhysRevA.63.042708 *Cited on pages 54, 56.*

[127] A. F. Starace. *Handbuch der Physik*. Ed. by W. Mehlhorn. Vol. 31. Springer-Verlag, 1982 *Cited on pages 54, 56.*

[128] H. A. Bethe and E. E. Salpeter. *Quantum Mechanics of One- and Two-Electron Atoms*. Springer Berlin, 1957 *Cited on pages 54, 55, 60.*

[129] K G Dyall. "Shake theory predictions of excited-state populations following 1s ionisation in argon". In: *Journal of Physics B: Atomic and Molecular Physics* 16.17 (1999), p. 3137. ISSN: 0022-3700. DOI: 10.1088/0022-3700/16/17/008 *Cited on page 56.*

[130] Anthony F. Starace. "Behavior of partial cross sections and branching ratios in the neighborhood of a resonance". In: *Phys. Rev. A* 16 (1 July 1977), pp. 231–242. DOI: 10.1103/PhysRevA.16.231 *Cited on page 58.*

[131] Chien-Nan Liu and Anthony F. Starace. "Mirroring behavior of partial photodetachment and photoionization cross sections in the neighborhood of a resonance". In: *Phys. Rev. A* 59 (3 Mar. 1999), R1731–R1733. DOI: 10.1103/PhysRevA.59.R1731 *Cited on page 59.*

References for Chapter 4: Resonant Auger Spectroscopy as a Probe of Conjugation Effects

[101] L Avaldi et al. "Near-threshold photoionization of the Ar 2p subshell". In: *Journal of Physics B: Atomic, Molecular and Optical Physics* 27.17 (1994), pp. 3953–3966. ISSN: 0953-4075. DOI: 10.1088/0953-4075/27/17/019 *Cited on pages 38, 39, 72.*

[132] Jian Luo et al. "A πConjugation Extended Viologen as a TwoElectron Storage Anolyte for Total Organic Aqueous Redox Flow Batteries". In: *Angewandte Chemie International Edition* 57.1 (2018), pp. 231–235. ISSN: 1521-3773. DOI: 10.1002/anie.201710517 *Cited on page 67.*

[133] Piétrick Hudhomme. "An overview of molecular acceptors for organic solar cells". In: *EPJ Photovoltaics* 4 (2013), p. 40401. DOI: 10.1051/epjpv/2013020 *Cited on page 67.*

[134] Marcelo Eising et al. "Doping effect on self-assembled films of polyaniline and carbon nanotube applied as ammonia gas sensor". In: *Sensors and Actuators B: Chemical* 245 (2017), pp. 25–33. ISSN: 0925-4005. DOI: 10.1016/j.snb.2017.01.132 *Cited on page 67.*

[135] Hiroki Uoyama et al. "Highly efficient organic light-emitting diodes from delayed fluorescence". In: *Nature* 492.7428 (2012), pp. 234–238. ISSN: 0028-0836. DOI: 10.1038/nature11687 *Cited on page 67.*

[136] David Bevk et al. "Thiazolo[5,4- d]thiazoles – promising building blocks in the synthesis of semiconductors for plastic electronics". In: *RSC Advances* 3.29 (2013), pp. 11418–11431. ISSN: 2046-2069. DOI: 10.1039/c3ra40851e *Cited on page 67.*

[137] Antonio Facchetti. "π-Conjugated Polymers for Organic Electronics and Photovoltaic Cell Applications". In: *Chemistry of Materials* 23.3 (2011), pp. 733–758. ISSN: 0897-4756. DOI: 10.1021/cm102419z *Cited on page 67.*

[138] M Mauerer et al. "Resonant excitation and decay of core holes in condensed layers of furan and pyrrole". In: *The Journal of Chemical Physics* 99.5 (1993), pp. 3343–3352. ISSN: 0021-9606. DOI: 10.1063/1.465144 *Cited on page 67.*

[139] M. L. M. Rocco, T. Sekiguchi, and Y. Baba. "Photon stimulated ion desorption from condensed thiophene photoexcited around the S 1 s -edge". In: *Journal of Vacuum Science & Technology A* (). DOI: 10.1116/1.3336466 *Cited on page 68.*

[140] M.L.M. Rocco, T. Sekiguchi, and Y. Baba. "Photon stimulated ion desorption from condensed thiolane photoexcited around the S 1s-edge". In: *Journal of Electron Spectroscopy and Related Phenomena* 156 (2007), pp. 115–118. ISSN: 0368-2048. DOI: 10.1016/j.elspec.2006.12.042 *Cited on page 68.*

[141] Igor V Alabugin, Kerry M Gilmore, and Paul W Peterson. "Hyperconjugation". In: *Wiley interdisciplinary reviews: computational molecular science* 1.1 (2011), pp. 109–141 *Cited on page 69.*

[142] Igor V Alabugin, Gabriel dos Passos Gomes, and Miguel A Abdo. "Hyperconjugation". In: *Wiley Interdisciplinary Reviews: Computational Molecular Science* 9.2 (2019), e1389 *Cited on page 69.*

[143] Alexandre B. Rocha. "Potential curves for inner-shell states of CO calculated at multiconfigurational self-consistent field level". In: *The Journal of Chemical Physics* 134.2 (2011), p. 024107. DOI: 10.1063/1.3528725. eprint: https://doi.org/10.1063/1.3528725 *Cited on page 69.*

[144] Carlos E. V. de Moura, Ricardo R. Oliveira, and Alexandre B. Rocha. "Transition energy and potential energy curves for ionized inner-shell states of CO, O2 and N2 calculated by several inner-shell multiconfigurational approaches". In: *Journal of Molecular Modeling* 19.5 (2013), pp. 2027–2033. ISSN: 1610-2940. DOI: 10.1007/s00894-012-1622-x *Cited on page 69.*

[145] Michael W Schmidt and Mark S Gordon. "The construction and interpretation of MCSCF wavefunctions". In: *Annual Review of Physical Chemistry* 49.1 (1998), pp. 233–266. ISSN: 0066-426X. DOI: 10.1146/annurev.physchem.49.1.233 *Cited on page 69.*

[146] J P Foster and F Weinhold. "Natural hybrid orbitals". In: *Journal of the American Chemical Society* 102.24 (1980), pp. 7211–7218. ISSN: 0002-7863. DOI: 10.1021/ja00544a007 *Cited on page 70.*

[147] Alan E Reed, Robert B Weinstock, and Frank Weinhold. "Natural population analysis". In: *The Journal of Chemical Physics* 83.2 (1985), pp. 735–746. ISSN: 0021-9606. DOI: 10.1063/1.449486 *Cited on page 70.*

[148] Fatemeh Abyar and Hossein Farrokhpour. "Symmetry adapted cluster–configuration interaction calculation of the photoelectron spectra of famous biological active steroids". In: *Journal of Molecular Structure* 1076 (2014), pp. 69–79. ISSN: 0022-2860. DOI: 10.1016/j.molstruc.2014.07.040 *Cited on page 70.*

[149] Dumitru-Claudiu Sergentu, Thomas J Duignan, and Jochen Autschbach. "Ab Initio Study of Covalency in the Ground versus Core-Excited States and X-ray Absorption Spectra of Actinide Complexes". In: *The Journal of Physical Chemistry Letters* 9.18 (2018), pp. 5583–5591. ISSN: 1948-7185. DOI: 10.1021/acs.jpclett.8b02412 *Cited on page 70.*

[150] Alan E Reed, Larry A Curtiss, and Frank Weinhold. "Intermolecular interactions from a natural bond orbital, donor-acceptor viewpoint". In: *Chemical Reviews* 88.6 (1988), pp. 899–926. ISSN: 0009-2665. DOI: 10.1021/cr00088a005 *Cited on page 70.*

[151] Frank Weinhold. "Natural bond orbital analysis: A critical overview of relationships to alternative bonding perspectives". In: *Journal of Computational Chemistry* 33.30 (2012), pp. 2363–2379. ISSN: 0192-8651. DOI: 10.1002/jcc.23060 *Cited on page 70.*

[152] Eric D. Glendening, Clark R. Landis, and Frank Weinhold. "Natural bond orbital methods". In: *Wiley Interdisciplinary Reviews: Computational Molecular Science* 2.1 (2012), pp. 1–42. ISSN: 1759-0876. DOI: 10.1002/wcms.51 *Cited on page 70.*

[153] Frank Weinhold and Clark R. Landis. *Valency and Bonding: A Natural Bond Orbital Donor-Acceptor Perspective*. Cambridge University Press, 2005. DOI: 10.1017/CBO9780511614569 *Cited on page 70.*

[154] Tadeusz Marek Krygowski and Beata Tamara Stepien. "Sigma- and Pi-Electron Delocalization: Focus on Substituent Effects". In: *Chemical Reviews* 105.10 (2005), pp. 3482–3512. ISSN: 0009-2665. DOI: 10.1021/cr030081s *Cited on page 70.*

[155] Igor V. Alabugin, Gabriel dos Passos Gomes, and Miguel A. Abdo. "Hyperconjugation". In: *Wiley Interdisciplinary Reviews: Computational Molecular Science* 9.2 (2019). ISSN: 1759-0876. DOI: 10.1002/wcms.1389 *Cited on page 70.*

[156] Marvin Douglas and Norman M Kroll. "Quantum electrodynamical corrections to the fine structure of helium". In: *Annals of Physics* 82.1 (1974), pp. 89–155. ISSN: 0003-4916. DOI: 10.1016/0003-4916(74)90333-9 *Cited on page 71.*

[157] Bernd A. Hess. "Applicability of the no-pair equation with free-particle projection operators to atomic and molecular structure calculations". In: *Physical Review A* 32.2 (1985), pp. 756–763. ISSN: 1050-2947. DOI: 10.1103/physreva.32.756 *Cited on page 71.*

[158] Bernd A. Hess. "Relativistic electronic-structure calculations employing a two-component no-pair formalism with external-field projection operators". In: *Physical Review A* 33.6 (1986), pp. 3742–3748. ISSN: 1050-2947. DOI: 10.1103/physreva.33.3742 *Cited on page 71.*

[159] Thom H. Dunning. "Gaussian basis sets for use in correlated molecular calculations. I. The atoms boron through neon and hydrogen". In: *J. Chem. Phys.* 90 (1989). DOI: 10.1063/1.456153 *Cited on page 71.*

[160] Rick A. Kendall, Thom H. Dunning, and Robert J. Harrison. "Electron affinities of the first-row atoms revisited. Systematic basis sets and wave functions". In: *J. Chem. Phys.* 96 (1992). DOI: 10.1063/1.462569 *Cited on page 71.*

[161] David E. Woon and Thom H. Dunning. "Gaussian basis sets for use in correlated molecular calculations. III. The atoms aluminum through argon". In: *J. Chem. Phys.* 98 (1993). DOI: 10.1063/1.464303 *Cited on page 71.*

[162] David E. Woon and Thom H. Dunning. "Gaussian basis sets for use in correlated molecular calculations. V. Core-valence basis sets for boron through neon". In: *J. Chem. Phys.* 103 (1995). DOI: 10.1063/1.470645 *Cited on page 71.*

[163] W. A de Jong, R. J. Harrison, and D. A. Dixon. "Parallel Douglas-Kroll energy and gradients in NWChem: Estimating scalar relativistic effects using Douglas-Kroll contracted basis sets". In: *J. Chem. Phys.* 114 (2001). DOI: 10.1063/1.1329891 *Cited on page 71.*

[164] Kirk A. Peterson and Thom H. Dunning. "Accurate correlation consistent basis sets for molecular core-valence correlation effects: The second row atoms Al-Ar, and the first row

atoms B-Ne revisited". In: *J. Chem. Phys.* 117 (2002). DOI: 10.1063/1.1520138 *Cited on page 71.*

[165] L. R. Varas et al. "Breaking the disulfide chemical bond using high energy photons: the dimethyl disulfide and methyl propyl disulfide molecules". In: *RSC Advances* 7.58 (2017), pp. 36525–36532. ISSN: 2046-2069. DOI: 10.1039/c7ra05001a *Cited on page 71.*

[166] H.-J. Werner et al. "Molpro: a generalpurpose quantum chemistry program package". In: *WIREs Comput Mol Sci* 2 (2012), pp. 242–253 *Cited on page 71.*

[167] H.-J. Werner et al. *MOLPRO, version 2012.1, a package of ab initio programs.* http://www.molpro.net Cardiff, UK, 2012 *Cited on page 71.*

[168] A P Hitchcock, J A Horsley, and J Stöhr. "Inner shell excitation of thiophene and thiolane: Gas, solid, and monolayer states". In: *The Journal of Chemical Physics* 85.9 (1986), pp. 4835–4848. ISSN: 0021-9606. DOI: 10.1063/1.451718 *Cited on pages 72, 73, 75.*

[169] A Daniel Boese and Roland Boese. "Tetrahydrothiophene and Tetrahydrofuran, Computational and X-ray Studies in the Crystalline Phase". In: *Crystal Growth & Design* 15.3 (2015), pp. 1073–1081. ISSN: 1528-7483. DOI: 10.1021/cg501228w *Cited on page 73.*

[170] A P Hitchcock et al. "Carbon K shell excitation of gaseous and condensed cyclic hydrocarbons: C3H6, C4H8, C5H8, C5H10, C6H10, C6H12 , and C8H8shell excitation of gaseous and condensed cyclic hydrocarbons: C3H6, C4H8, C5H8, C5H10, C6H10, C6H12 , and C8H8". In: *The Journal of Chemical Physics* 85.9 (1986), pp. 4849–4862. ISSN: 0021-9606. DOI: 10.1063/1.451719 *Cited on page 75.*

[171] A P Hitchcock and I Ishii. "Carbon K-shell excitation spectra of linear and branched alkanes". In: *Journal of Electron Spectroscopy and Related Phenomena* 42.1 (1987), pp. 11–26. ISSN: 0368-2048. DOI: 10.1016/0368-2048(87)85002-8 *Cited on page 75.*

[172] Shirin Behyan, Yongfeng Hu, and Stephen G Urquhart. "Sulfur 1 s near edge x-ray absorption fine structure spectroscopy of thiophenic and aromatic thioether compounds". In: *The Journal of Chemical Physics* 138.21 (2013), p. 214302. ISSN: 0021-9606. DOI: 10.1063/1.4807604 *Cited on page 75.*

[173] Graham N. George et al. "Long-Range Chemical Sensitivity in the Sulfur KEdge Xray Absorption Spectra of Substituted Thiophenes". In: *The Journal of Physical Chemistry A* 118.36 (2014), pp. 7796–7802. ISSN: 1089-5639. DOI: 10.1021/jp505766f *Cited on page 75.*

[174] Valérie Brenner, Eric Gloaguen, and Michel Mons. "Rationalizing the diversity of amideamide H-bonding in peptides using the natural bond orbital method". In: *Physical Chemistry Chemical Physics* 21.44 (2019), pp. 24601–24619. ISSN: 1463-9076. DOI: 10.1039/c9cp03825f *Cited on page 84.*

References for Chapter 5: Electron Dynamics in Sulfur-Based Polymers Using Core-Hole Clock Spectroscopy

[41] MF Kling et al. "Control of electron localization in molecular dissociation". In: *Science* 312.5771 (2006), pp. 246–248 *Cited on pages 19, 88.*

[42] Giuseppe Sansone et al. "Electron localization following attosecond molecular photoionization". In: *Nature* 465.7299 (2010), pp. 763–766 *Cited on pages 19, 88.*

[47] PA Brühwiler, O Karis, and N Mårtensson. "Charge-transfer dynamics studied using resonant core spectroscopies". In: *Reviews of Modern Physics* 74.3 (2002), p. 703 *Cited on pages 19, 92, 93.*

[59] C Arantes et al. "Femtosecond electron delocalization in poly (thiophene) probed by resonant auger spectroscopy". In: *The Journal of Physical Chemistry C* 117.16 (2013), pp. 8208–8213 *Cited on pages 21, 89, 96, 102, 103.*

[60] Hiromi Ikeura-Sekiguchi and Tetsuhiro Sekiguchi. "Molecular ordering effect of regioregular poly (3-hexylthiophene) using sulfur K-edge X-ray absorption spectroscopy". In: *Japanese Journal of Applied Physics* 53.2S (2014), 02BB07 *Cited on pages 21, 89.*

[100] E. Kukk. *Curve Fitting Macro Package SPANCF* *Cited on pages 37, 96.*

[175] Hideki Shirakawa et al. "Synthesis of electrically conducting organic polymers: halogen derivatives of polyacetylene,(CH) x". In: *Journal of the Chemical Society, Chemical Communications* 16 (1977), pp. 578–580 *Cited on page 88.*

[176] Jiamo Guo et al. "Charge generation and recombination dynamics in poly (3-hexylthiophene)/fullerene blend films with different regioregularities and morphologies". In: *Journal of the American Chemical Society* 132.17 (2010), pp. 6154–6164 *Cited on page 88.*

[177] Christos D Dimitrakopoulos and Patrick RL Malenfant. “Organic thin film transistors for large area electronics”. In: *Advanced materials* 14.2 (2002), pp. 99–117 *Cited on page 88.*

[178] Jesus Nieto-Pescador, Baxter Abraham, and Lars Gundlach. “Photoinduced Ultrafast Heterogeneous Electron Transfer at Molecule–Semiconductor Interfaces”. In: *The journal of physical chemistry letters* 5.20 (2014), pp. 3498–3507 *Cited on page 88.*

[179] Veaceslav Coropceanu et al. “Charge transport in organic semiconductors”. In: *Chemical reviews* 107.4 (2007), pp. 926–952 *Cited on page 88.*

[180] Vincent V Duong, David Prendergast, and Alexander L Ayzner. “Ultrafast core-excited electron dynamics in model crystalline organic semiconductors”. In: *Physical Chemistry Chemical Physics* 22.3 (2020), pp. 1400–1408 *Cited on page 89.*

[181] Hiromi Ikeura-Sekiguchi and Tetsuhiro Sekiguchi. “Unoccupied electronic states in polythiophene as probed by XAS and RAS”. In: *Surface and Interface Analysis: An International Journal devoted to the development and application of techniques for the analysis of surfaces, interfaces and thin films* 40.3-4 (2008), pp. 673–675 *Cited on pages 89, 102, 109.*

[182] Y Garcia-Basabe et al. “The interplay of electronic structure, molecular orientation and charge transport in organic semiconductors: Poly (thiophene) and poly (bithiophene)”. In: *Organic Electronics* 14.11 (2013), pp. 2980–2986 *Cited on page 89.*

[183] Alan J Heeger. “Semiconducting polymers: the third generation”. In: *Chemical Society Reviews* 39.7 (2010), pp. 2354–2371 *Cited on page 91.*

[184] Dietrich Menzel. “Ultrafast charge transfer at surfaces accessed by core electron spectroscopies”. In: *Chemical Society Reviews* 37.10 (2008), pp. 2212–2223 *Cited on page 93.*

[185] Sigma-Aldrich. *Fiche de données de sécurité - P3HT* *Cited on page 93.*

[186] Albert C Thompson, Douglas Vaughan, et al. *X-ray data booklet*. Vol. 8. 4. Lawrence Berkeley National Laboratory, University of California Berkeley, CA, 2001 *Cited on page 96.*

[187] H Sirringhaus et al. “AJ; Meijer, EW; Herwig, P.; de Leeuw, DM”. In: *Nature* 401.6754 (1999), pp. 685–688 *Cited on pages 98, 99.*

[188] Xin-Yan Zhao et al. "Nanostructured semiconducting polymer films with enhanced crystallinity and reorientation of crystalline domains by electrospray deposition". In: *Macromolecular Materials and Engineering* 302.9 (2017), p. 1700090 *Cited on page 98.*

[189] Dean M DeLongchamp et al. "Variations in semiconducting polymer microstructure and hole mobility with spin-coating speed". In: *Chemistry of materials* 17.23 (2005), pp. 5610–5612 *Cited on page 99.*

[190] Yeong Don Park. "The Molecular Structures of Poly (3-hexylthiophene) Films Determine the Contact Properties at the Electrode/Semiconductor Interface". In: *Bulletin of the Korean Chemical Society* 35.8 (2014), pp. 2277–2280 *Cited on page 100.*

[191] JL Campbell and Tibor Papp. "Widths of the atomic K–N7 levels". In: *Atomic Data and Nuclear Data Tables* 77.1 (2001), pp. 1–56 *Cited on page 103.*

References for Chapter 6: Conclusions and Outlooks

[181] Hiromi Ikeura-Sekiguchi and Tetsuhiro Sekiguchi. "Unoccupied electronic states in polythiophene as probed by XAS and RAS". In: *Surface and Interface Analysis: An International Journal devoted to the development and application of techniques for the analysis of surfaces, interfaces and thin films* 40.3-4 (2008), pp. 673–675 *Cited on pages 89, 102, 109.*

[192] S Kosugi et al. "Conjugate photoelectron recapture peaks in the high resolution Auger electron spectra following near-threshold Ar 2p photoionization". In: *Journal of Physics B: Atomic, Molecular and Optical Physics* 53.12 (2020), p. 125001. ISSN: 0953-4075. DOI: 10.1088/1361-6455/ab7fc1 *Cited on page 109.*

[193] S. Kosugi et al. "Strong configuration interaction in the 3p photoelectron spectrum of Kr". In: *Physical Review A* 101.4 (2020), p. 042505. ISSN: 2469-9926. DOI: 10.1103/physreva.101.042505 *Cited on page 109.*

Acknowledgements

Undertaking this Ph.D. has been an absolutely life-changing experience for me, even more in these unique (and challenging) times. This important step of my life would not have been possible without the support and guidance that I received from many people.

First, I am grateful to have been supervised by Dr. Tatiana Marchenko. I admire how brilliant she is doing science. I appreciate all of the knowledge she shared with me and all the discussions we had, which helped me develop myself as a scientist. Also, I gratefully acknowledge the funding received towards my Ph.D. from the Agence Nationale de la Recherche (ANR) Ph.D. fellowship.

I also would like to thank Dr. Marc Simon for accepting me into his research group. I am thankful to have been part of this top-level research team. So, I would like to thank all the group members, Prof. Dr. Maria Novella Piancastelli, Prof. Dr. Loïc Journel, Dr. Oksana Travnikova, Dr. Renaud Guillemin, and Dr. Iyas Ismail, for always being pleasant and helpful.

I would like to thank the jury members Prof. Dr. Emmanuel Maisonhaute, Prof. Dr. Arnaldo Naves de Brito, Dr. Lorenzo Avaldi, Dr. Valérie Brenner, and Dr. Evangelos Papalazarou for accepting participate in this crucial step of my career.

My thanks to the collaborators directly involved in the work presented in this thesis: Dr. Steven Manson, Dr. Ralph Püttner, Dr. Carlos Eduardo de Moura, Dr. Laure Fillaud, and Prof. Dr. Maria Luiza Rocco. I wish to extend my special thanks to two of our research group collaborators: Dr. Ralph Püttner and Dr. Yoshiro Azuma, for always being kind and patient with the students and always being open to discussions.

I am confident that this time being part of LCPMR provided me the experience I needed to advance my career to the next level, so many thanks to all the LCPMR permanent members. I am thankful to have been part of the team. In particular, I would like to thank the LCMPR's

director, Dr. Richard Taïeb, for always being kind and concerned for all students' welfare in our laboratory, especially in these weird times with all the difficulties that the sanitary crisis brought. Many thanks also to the two LCPMR's secretaries, David Massot and Sophie Gargan, for always saving all of us dealing with the french paperwork.

I also have to say thank you to my colleagues for sharing their Ph.D. journey with me, making it softer and funny: Dimitris Koulentianos, Nacer Boudjemia, Moustafa Zmerli, Hang Liu, Nicolas Velasquez, Roba Moussaoui, and all the Ph.D. students who are or were part of our lab. In special, many thanks to Farzad Hosseini for sharing the office with me and for the long conversations about life in France, the future, good music, and obviously, science. After all, as the one would say: *"Don't be shy... Let's talk about science!"*

I would like to thank two people that I consider as my "parents in science", Prof. Dr. Maria Luiza Rocco and Prof. Dr. Alexandre Braga da Rocha. They are my primary inspiration as scientists, and I think that today, more than mentors, we can consider ourselves as friends.

Many, many thanks also to my longtime friends Maria Clarissa Silva and Celina Oliveira. We remain together after all this time, even if at a distance (*the TWIX will never die!*). I also include Rodolfo Bantim in my thanks (I hope we can soon play some board game while we criticize Flamengo!). You guys could not imagine how you helped me in this journey, even if just making small talk.

I am thankful for having my parents João and Lilian because they are why I walked all this way here. They were the people responsible for giving me all the support to develop my critical sense and curiosity, two essential ingredients to form a scientist. Also, I am grateful to have my younger sister Patricia Caroline on my side, supporting me in all situations, in the good and bad moments, even though now we are physically separated by a Continent away. I also would like to thank my parents-in-law Isabel Maria and Augusto Carlos and my sister-in-law Gabriela for always being kind and supportive.

Finally, I always think how lucky I am to have found my husband Carlos Eduardo in this vast world. Thank you for being who you are and for being my collaborator, partner, and best friend. Thank you for our little family and our four-legged son, Ringo Starr. Thank you for being patient when I am in a bad mood and bringing me back to reality every time I feel too pessimistic. We are better and stronger together, and we are confident that we will win in this

life together forever and always.